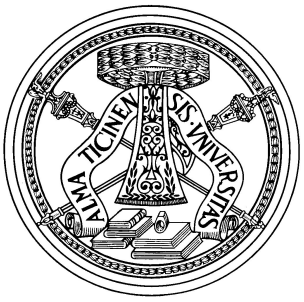

UNIVERSITÀ DEGLI STUDI DI PAVIA

Facoltà di Ingegneria

Dipartimento di Ingegneria Civile e Architettura

Corso di Laurea Magistrale in Ingegneria Civile

Indirizzo Strutturistico

Fem Analysis of the Fluid Structure Interaction between shock-waves and deformable structures

Analisi Fem dell'Interazione Fluido Struttura tra onde d'urto e strutture deformabili

Relatore: Chiar.mo Professore

Ferdinando Auricchio

Correlatore: Dott.Ing.

Andrea Montanino

Candidato:

Enrico Scarin

N.Matr. 395445

Anno Accademico 2011/2012

Alla mia famiglia

Ringraziamenti

Giunto al termine di questo infinito lavoro vorrei rivolgere qualche parola alle persone che in un modo o nell'altro sono state importanti, non solo allo svolgimento di questa tesi, ma in tutta la mia vita universitaria. Per questo in primo luogo devo ringraziare i miei genitori, Antonella e Arrigo, per avermi dato tranquillità e sostentamento, per essere stati sempre entusiasti in tutto ciò che ho fatto, e per aver creduto sempre in me , cosa che valutando il soggetto in questione, è tutt'altro che facile! Un grazie importante anche a Sarah e Sabrina, perchè volenti o nolenti siete la mia famiglia!

Ringrazio coloro che mi hanno aiutato a sviluppare questo lavoro, il professore Auricchio per avermi spronato nei momenti di difficoltà, e Andrea per esserci stato ogni giorno, per avermi obbligato a lavorare duro e per tutto quell'entusiasmo che sei riuscito a trasmettermi.

Un grazie infinito poi va a tutti i miei compagni di università, che da semplici compagni di studio, sono diventati veri e propri amici. Un grazie a Dino perchè ora non ci dimenticheremo mai della rigidezza assiale, a Simo per le studiate folli che mi obbligavi a fare, a Max futuro mastro birraio, oltre che futuro ing!. Grazie a Cico per la suprema sapienza, grazie a Leo a Bobo a Mago e a Dade, l'unico che mi ha sopportato per tutti e 5 gli anni! Grazie anche a Gampe, perchè per una bevuta ci sei sempre!

Come poter non ringraziare i miei amici di sempre, mi spiace se trascurerò

qualcuno! Un grazie a Jack, per non esserci nemmeno alla mia seconda laurea, ma per esserci sempre quando serve, un grazie Solla e a Seba per le mille sciate, e un grazie lo devo a te , Simone, perchè io stesso stento a credere che non siamo fratelli.

Un grazie lo devo anche a me, per essere riuscito a concludere questo difficile percorso, mantenendo la serenità e l'entusiasmo di affrontare un' esperienza unica come quella universitaria.

E infine grazie a te Jennifer, per aver conquistato un posto importante nel mio cuore, per rendere speciale ogni giornata, per essere semplicemente, la mia Chica.

Abstract

The effects of an explosion have gained an increasing importance in the phase of load definition in the design of strategical structures, like military structures, major civil constructions and infrastructures. For this reason is very important to provide a physics systems to mitigate the effects of shock-waves on structures. In this thesis work we deal with the study of the fluid-structure interaction between shock-waves and deformable structures. The numerical simulations have been run by the commercial Finite Element code $LS-Dyna$, an hydro-code particularly suited for simulation of fast dynamics, fluid-structure interaction and impacts. After some simple examples basically acts to validate the methods used for the simulations, we focused on the model and the simulation of the experimental test carried out in mine at the University of Naples Federico II, consisting in a blast of a quantity of $5Kg$ of commercial explosive in proximity of a porous barrier composed by $GFRP$ pipes stuck in a precast concrete basement. The obtained numerical results are in substantial agreement with the experimental data and confirm the effectiveness of such protection systems.

Sommario

Gli effetti di una esplosione hanno assunto una crescente importanza nella fase di definizione dei carichi da tenere in considerazione nella progettazione di strutture strategiche, quali strutture militari, grandi opere civili e infrastrutture. E' quindi anche molto importante prevedere dei sistemi fisici per attenuare l'effetto delle onde d'urto sugli edifici. In questo lavoro di tesi si affronta lo studio dell'interazione fluido struttura tra onde d'urto generate da esplosioni e strutture deformabili. Le simulazioni numeriche sono state condotte utilizzando il codice commerciale $LS-Dyna$, un idrocodice esplicito adatto per le simulazioni di dinamica veloce, interazione fluido struttura e impatti. Dopo alcuni esempi elementari tendenzialmente tesi a validare il metodo usato per le simulazioni, ci si è concentrati sulla modellazione e simulazione del test sperimentale condotto in cava dall'Università degli Studi di Napoli Federico II, consistente lo scoppio di un quantitativo di $5Kg$ di esplosivo commerciale in prossimità di una barriera porosa composta da tubi di $GFRP$ incastrati in una base di calcestruzzo prefabbricato. I risultati numerici ottenuti sono in sostnziale accordo con i dati sperimentali e confermano l'efficacia di tali sistemi di protezione.

Contents

Chapter 1

Introduction

Recent terrorist attacks have contributed in changing the design approach to critical infrastructures; in fact, malicious disruptions, blasts, or impacts have unfortunately become part of the possible load scenarios that could act on buildings during their life spans. Consequently, specific protection interventions have been introduced to minimize disruptive effects, guarantee the safety of the occupants,and ,to the extent possible, maintain the functionality of buildings.

1.1 The SAS project

This work of thesis is inserted within of the *SAS* (Security of Airport Structures), a project developed with the aim of designing buildings aimed to assure protection to strategic structures against terrorist attacks, and then, to preserve the safety of things and people at risk. This project is addressed to the study, in a systematic manner, of the complex theme of the security of structures aimed to the control and the assistance to the air navigation.

The main goal of the research project is to develop and deploy a structural

fencing system able to protect VHF Omnidirectional Range (VOR) stations against malicious actions consisting of intrusion and blast loads of relatively small explosive charges placed in the neighborhood or in contact with the barrier. The VOR is a radio-navigation system for aircraft, that transmits VHF waves; from here the necessity to use radio-transparenct materials.

Figure 1.1: VOR station in Sorrento (NA)

The aim of this project is to give the structure an adequate level of protection, trough the usage of materials permeable to radio frequencies in order to not interpose with the aeronautical communications of radio-navigation and air traffic control. Therefore the critical feature of any protective barrier for this type of buildings is radio transparency, which is necessary to avoid any disturbance to radio communications of specific frequencies.

Hence, in order to achieve such goals, a discontinuous (porous) barrier composed by $GFRP$ and precast concrete elements reinforced with $GFRP$

bars was designed to take advantage of electromagnetic and mechanical properties of composites. The proposed barrier provides protection through two contributions: first, its geometrical and mechanical characteristics ensure protection against intrusions and blast loads; moreover, its shape provides an attenuation of the blast shock-wave, adding some level of additional protection to the facilities located beyond it.

1.2 How to deal with an explosive problem

This works, in particular, deals with the fluid-dynamics simulation of the experimental test, with the use of a modern hydro-code. The importance of a numerical simulation stares in the fact that it is possible to minimize the number of requested experimental tests, that are very expensive, and also helps us to understand the results of the tests itself. Once a simulation is validate, by comparing the numerical results with the results of the tests, it can be used like a design instrument to improve the systems of more complex structures. So if the scale and the complexity of the problem is very high, the better way is to reduce to the minimum the experimental tests, and improve the numerical simulation.

The treatment of the explosion problems in air and the interaction of the products of the explosions with the structures, result very onerous, both for the cost of the experimental tests, and for the implementation of the numerical models. Last problem, carried out at the University of Naples (Asprone et al., 2009) is due to the fact that the effects in particular of explosions are loads of high intensity and very low span.

The analysis methodologies most used for the description of the physics phenomenon, provide a complex discretization of the continuum. So we can

differentiate between two typologies of methods. At first, the *Lagrangian* methods, used mostly for the mesh of solid elements, and for the solution of structural mechanical problems, where the deformation are infinitesimal. In our case a Lagrangian problem is used to simulate a blast effect on a Lagrangian solid, thanks to a *Blast Load* function (Pehrson and Bannister, 1997) available in the hydro-code. Usually, when it is necessary to deal with problems where there are large deformation, (i.e fluid-dynamics) the *Eulerian* formulation is more suited. Finally the *ALE* (Arbitrary Lagrangian Eulerian) methods, allow us to treat any size of deformations, because they are methods that combine the two previous formulations.

Our case study, is a Fluid-Structure Interaction problem (FSI). Such problems can be treated in different ways, that are mentioned in chapter 2.

1.3 Faced Problems

We treat the explosion problem step by step, in the way to understand the behaviour of the physics phenomenon. In the following chapters we first describe the physics characterization of an explosion, then the most used numerical methods , with particular care to the methods used in this work, and the codes used for the calculation. So we want to know how the Lagrangian structures react to impulsive loads (i.e a pressure wave due to a blast), and at the same time, the behaviour of the shock-wave in impacting with a structure, like the barrier token in exam. First of all we have set up a pure lagrangian model where a cantilever beam interacts with a pressure load due to an explosion. The pressure enforced on the beam is applied with the CONWEP function (Pehrson and Bannister, 1997) integrated in the hydro-code. In this first approach we want to see how the loads due to an explosion are enforced,

and how the stress propagates in the solid, comparing it with some analytical results. This approach presents some limitations, that will be explained in the following, so we consider the ALE formulation to have a more complete description of an explosion, and observe the subsequent propagation of the pressure wave, and the interaction with a solid structure. We checked various theoretical parameters to verify the rightness of the simulation. Then we introduce a couple of models with the fluid-structure interaction method. The final numerical model presents the interaction between the shock-wave due to the explosion of the charge of the experimental test with the porous barrier. At the end of the work the main results of the simulation have been reported, and compared with the semi-empirical formulations existing in the literature and with the results of the experimental tests.

Chapter 2

Explosions and Shock-Waves

2.1 The Explosion

The explosion is a phenomenon of chemical transformation or chemical-physical transformation that, starting from a solid element, liquid or gaseous, and generates the formation of a gas at high pressures (Bergano, 1973). Such a transformation takes place in a very rapid time and, in general, is accompanied by the development of energy (for good thermal part) and gas. The transformation of the internal energy of the explosive, from chemical energy into thermal energy, determines the characteristic speed of the explosion, which can be disruptive or propellant.

Any system that for administration of very small quantities of thermal or mechanical energy and capable of chemically transformation in a very short time, with the development of energy, gas and vapours, constitutes an explosive system. An explosive, is a substance, or the mechanical joining of two or more substances (mixture) that, as a result of specific external stimuli, become chemically unstable undergoing a decomposition reaction for combustion. An explosive system is said homogeneous if constituted by

a single chemical species and heterogeneous when and instead consists of several chemicals. The gases produced by the reaction, because of the high temperatures reached in the explosion, tends to occupy volumes enormously higher than those corresponding to the starting substances. The explosion generates, in the external medium, a pressure wave, with short and long distance effects. The main long distance effect is the creation of a shock-wave which propagates by creating an overpressure followed by a longer phase of depression. The pressure wave, when it encounters an object, produces lesions which can then be aggravated by the wave of depression, such as a wall can be damaged by the wave and then dropped an explosive wave of suction or retrograde. From a short distance instead, the explosion acts directly with shock-waves buttons that cross the objects and are reflected by its free surfaces so that stress created in it causes the collapse. So the explosives are substances with high-energy content, which, through the explosion, are transformed into substances that are stable at much lower energy level. Solid explosives are solid mixtures or combinations likely to take on the regime of *detonation*; we reserve the name of "powder explosives" that take the regime of *deflagration* (Seguiti, 1969).

2.1.1 Detonation and Deflagration

The combustion of explosive materials produces energy that generates a shock-wave. The propagation at high velocity of the enormous quantity of gas generated by the chemical reaction, is accompanied by a flame and a noise due to the displacement of the shock-wave. The explosive materials, in order to its chemical compositions and the physics disposition of the molecules, enforce to the gas a specific propagation velocity. So the analysis of the shock-wave is an important indication about the velocity of the

gas projected by the explosion (Seguiti, 1969). Moreover an other important characteristic data is the confinement of the explosive, because, depending on this, the explosive substance can burn or explode. Also the chemical reaction develops with different velocities as a result of various factors: temperature, concentration of reactive, presence of catalyst. We can talk about *explosive velocities* when the explosion develops in a very short time, lower than those necessary for the transmission of the heat of the reaction trough the medium for conductivity and radiation and so its stores in the product gas, as a form of kinetic energy.

The explosive velocities are always high but can change a lot. The explosions that occurs at low velocities are called **Deflagrations** (also called first grade explosions), and the explosive that happens at high velocities are called **Detonations** (or second grade explosions). The deflagration velocities are in general of the order of hundred meters per second, and the detonations velocities are between 1000 and 9000 m/s. However the limits of the deflagration velocities cannot be defined with precision, because they depend on various factors. In fact besides the graining of the powders have influence the magnitude of the primer, the density of the charge, the diameter of the charge have great influence. As a function of various factors, first of all the violence of the initial shock, the deflagration can transform in detonation and an explosive normally deflagrating, like the black powder, can detonate when it is strongly triggered. Conversely the dynamite, that is a detonating explosive, can deflagrate when weakly triggered. The difference between deflagration and detonation lies not only in the speed with which the chemical phenomenon proceeds; the two methods of propagation are in fact substantially different.

The deflagration is an explosive phenomenon that, due to thermal con-

ductivity, propagates from the outer surface of the mass to the inside. The duration of the reaction is lower for thin powders graining (which have greater surface area per unit weight), so for different graining corresponds different deflagration velocities. These velocities that are very lower in confront of the detonation velocities, have lower disruptive effects.

Figure 2.1: Deflagration

The detonation is a so violent phenomenon that cannot be explained only by the mechanism of combustion and in fact it propagates with the wave explosive mechanism. In the above wave is associated with a physical phenomenon (pressure wave or shock wave) and a chemical phenomenon (combustion reaction, also known as the combustion wave). The two phenomena are mutually supportive so that explosive coexists on the wave face, the shock wave and the chemical reaction. The detonation is not necessarily a phenomenon of combustion. In fact, some elements in the detonation do not undergo oxidation phenomena, but rather a decomposition reaction. In the explosion of gas mixtures, is defined a period beginning or start of the detonation, the time interval between the instant at which the mixture ig-

nites and the instant at which the wave explosive starts . During this period, the speed of the flame grows very rapidly until it reaches the speed of the wave explosive. A similar starting period occurs in the detonation of solid explosives.

Figure 2.2: Detonation

It is dangerous when an deflagrant explosive detonates, but it is also dangerous when a detonating explosive deflagrates, because in this a lot of anomalies case can occur, for example when all the charge, or a part of it, does not reach the detonation regime, but develops in a deflagration regime, burning with lower velocities. A deflagrant explosive is appreciable when we want to obtain a pushing effect and not disruptive. On the other hand a detonating explosive is to prefer when we want to enforce violent and disruptive forces.

2.2 Shock-Waves

Baker et al. (1983) define the explosion as a process by which a pressure wave of finite amplitude is generated in air by a rapid release of energy. An explosion initiates a supersonically moving shock wave. The properties of air

as a compressible gas together with the high velocity of explosive detonation, rises the disturbance at the shock front until it is nearly discontinuous. This is a non-linear process which differs markedly from an acoustic wave (Baker et al., 1983). The magnitude and distribution of the blast load on a structure depends on:

- Explosive properties - type and mass
- Casing effects - a free air blast gives a more important peak pressure than an air blast from a cased charge. On the other hand, cased charge leads to fragments.
- Distance between detonation and protective structure
- Interaction with ground plane or structure

For military explosives the velocity of the detonation/shock wave ranges from 6700 to 8840 m/s, the pressure ranges from 18620 to 38620 MPa, while the temperatures range from about 3800 to 5700 K (Army, 1991).

2.2.1 Development of a shock-wave generated by a free explosion

After the reaction, the explosive is converted almost instantly in explosive gas which presents high pressure ($10^5 \div 3x10^5$ kgf/cm^2 and temperature ($3.5x10^3 \div 4x10^3$ C). (Henrych, 1979). The violent expansion of the gases means that all the air that surrounds the charge is expelled, and leads the development of compression waves in the surrounding air, and to the gradual conversion of chemical energy into mechanical energy, until the gas pressure reaches the atmospheric pressure. When this equality happens, the explosive

wave is not anymore supported by the gases, but flow continues to propagate independently. Since the air that surrounds the charge have an higher pressure, the explosive gases gradually stop and begin to go backward. In the return phase their pressure begin to increases again since overtaking the atmospheric pressure and returns the condition for the expansion of the gas and so on. This comports a free oscillation, that is called pulsation of the system of the explosive gas.

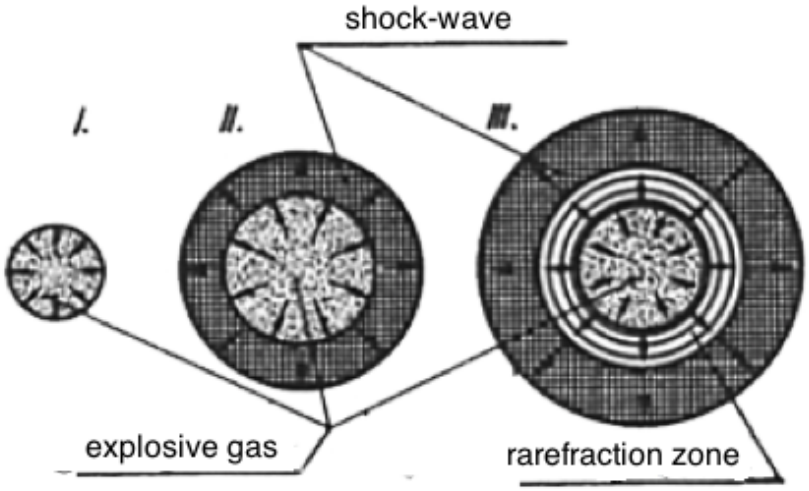

Figure 2.3: Detonation of a charge and shock-wave formation

2.3 Shock-wave parameters for a free field explosion

When an explosive is detonated in air, far away from any surface, a overpressure wave is generated that propagates with spherical shape. Instead, when a charge detonates on a rigid surface, without any other reflecting surfaces, an hemispheric overpressure wave is generated (Smith and Rose, 2002).

This two types of explosions are very important, because they represent the ideal shock-waves that are described and quantified detailed in the literature (Henrych, 1979; Harold and Brode, 1955; Kingery and Bulmash, 1984).

The main difference between the two typologies of explosion, is that, from a theoretical point of view, if the surface under the charge is considered prefectly rigid, the shock will be duplicated in comparison to the free explosion in air. Actually, instead, the direct contact between the charge and a generic surface causes a loss of energy, due to the formation of a crater on the surface itself.

The main parameters for the description of a shock-wave generated by an explosion are:

- The peak of positive overpressure
- The peak of negative overpressure
- The time arrival
- The duration of the positive and negative phase
- The positive and negative impulse

The impulse are defined as the integral of the positive and negative phase. All these quantities, are represented in the figure 2.4.

In the analysis of this trend, other factors are defined, like the shock front velocity and the Mach number of the wave, that are not necessary to evaluate the dynamics pressure that an explosion enforces to every surrounding solid.

It is evident that the pressure, the time arrival and the impulse, that are the three most important parameters of a free explosion in air, depend on the amount of detonating explosive and on the distance where are evaluated. We observe that the trend of the peak overpressure and the impulse decrease

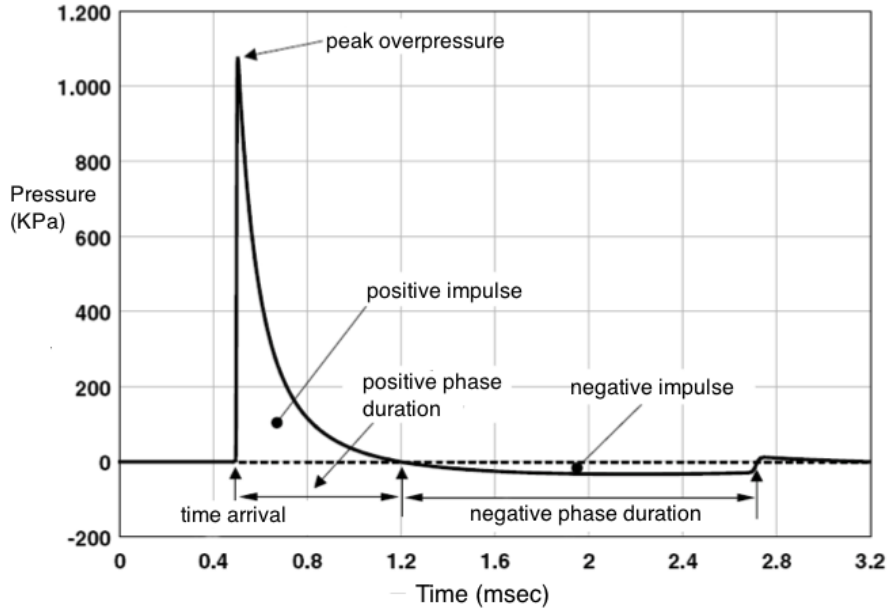

Figure 2.4: Typical trend of the overpressure

with the increasing of the distance, while in an almost specular way, the time arrival increases with the increasing of the distance, like show in figure 2.5 (Smith and Rose, 2002).

2.3.1 Numerical formulations to evaluate the overpressure in a free field

Many authors, trough accurate experimental analyses on the explosive phenomena, developed some formulations to compute the peak overpressure of a free field explosion in air. One of the most important is described in Henrych (1979).

The principal parameters of a shock-wave due to an explosion of an ideal gas in air, can be evaluated using the numerical method of H. Brode (Harold and Brode, 1955). He introduced the dimensionless parameters $\hat{p}$ (pressure),

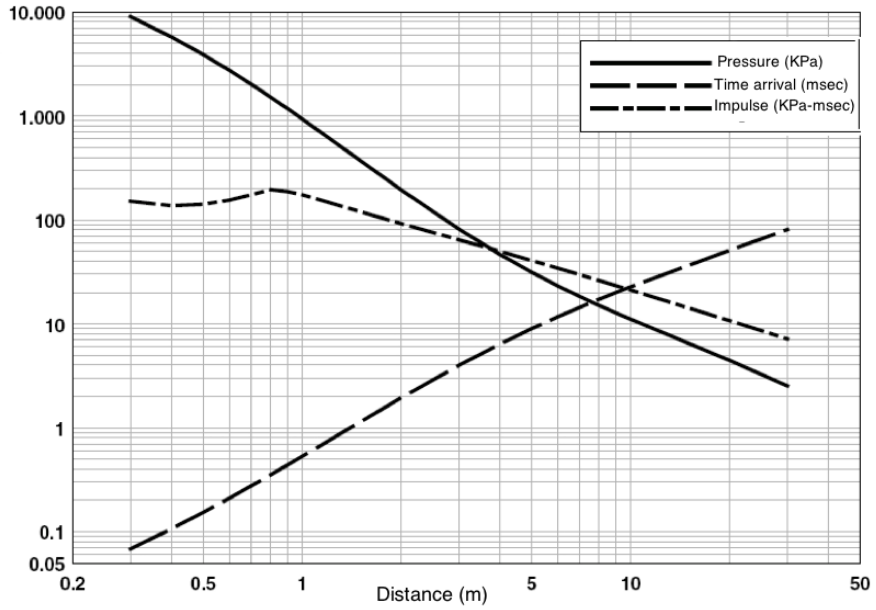

Figure 2.5: Trend of the overpressure, impulse and time arrival, for a 1Kg equivalent TNT

$\hat{\rho}$ (density), $\hat{u}$ (velocity), obtained trough the ratio of the values in the considered point and the atmospheric values p_o, ρ_0, c_{z0} (defined as "international atmospheric standard), where c_{z0} is the sound velocity. From the conducted analyses he evaluate some expressions that define the overpressure due to a free field explosion in air. Before reviewing these formula, we introduce the concept of scaled distance $\overline{R}$ and equivalent TNT weight.

Scaled distance and equivalent TNT weight

By scaling the parameters determined from experiments results, the results are generalized and thus can be used for the simulation of blasts of varying energy or varying distances. Essentially, Hopkinson (Army, 1991) introduce the idea that the behaviour of an explosion depends essentially on scaled

parameters $\overline{R}$ and W. In particular, the scaled distance is:

$$\overline{R} = \frac{R}{\sqrt[3]{W}} \qquad [m/Kg^{1/3}] \tag{2.1}$$

where R is the distance (range) from the explosive blast center and W is the weight of equivalent TNT of the charge.

Also it is possible to introduce an equivalent weight of explosive, depending on the different explosive characteristic:

$$W = \frac{W_s Q_{ws}}{Q_{wt}} \qquad [Kg] \tag{2.2}$$

where W_s is the weight of the real explosive, Q_{ws} is the specific heat of the real explosive, Q_{wt}, that is equal to $1000 Kcal/Kg$, is the specific heat of TNT.

Back to the experimental analyses, H.L.Brode (Harold and Brode, 1955) derived the sequent expressions, that define the overpressure due to an free field explosion in air. The peak overpressure $[kp/cm^2]$of the shock-wave Δp_ϕ can be written in the form:

$$\begin{aligned} \Delta p_\phi &= \frac{6.7}{\overline{R}^3} + 1 \quad for \qquad \Delta p_\phi \geq 10 \\ \Delta p_\phi &= \frac{0.975}{\overline{R}} + \frac{1.455}{\overline{R}^2} + \frac{5.85}{\overline{R}^3} - 0.019 \quad for \quad 0.1 \leq \Delta p_\phi \leq 10 \end{aligned} \tag{2.3}$$

$$\Delta p_\phi = p_\phi - p_0 \tag{2.4}$$

where $\overline{R}$ is the scaled distance $[m/kg^{1/3}]$ between the considerate point and the center of the charge, W is the equivalent TNT charge $[Kg]$, p_ϕ is the pressure on the front of the shock-wave and p_0 is the atmospheric pressure.

It is possible to compare equations (2.3) with others written by other authors:

$$\Delta p_\phi = \frac{10.7}{\overline{R}^3} - 1 \quad [kp/cm^2]\ for \qquad \overline{R} \leq 1$$
$$\Delta p_\phi = \frac{0.76}{\overline{R}} + \frac{2.55}{\overline{R}^2} + \frac{6.5}{\overline{R}^3} \quad [kp/cm^2]\ for \qquad 1 \leq \overline{R} \leq 15 \tag{2.5}$$

The first formula has been derived by Naumyenko and Petrovsky (1956) and the second one by Sadovsky (1952). They achieved the formulations from the develop of similar model and the coefficent have been derived experimentally. Another formulation, mostly used for the evaluation of the peak overpressure in free air was supplied by Henrych (1979). He on the basis of experimental results developed the following formulations:

$$\Delta p_\Phi = \frac{14.0717}{\overline{R}} + \frac{5.5397}{\overline{R}^2} - \frac{0.3572}{\overline{R}^3} + \frac{0.00625}{\overline{R}^4} \quad [kp/cm^2] \quad for \quad 0.05 \leq \overline{R} \leq 0.3$$
$$\Delta p_\Phi = \frac{6.1938}{\overline{R}} - \frac{0.3262}{\overline{R}^2} + \frac{2.1324}{\overline{R}^3} \quad [kp/cm^2] \quad for \quad 0.3 \leq \overline{R} \leq 1 \tag{2.6}$$
$$\Delta p_\Phi = \frac{0.622}{\overline{R}} + \frac{4.05}{\overline{R}^2} + \frac{3.288}{\overline{R}^3} \quad [kp/cm^2] \quad for \quad 1 \leq \overline{R} \leq 10$$

that are right again for charges in equivalent TNT weight.

The values of the last formulation give , for a chemical explosion of TNT,information about what happens for all the values of $\overline{R}$ until the center of the charge (on the surface of the charge, $\overline{R} \approx 0.05$ and $\Delta p_\Phi = 640\ kp/cm^2$). In the abacus shown in 2.6 the typical trends of all the main parameters of a shock-wave with no limit of $\overline{R}$ are represented.

Between the interval $1 \leq \overline{R} \leq 10$ these formulations can be used for all the chemical or nuclear explosives, giving similar results. The research job

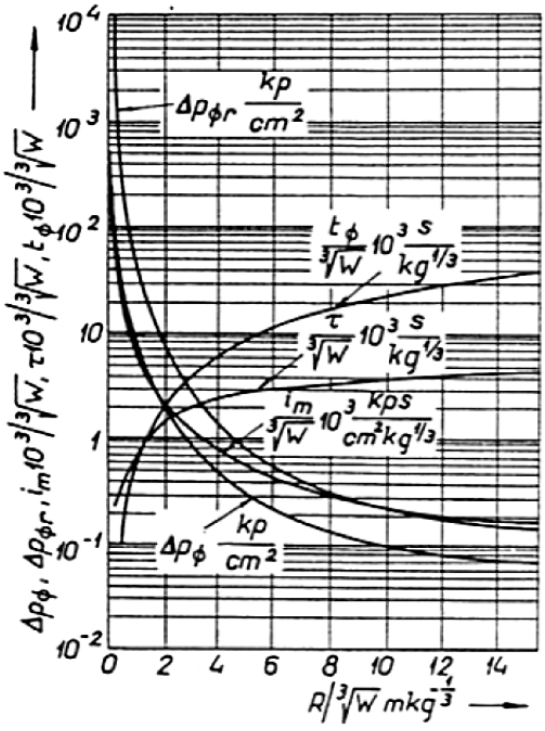

Figure 2.6: Trend of the incident overpressure , Δp_Φ, reflected overpressure $\Delta p_{\Phi r}$, impulse i_m , time arrival t_ϕ and positive phase duration τ [ref]

on the explosions of TNT charges made by Henrych allows to derive the formulation to evaluate the duration of the overpressure $\tau[s]$:

$$\frac{\tau}{\sqrt[3]{W}} = 10^{-3}\left(0.107 + 0.444\overline{R} + 0.264\overline{R}^2 - 0.129\overline{R}^3 + 0.0335\overline{R}^4\right) \quad 0.05 \leq \overline{R} \leq 3 \tag{2.7}$$

where $\frac{\tau}{\sqrt[3]{W}}$ measured in $[s/kg^{1/3}]$, is a scaled time.

The surface under the curve overpressure-time is defined as specific impulse i_m of the shock-wave. For (Sadovsky, 1952)

$$i_m = \int_0^t \Delta p\,(t)\ dt = A\sqrt[3]{\frac{W^2}{R}} \qquad [kp\cdot s/m^2] \qquad \overline{R} > 0.5$$
$$i_m = \frac{15W}{R^2} \qquad [kp\cdot s/m^2] \qquad \overline{R} < 0.25 \tag{2.8}$$

Where A = 34 ÷ 36 is a constant.

For Henrych the formulations are:

$$\frac{i_m}{\sqrt[3]{W}} = 663 - \frac{1115}{\overline{R}} + \frac{629}{\overline{R}^2} - \frac{100.4}{\overline{R}^3} \qquad [kp\cdot s\cdot m^{-2}\cdot kg^{-1/3}]\ for\ 0.4 \le \overline{R} \le 0.75$$
$$\frac{i_m}{\sqrt[3]{W}} = -32.2 - \frac{211}{\overline{R}} + \frac{211}{\overline{R}^2} - \frac{80.1}{\overline{R}^3} \qquad [kp\cdot s\cdot m^{-2}\cdot kg^{-1/3}]\ for\ 0.75 \le \overline{R} \le 3 \tag{2.9}$$

The shock-wave is followed by an rarefaction or depression wave for according to the relation:

$$0 < \overline{p}_{min} < p_0 = 1\ atm \tag{2.10}$$

where $\overline{p}_{min} > 0$ is the minimum pressure of the rarefaction wave. So an under-pressure $\Delta\overline{p}_{min}$ is defined, that is given by:

$$\Delta\overline{p}_{min} = \overline{p}_{min} - \overline{p}_0 < 0 \tag{2.11}$$

From the theoretical works by Brode (Harold and Brode, 1955) and from the experimental did by Henrych (1979), the following approximate relationships are obtained:

$$\Delta\overline{p}_{min} \approx -\frac{0.35}{\overline{R}} \quad [kp/cm^2] \quad \overline{R} > 1.6\ m/kg^{1/3}$$

$$\overline{\tau} \approx 4.25\frac{\sqrt[3]{W}}{c_{z0}} = 1.25x10^{-2} \cdot \sqrt[3]{W} \quad [s] \tag{2.12}$$

$$\overline{i} \approx i_m \left(1 - \frac{1}{2R}\right) \quad [kp \cdot s/m^2]$$

$$\overline{\lambda} \approx 340\overline{\tau}$$

where $\overline{\tau}$ is the duration of the negative phase, $\overline{i}$ is the specific impulse of the rarefaction wave , and $\overline{\lambda}$ is the length of the rarefaction wave. The time dependence of the entire explosive wave (shock and rarefaction wave) can be express by the analytic relation:

$$\Delta p(t) = \frac{\Delta}{p_\phi} cos\overline{\alpha}_i e^{-f(t/\tau)} cos\left(\alpha_t \frac{t}{\tau} + \overline{\alpha_t}\right) \tag{2.13}$$

where the function $f\,(t/\tau)$ and the constants $\overline{\alpha_t}$ and α_t depend on the shape of overpressure and on the values of τ and $\overline{\tau}$. In particular, the parameters $\overline{\alpha_t}$ and α_t are determined from the condition that, at point $t = \tau$ and $t = \tau + \overline{\tau}$, the value of $\Delta p(t)$ have to be equal to 0.

Kingery (Kingery and Bulmash, 1984) calculates the shock front velocity depending on pressure as :

$$u = c_0 \left(1 + \frac{\gamma + 1}{2\gamma}\frac{p_{max}}{p_0}\right)^{1/2} \tag{2.14}$$

where

- The parameter γ (ratio of specific heat of air) depend also on the overpressure and can be taken from a table in (Kingery et al., 1964) and is

defined as :

$$\gamma = \frac{c_p}{c_v} \tag{2.15}$$

with c_p being the specific heat at constant pressure and c_v the specific heat at constant volume. Both the specific heat ratio and the speed of sound depend on the temperature, the pressure, the humidity, and the CO_2 concentration. Kingery and Bulmash (1984) defines the variation of the specific heat ratio with a range of 1.402 to 1.176

- c_0 is the sound velocity in air (331 m/sec)
- p_{max} is the peak of the overpressure
- p_0 is the atmospheric pressure (101.3 KPa)

2.4 Reflection of a Shock-Wave

When a shock-wave impacts in perpendicular way on a rigid surface infinitely extended, the direction of the air flow in the shock-wave is progressively inverted by increasing the static pressure on the surface and generating a reflected pressure wave. This phenomenon is called "loading on the face" and the assessment of reflected pressures in calculations of the load generated by the outbreak, is very important as it can be 20 times higher than the pressure incident, depending on the strength of the incident pressure. When the whole phenomenon of reflection is complete, the reflected wave back toward to the source of the explosion. In reality, however, it is very unlikely that the shock wave generated by an explosion would affect an entire surface with a zero angle, and is much more likely to impact with an angle of incidence greater than zero.

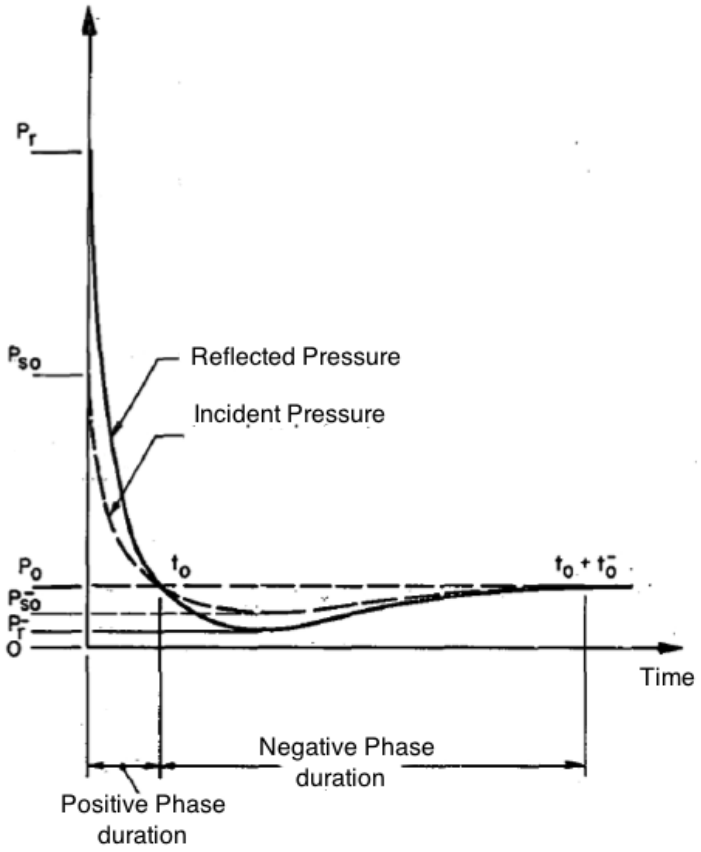

Figure 2.7: Typical trend of the incident and reflected wave (ref9)

Depending on the angle of incidence, two distinct situations may occur: at shallow angles (typically $< 40 \circ$) it generates a regular reflection where the incident wave precedes the wave reflected from the surface; at angles of incidence higher, it generates a wave of Mach following the union of the shock wave incident and the reflected one. The configuration where most commonly can be observed the formation of a wave of Match is the one where the charge is placed at a certain height from the ground, therefore the parameter that affects the formation of the aforementioned wave is H_c (i.e. the distance between the charge and the surface).

This scheme is shown in Figure 2.8, where are indicated the incident wave and reflected and is illustrated the formation of the branch of Mach. A practical example that can arise in such a situation can be represented by the detonation of a charge in an urban environment. It is obvious that only a few surfaces of buildings will be affected by the shock wave orthogonally, while most will be hit by a shock wave with an angle of incidence greater than zero.

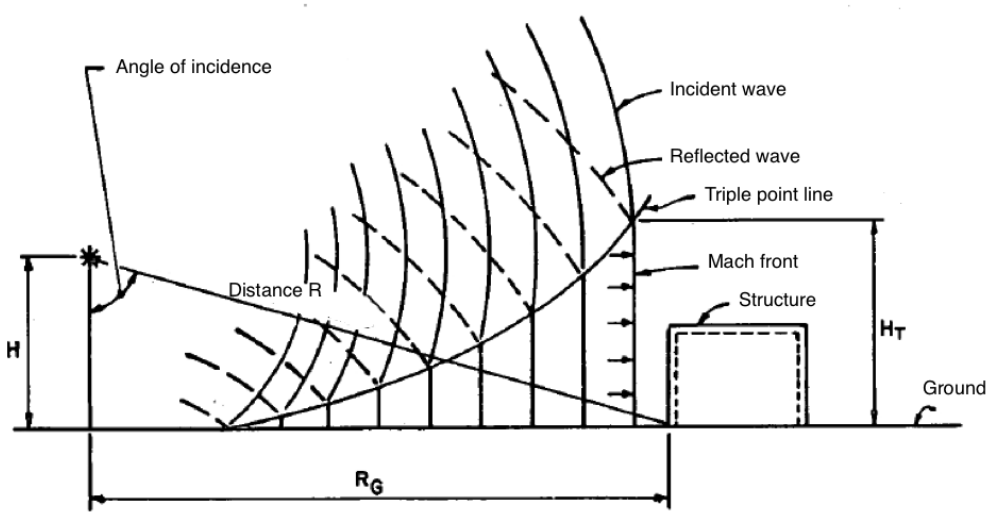

Figure 2.8: Schematic representation of the Mach front formation (ref9)

2.4.1 Normal Reflection

In the shock wave the air particles are compressed and in continuous motion, therefore in the normal incidence of the wave with a rigid barrier the reflected overpressure will become greater than the one existing in the wave before the incidence. The parameters of the atmosphere at rest are: p_0,ρ_0 ,T_0 ,$u_0 = 0$ and the parameters of the incident wave are p_ϕ ,ρ_ϕ ,T_ϕ ,u_ϕ. At the instant of

the impact of the shock front on the barrier, a reflecting wave is produced that propagates in the opposite direction. The parameters of this front are denoted as N_r,$p_{\phi r}$,$\rho_{\phi r}$,$T_{\phi r}$,$u_{\phi r}$ (Henrych, 1979). Just before the incidence, it is possible to write ,for the incident shock front, the sequent relationship:

$$u_\phi = \sqrt{(p_\phi - p_0)\left(\frac{1}{\rho_0} - \frac{1}{\rho_\phi}\right)} \tag{2.16}$$

and just after the incidence :

$$u_\phi + u_{\phi r} = \sqrt{(p_{\phi r} - p_0)\left(\frac{1}{\rho_0} - \frac{1}{\rho_{\phi r}}\right)} \tag{2.17}$$

Using the adiabatic shock, the solution of the equation (2.17) can be written as follows:

$$\Delta p_{\phi r} = p_{\phi r} - p_0 = 2\Delta p_\phi + \frac{6\Delta p_\phi^2}{\Delta p_\phi + 7p_0} = \frac{8\Delta p_\phi^2 + 14\Delta p_\phi}{\Delta p_\phi + 7.2} \tag{2.18}$$

where Δp_ϕ expressed in $[kp/cm^2]$. Following this formulation, the ratio $\Delta p_{\phi r}/\Delta p_\phi$ is between 2 and 8.

2.4.2 Oblique Reflection

In the oblique incidence of the shock wave, the reflection phenomenon is very complex and therefore, accurate results can be obtained only by experimental testing. In order to determine the quantitative parameters of the phenomenon, the speed of the particles of the incident wave front, u_ϕ , is shifted into two components, one parallel to the surface of incidence, namely $u_{\phi 1}$, and are normal to the surface, namely $u_{\phi 2}$. The normal component is reflected according to the rules described in the previous paragraph. The tangential component, instead, generates a motion of the compressed air

along the surface, moving to the right of the vertical reflected particles. The reflected shock front propagates in the compressed air and preheated by the incident wave; It propagates with a higher velocity than the incident wave and accordingly we observe that $\beta > \alpha$ (2.9 (a)). The point A, intersection between the reflected fronts and incidents, and the barrier surface, moves on the surface with the velocity:

$$c_A = \frac{N}{sin\alpha} \tag{2.19}$$

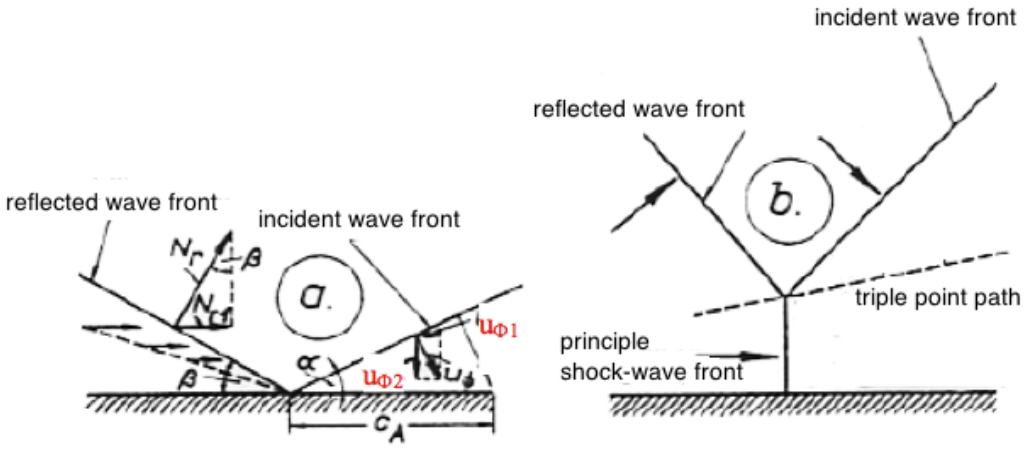

Figure 2.9: Reflection of an incident wave (a); Formation of the Mach wave front (b);

The tangential component of the incident wave velocity is $u_{\phi 1} = u_\phi \, sin\alpha$, while the normal component is $N_{r1} = N_r \, sin\beta$. We consider a small incident angle α, it results $N_{r1} < c_A$, so with the increment of α the velocity c_A decreases, and with the increment of β the velocity N_{r1} increases. At a certain angle α, that depends on the overpressure of the incident wave front, the velocity N_1 is equal to c_A, and their intersection point generates the point A. From at the instant when $N_{r1} = c_A$, with another increment of α, the point A moves away from the barrier, generating new shock-wave, and

such a composition of the incident and reflected wave is denoted "principle of *Mach*" . The front of this wave moves along the surface of the barrier bringing with itself the *triple point*, that is the intersection of the three wave. If the incident wave front starts from a point that belongs to the barrier surface (intersection point A), the reflection is defined as "double impact" or "regular reflection". For a Mach wave, as is shown in the figure 2.10 , the reflection is called "triple impact" or "non regular reflection".

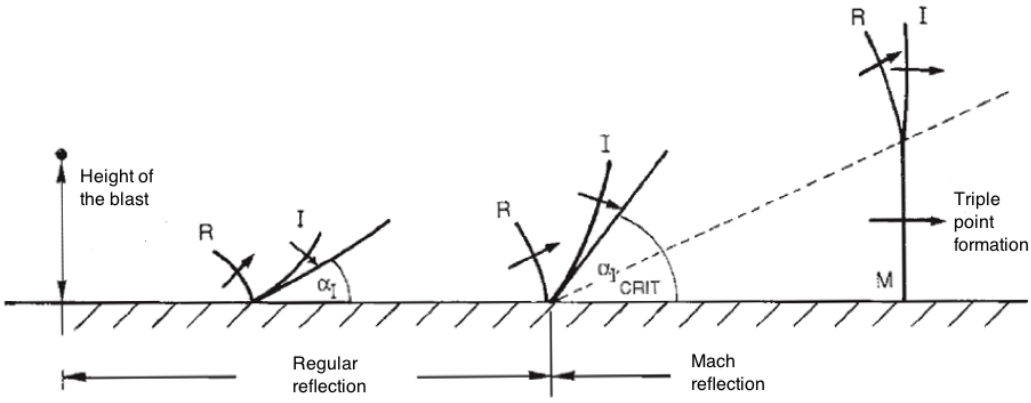

Figure 2.10: Schematich representation of the regular reflection and the non-regular reflection (Smith and Rose, 2002)

In the figure 2.11 (a) it is shown how the boundary of the two types of reflection depends on the overpressure Δp_ϕ and the angle α between the incident wave front and the barrier. The reflected overpressure $\Delta p_{\phi r}$ can be evaluated as:

$$\Delta p_{\phi r} = k_r \cdot \Delta p_\phi \tag{2.20}$$

where k_r is defined as amplification coefficient.

From the graphic shown below 2.11 (b) it is possible to derive the coefficient of amplification k_r, against the variation of α. It is evident that

the maximum increment of the overpressure is verified when $\alpha = 0$ or when $\alpha = 40 \div 70°$, that corresponds with the transition between the regular and non-regular reflection. The impulse of the reflected shock-wave is computed with the sequent formulations:

$$i_r = A\frac{\sqrt[3]{W^2}}{R}\ [kp \cdot s/m^2] \quad R \geq 0.5\sqrt[3]{W}[m]$$
$$i_r = 24\frac{W}{R^2}\ [kp \cdot s/m^2] \quad R \leq 0.25\sqrt[3]{W}[m] \tag{2.21}$$

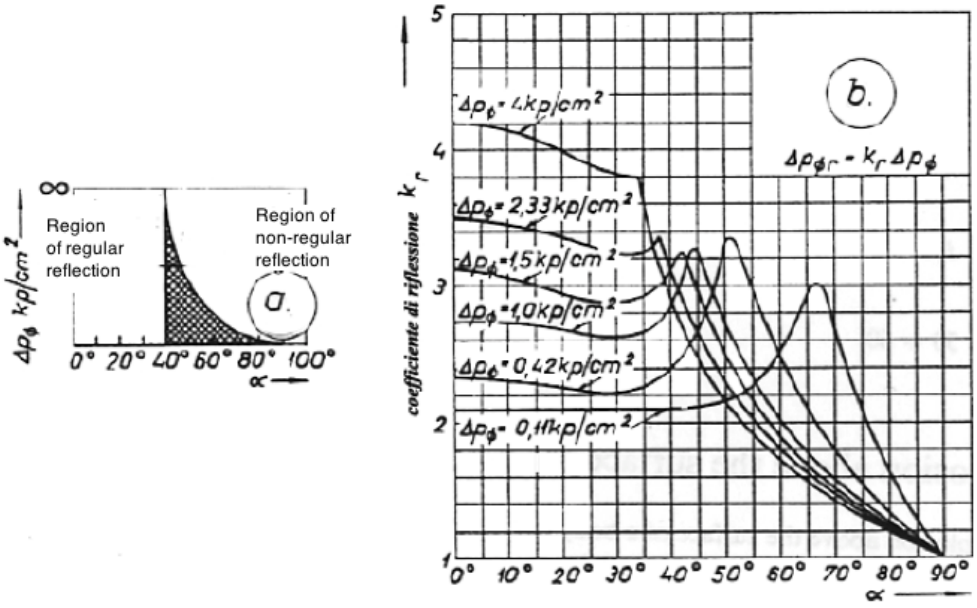

Figure 2.11: boundary between regular and non-regular reflection as a function of α and Δp_ϕ (a); representation of the amplification coefficient k_r as a function of α and Δp_ϕ (b);

2.5 Shock-Waves effects in the impact by a generic solid

2.5.1 Interaction of the shock-wave with a finite solid

Probably the simplest scenario that can be analyzed in the case of loading due to an explosion is the one of a solitary building (or set of buildings far apart), oriented in the direction of the explosion, and loaded by a wave of ideal shock (2.12). In a situation like this we observe a particular phenomenon on the face directly subjected to the explosion.

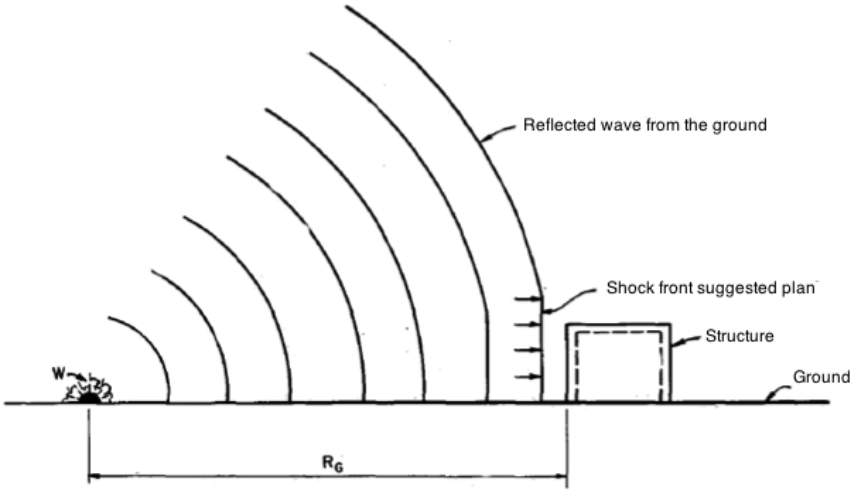

Figure 2.12: Graphic representation of the interaction between the shock-wave with a generic solid

In fact, unlike what happens on infinite surfaces, the pressure acting on the front face of the building is reduced by the pressure acting on the side faces. This also leads to a reduction in the positive phase and then the "time of cancellation" occurs before. The result of these complex interactions between the waves is that the total loading on the front face (the impulse)

is lower than that assumed on that face, but higher than that the one is generated on the side faces. The main factors that define the trend of the pressure and the duration of the time of cancellation are basically the mass of the charge, the distance of the load from the building and the dimensions of the front face of the building. Figure 2.13 shows the comparison between two pressure-time diagrams on the central face of a building considering at first a face of infinite extensions and then one finite face.

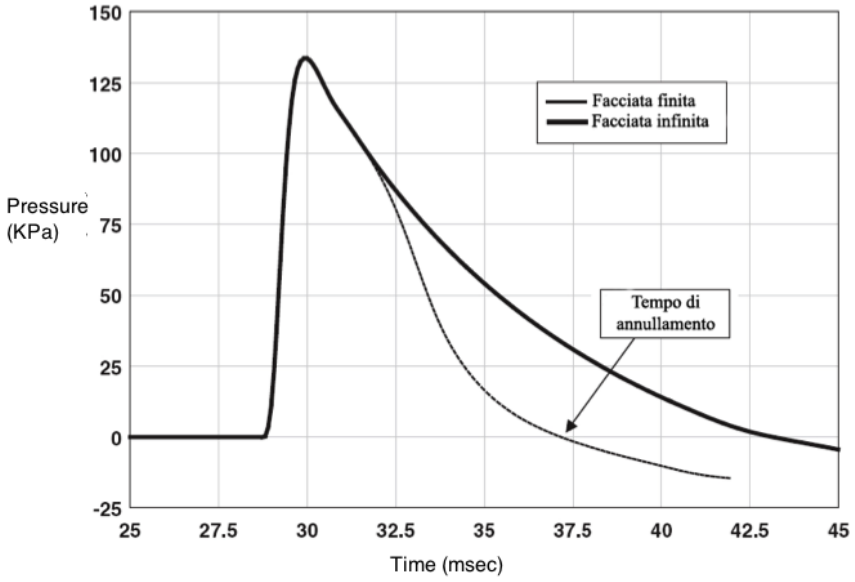

Figure 2.13: Trend of the pressure with the time on a finite and infinite surface

2.5.2 Pressure distribution on the front and rear surface

The effects of a shock-wave (Henrych, 1979) on structures differs accordingly with the intrinsic characteristics of the type of the explosive used, the distance of the point of explosion, the size of the feedstock and the shape of the body. Since a theoretical solution of the problem has not been yet proposed, in the following we present only experimental results obtained in rooms of explosion

(Army, 1991). With reference to the figure 2.14, in the area nearest to the explosion, the structures are subjected to the effects of the incident wave. The structure is at first stressed by the pressure reflected from the top, then the shock wave reaches the surface of the ground (at the time greater than $H/c_{z\phi}$) by immersing the entire structure in a layer of compressed air which apply on the structure a stress state in all directions (omnidirectional) resulting from the reflected overpressure.

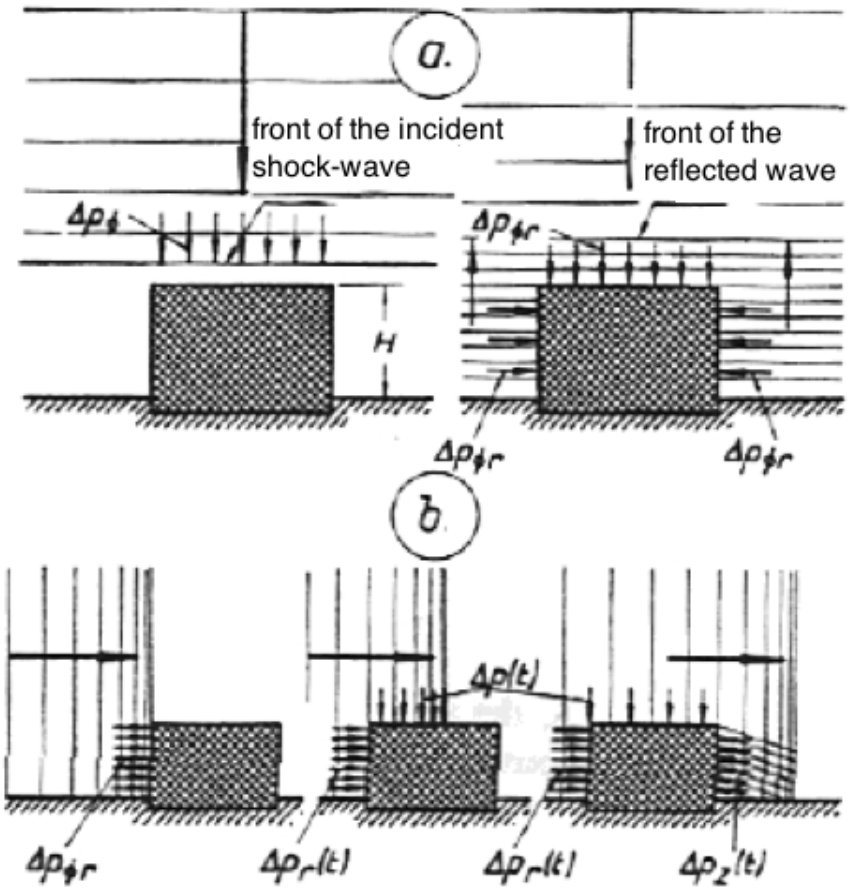

Figure 2.14: Effects of a shock-wave on the surfaces of a generic solid: (a) action of the wave for an explosion very near to the ground ;(b) action of the incident wave in a non-regular reflection

The tension that occurs on the surface of the structure subjected to the effects of the main wave and the tension that instead occurs upon contact with the reflected shock-wave are evidently different. In fact, the wall that faces the epicenter of the explosion (2.14 (b)) is stressed by the reflection of the overpressure of the shock wave which propagates along the surface. So the overpressure acts gradually first on the lateral walls, then on the upper horizontal surface (i.e on the roof), and then on the backward surface. After the shock wave has hit the front wall, the wall is bypassed and the action of pressure on it decreases rapidly. The effect of the impact on the front wall fades after the time:

$$\Delta t_1 = \frac{3x}{c_{z\phi r}} \tag{2.22}$$

where x is the smallest between the two dimension $B/2$ and H that are shown in the figure 2.15, while $c_{z\phi r}$ is the sound velocity of the reflected shock-wave given by the formula:

$$c_{z\phi} = 20.1\sqrt{T_\phi} \tag{2.23}$$

After this instant, the action of overpressure on the front of the wall is given by the sum of the overpressure of the incident wave and the velocity of impact of the overpressure amplified by a pressure coefficient k_p $(0.8 \div 1)$. When the shock wave reaches the rear wall, it begin to create the vortices at the edges and due to this phenomenon of suction a reduction of the overpressure occurs . The overpressure on the back of the wall increases with time and reaches the maximum at the time:

$$\Delta t_2 = \frac{5x}{c_{z\phi r}} \tag{2.24}$$

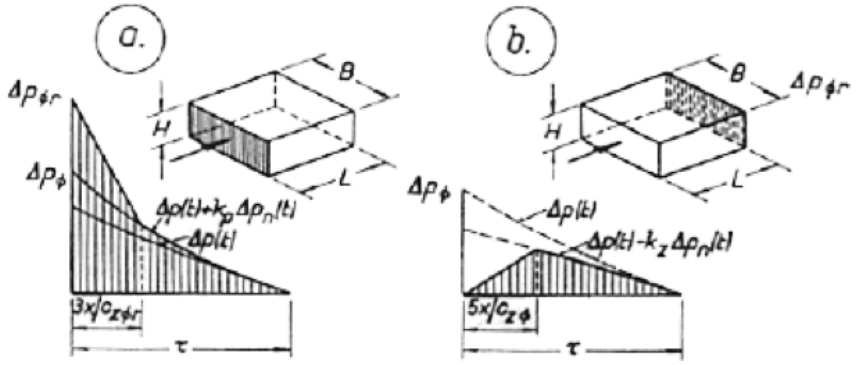

Figure 2.15: (a) Trend of the pressure by time on the front surface of the considering solid ;(b) Trend of the pressure by time on the back surface of the considering solid

The dependence of the overpressure from the time on the back of the wall can be considered as shown in figure 2.15. Finally, we can define the values of the pressure on the body as the difference between the pressure in front and the one on the back of the wall. The shift of the time step (i.e. the time interval in which the passage of the overpressure occurs) between the beginning and the end of the overpressure is:

$$\Delta t_3 = \frac{L}{N} \tag{2.25}$$

Chapter 3

Numerical Methods and Introduction to Fluid Structure Interaction problems

3.1 Numerical Methods and Element Formulation

The following sections show the theory behind the numerical methods used in this paper. First there will be a description of the numerical time integration and the attributes of explicit and implicit methods. After this we make an introduction to the Fluid Structure Interaction problems, with some theory and methods used to resolve this kind of problems. We do this because some problems, e.g. the interaction of pressure waves with structures, that we will face in the sequent sections are solved using this theory. In what follows we restrict to the case of Finite Elements Methods. Then we compile a summary of the three different Finite Element Formulations, that are:

- Lagrangian Formulation
- Eulerian Formulation
- Arbitrary Lagrangian Eulerian (ALE) formulation

The difference between these formulations stems from how the mesh conforms to material motion. A particular care will be given to the ALE methods, because is the most used for the Fluid-Structures Interaction problems.

3.1.1 Explicit method

LS-DYNA mainly uses explicit time integration to solve nonlinear dynamic problems, e.g. explosions/blast loading. This section is based in particular on LS-DYNA theory manual (Hallquist, 2006). In implicit methods, the equations of dynamics are combined with the time integration operator, and the displacements are found directly. In explicit methods, on the contrary, at first the accelerations are determined from the equations of dynamics and then integrated to obtain the displacements. The implicit methods require solution of a set of non-linear algebraic equations at each time step. Furthermore, iterations need to be performed for each time step of implicit integration to control the error and prevent divergence. Therefore, the number of numerical operations per each time step can be three orders of magnitude larger than for explicit integration. Thus, the advantage of implicit method for three-dimensional ,transient, problems becomes marginal (Miller and Joldes, 2006). This means that each time increment is computationally inexpensive and iterative convergence is not an issue. All the explicit methods are conditionally stable, that means that a limitation to the time increment always exist. If the critical time step Δt_{cr} ,defined in the following lines, is exceeded, the numerical process becomes unstable. Because of the small time increments

required, explicit methods are ideal for high-speed dynamics simulations, like explosions.

The semi-discrete equation of motion of a $MDOF$ (multi degrees of freedom) system is:

$$[M]\{\ddot{u}(t)\} + [C]\{\dot{u}(t)\} + \{R^{int}(t)\} = \{R^{ext}(t)\} \tag{3.1}$$

where:

- M is the Mass matrix
- C is the Damping matrix
- u, $\dot{u}$, $\ddot{u}$ are respectively the displacement, velocity and acceleration
- R^{int} is the Internal force vector, $K * u$ in case of linear elastic material, where K is the stiffness matrix
- R^{ext} is the External force vector

$LS-Dyna$ uses the explicit central difference scheme to integrate the equations of motion. For the central difference method to be explicit, lumped mass have to be employed. This eliminates solution of equations and increases the critical time increment.

$$\ddot{u}^n = M^{-1}(R^n_{ext} - C\dot{u}^n - R^n_{int}) \tag{3.2}$$

$$\dot{u}^{n+1/2} = \dot{u}^{n-1/2} + \ddot{u}^n \Delta t^n \tag{3.3}$$

$$u^{n+1} = u^n + \dot{u}^{n+1/2} \Delta t^{n+1/2} \tag{3.4}$$

$$\Delta t^{n+1/2} = \frac{1}{2}\left(\Delta t^n + \Delta t^{n+1}\right) \tag{3.5}$$

The geometry is updated by adding the displacement increments to the initial geometry. The critical time increment for the central difference method is determined from the highest natural frequency ω_{max} and the damping ratio ζ.

$$\Delta t_{cr} \leq \frac{2}{\omega_{max}} \left(\sqrt{1 - \zeta^2} - \zeta \right) \tag{3.6}$$

For an non damped system, the critical time increment becomes:

$$\Delta t_{cr} \leq \frac{2}{\omega_{max}} = \frac{L}{c_d} \tag{3.7}$$

where L is the element length and c_d is the speed of sound in the material. The critical time increment have to be small enough that the information does not propagate more than one element length during a single time step.

3.2 Introduction to the Fluid Structure Interaction (FSI) problems

3.2.1 Introduction

In fluid-structure interaction (FSI) problems, one or more solid structures interact with an internal or surrounding fluid flow. FSI problems play prominent roles in many scientific and engineering fields, yet a comprehensive study of such problems remains a challenge due to their strong non-linearity and multidisciplinary nature. For most FSI problems, analytical solutions to the model equations are impossible to obtain, whereas laboratory experiments are limited in scope; thus to investigate the fundamental physics involved in the complex interaction between fluids and solids, numerical simulations may be employed (Richter, 2010). Fluid-structure interaction problems describe the coupled dynamics of fluid mechanics and structure mechanics. They are

classical multi-physics problems. First of all we have do give the definition of a coupled system.

A coupled system S is one in which physically or computationally heterogeneous mechanical components interact dynamically. By S_1 and $S2$ we denote two subsystems. The coupled system S is called one-way, if there is no feedback between the subsystems and two-way, if there is feedback between the subsystems. The concept of coupled systems can be generalized to multi-coupled systems with subsystems ($S1$, . . . , S_N) . This can be multi-structure-fluid interaction, fluid-structure-fluid-interaction (e.g. water-boat-air). We then call a fully coupled system multi-way coupled. In most problems it cannot be decided if the problem is one-way or two-way. Regarding the interaction of a very slow driving car with the surrounding air, the influence of the air on the car can be neglected. At a certain speed however, the aerodynamic resistance plays an important role.

The numerical procedures to solve these FSI problems may be broadly classified into two approaches: the monolithic approaches and the partitioned approaches. It is understood that the distinction between the monolithic and partitioned approaches may be viewed differently by researchers from different fields. In this paper, we intend to define these two approaches from the engineering application point of view. The monolithic approach treats the fluid and structure dynamics in the same mathematical framework to form a single system of equations for the entire problem, which is solved simultaneously by a unified algorithm. In contrast, the partitioned approaches treat the fluid and the structure as two computational fields which can be solved separately with their respective mesh discretization and numerical algorithm. The interfacial conditions are used explicitly to communicate information between the fluid and structure solutions.

3.2.2 Fluid-Structure Interaction

In the following, we introduce a prototypical fluid-structure interaction problem: figure 3.1 shows a flow domain with an obstacle. We call the common domain Ω, the flow domain Ω_f and the structure domain Ω_s

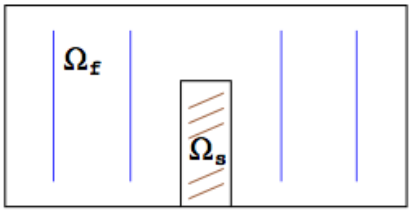

Figure 3.1: Fluid-structure interaction domain

Now assume that the fluid domain Ω_f is filled with air, and Ω_s is a rigid moving body of steel. This movement will set the fluid into motion. The air however will not significantly act on the obstacle:

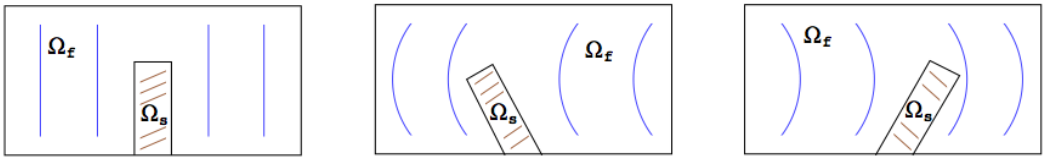

Figure 3.2: Fluid motion imposed by moving structure

This problem is a one-way fluid-structure interaction problem. The movement of the structure controls the motion of the fluid but the fluid's motion does not impair the movement of the structure.

Next assume, that the flow is driven by an inflow condition and the obstacle is an elastic structure. The evolving flow will act on the surface of the structure and will cause a deformation. This deformation changes the flow domain:

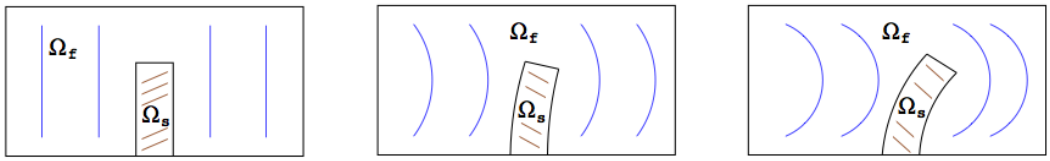

Figure 3.3: Fluid-structure interaction

Due to the deformation of the obstacle, the flow domain is altered. Here, there is a real feedback between both subsystems and the coupling is two-way. Both coupled problems have in commons, that they are formulated on moving domains. Here, the common domain Ω keeps the same, but the subdomains of the fluid Ω_f and the solid Ω_s problem change with time: $\Omega = \Omega_f(t) \cup \Omega_s(t)$. This is one of the main difficulties connected with the modelling of fluid-structure interaction problems as well the design of numerical methods for their solution. The different degree in coupling and interaction is important for the treatment of the problems. We will consider all fluid-structure interaction problems as time-dependent problems $S(t)$. The solution is approximated at time-steps $t_1, t_2, \ldots$:

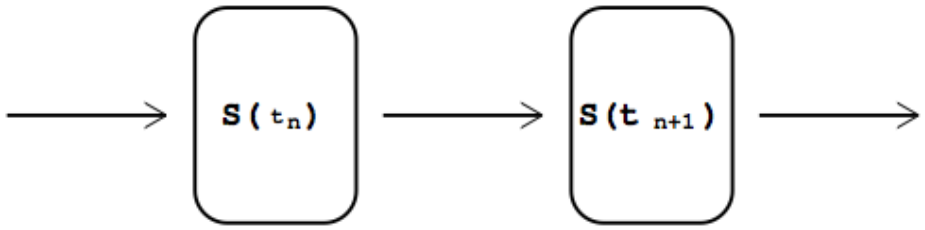

Figure 3.4: Time-approximation of the coupled problem

In every time-step $t_n \longrightarrow t_{n+1}$ both problems need to be solved. The

solution S_{n+1} depends on the state of both sub-problems at time t_n as well as on the interaction between both sub-problems. The straightforward way for simulation the coupled problem is the monolithic approach: we simultaneously solve the fluid and the structure problem at the same time.

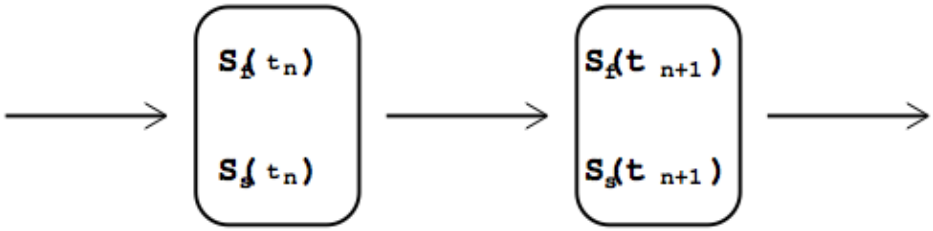

Figure 3.5: Monolithic solution of the coupled system

For this approach, we need to formulate both sub-problems, fluid and structure, as one combined problem. Sometimes however the coupling between both problems suggests a staggering of the solutions. Considering the problem described in Figure 3.5, the flow field has no influence on the body, which is moved by some external mechanism. Here, it may be advisable to first solve for the new shape of the structure and flow domain and then for the flow field:

This configuration can now be treated with standard methods: the structure deformation is computable with a structure solver, the flow problem can be computed separately with a fluid dynamics code. Unfortunately, interesting fluid-structure interaction problems are mostly two-way coupled. Still, it is possible to numerically decouple the interaction problem. These methods are called partitioned approaches:

In every time-step $t_n \longrightarrow t_{n+1}$ both problems are solved separately. The

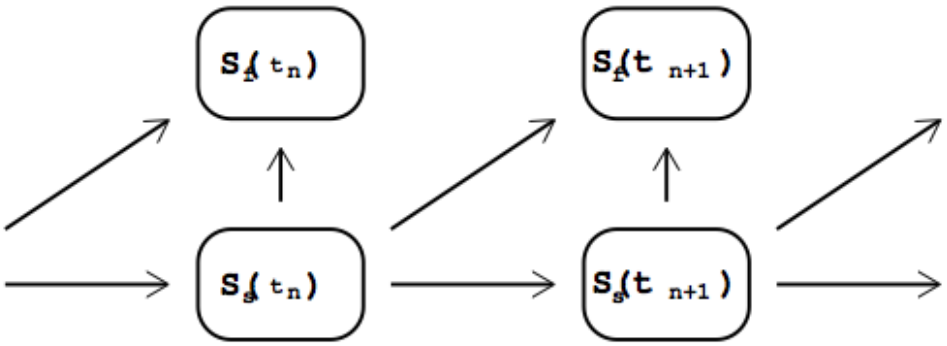

Figure 3.6: Staggered solution of the coupled system

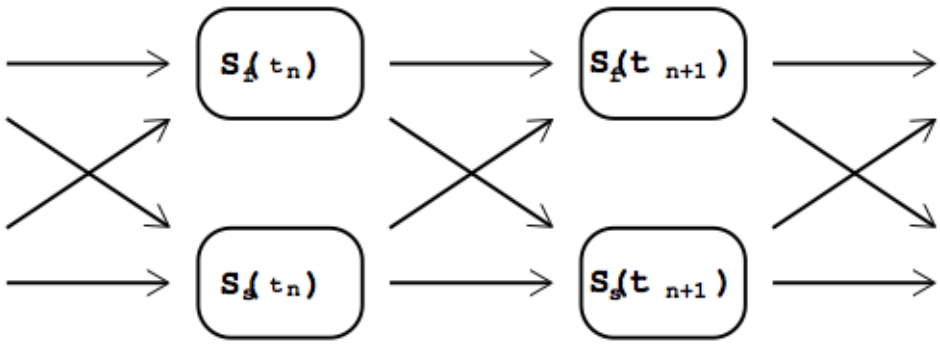

Figure 3.7: Partitioned solution of the coupled system

flow problem S_f at time $t_n + 1$ depends on the flow and on the structure problem at time t_n, but the interaction at time t_{n+1} is not taken into account. For the structures problem the same approach is used. In terms of time-stepping methods this approach can be called a semi-explicit approach: while the fluid and structure dynamics itself is considered in an implicit fashion, the interaction between both problems is included in an explicit way giving rise to stability problems and asking for small time steps. An advantage of the partitioned approach is that different solvers can be used for the different sub-problems. The coupling between fluid and structure comes into the problem by means of boundary conditions on the interface between both sub-domains. Aside, this decoupling allows for a parallel solution of the fluid and the structure problem. However, in most applications the coupling between both problems is too strong for partitioned approaches.

A further development of the partitioned approaches are the strongly coupled partitioned approaches. The two sub-problems are solved independently in a decoupled way. Every time-step $t_n \longrightarrow t_{n+1}$ is however iterated yielding approximate solutions $\mathbf{S}(t_{n+1})_f^i$ and $\mathbf{S}(t_{n+1})_s^i$. To compute the $i - th$ iterative, the solution at time t_n and the last approximations $\mathbf{S}(t_{n+1})_f^{i-1}$ and $\mathbf{S}(t_{n+1})_s^i$ are considered:

The strongly coupled partitioned approach still allows for the use of different solvers for the fluid and structure dynamics subsystem. Due to the outer iteration, stability problems are damped, even though not removed. If a very large number of sub-iterations is necessary to find the stable state, the strongly coupled partitioned approach can be less efficient than the monolithic solution of the coupled problem.

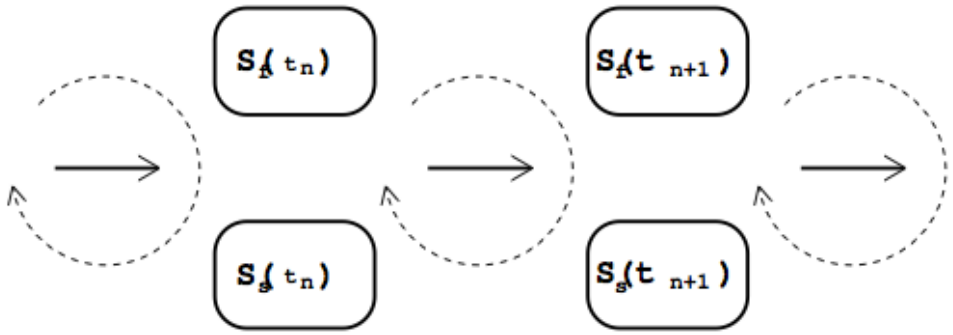

Figure 3.8: Strongly coupled partitioned approach for the coupled system

3.2.3 FSI Problem Formulation

As said in the previous section we consider a computational domain, denoted by Ω, with an external boundary Γ. The domain includes the structural domain, Ω_s , and the fluid domain, Ω_f ; i.e., $\Omega = \Omega_f \cup \Omega_f$. The fluid-structure interface is defined by $\Gamma_s = \Omega_f \cap \Omega_f$ (Hou et al., 2012) .

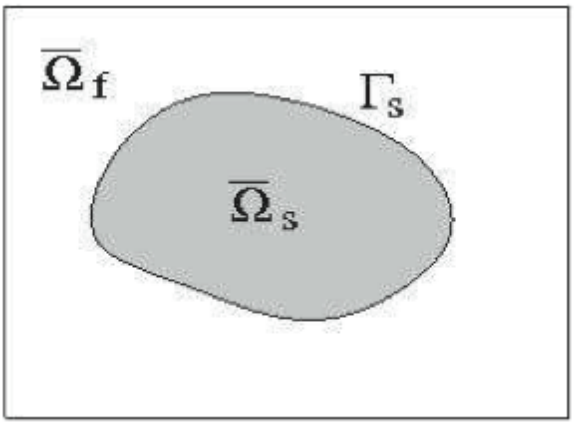

Figure 3.9: Schematic of the fluid and solid domains in a FSI problem

The equations of motion for the fluid and structure may be expressed in

the same index form, as a result of the D' Alembert 's principle:

$$\rho \dot{v}_i - \sigma_{ij,j} + f_i = 0 \tag{3.8}$$

where f_i is the body force, such as gravity. Specifically, in the structural domain, the equation is written as:

$$\rho^s \dot{v}^s_{ij,j} + f^s_i = 0 \quad in\ \Omega_s \tag{3.9}$$

where the superscript, s, denotes the quantity associated with the structure. Note that the velocity, v^s_i , is the material (or total) time derivative of the displacement field u^s_i , i.e., $v^s_i = \dot{u}^s_i$. Eq. (3.8) is usually given in the Lagrangian description. The first two terms in Eq. (3.8) are associated with inertia and internal stresses, respectively. For example, for linear elastic materials, the structural stress follows the linear Hooke 's law;

$$\sigma^s_{ij} = \lambda \delta_{ij} \epsilon_{ij} + 2G\epsilon_{ij} \tag{3.10}$$

where the structural stress is a function of the strains, and the Lame constants λ and G, which are defined by:

$$\epsilon_{ij} = \frac{1}{2}\left(u_{i,j} + u_{i,j}\right) \tag{3.11}$$

$$G = \frac{E}{2\left(1+\nu\right)} \tag{3.12}$$

$$\lambda = \frac{E\nu}{\left(1+\nu\right)\left(1-2\nu\right)} \tag{3.13}$$

where E and ν are the Young 's modulus and the Poisson 's ratio, respectively. In the fluid domain, the equation is given by:

$$p^f \dot{v}_i^f - \sigma_{ij,j}^f + f_i^f \quad in\ \Omega_f \tag{3.14}$$

which is usually represented by the Eulerian description. Thus, in the inertia term, one has

$$\dot{v}_i^f = \frac{dv_i^f}{dt} = \frac{\partial d_i^f}{\partial t} + v_j^f v_{i,j}^f \tag{3.15}$$

Assuming that the incompressible Newtonian fluid model is used here, the fluid stress is then given by:

$$\sigma_{ij}^f = -p\delta_{ij} + \tau_{ij} \tag{3.16}$$

where

$$\tau_{ij} = 2\mu\left(e_{ij} - \delta_{ij}e_{kk}/3\right) \qquad e_{ij} = \left(v_{j,i}^f + v_{i,j}^f\right) \tag{3.17}$$

Note that p is the static pressure which may be viewed as the necessary force to enforce the incompressibility condition, $v_{i,i}^f = 0$. To maintain the no-slip condition along the fluid-structure interface Γ_s, the following Dirichlet and Neumann conditions can be imposed,

$$v_i^s = v_i^f \quad on\ \Gamma_s \tag{3.18}$$

$$\sigma^s ijn_i = \sigma_{ij}^f n_i \quad on\ \Gamma_s \tag{3.19}$$

Eq. (3.19) is in fact the differentiation of the displacement condition that both fields share the same interface,

$$x_i^s = x_i^f \quad on\ \Gamma_s \tag{3.20}$$

or an interface profile that is smooth in time and space, some FSI methods consider Eq. (3.20) as the Dirichlet constraint, instead of Eq. (3.18) .

3.2.4 Different formulations to describe the state of a physic system

The Lagrangian formulation (Belytschko et al., 2000) is typically used to describe solid mechanics problems. The problem is described with a large number of particles having a certain mass, where the motion of a single particle is observed in space and time. The problem is exactly defined when the motion of every single particles is known. The Lagrangian formulation is very simple to use when the number of particles is small. The method become more complex to describe a large number of particles.

In the Eulerian formulation the problem is observed from a fixed point of the space that does not follow the motion of the single particle. In a interval of time Δt the particles can flow trough the observation point. Its motion is exactly defined when they passed trough that point. In the observation point the field variables are time dependent.

The main difference between Lagrangian and Eulerian formulation is that in the first one x, y and z are variable coordinates, where in the second method x, y and z are fixed coordinates of the defined field.

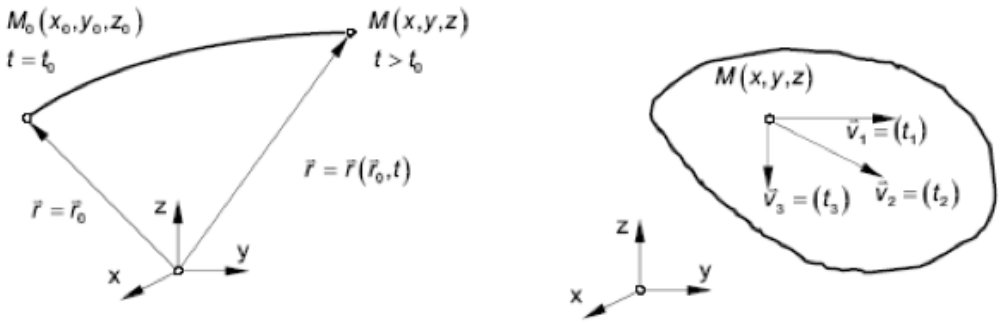

Figure 3.10: Lagrangian and Eulerian formulation

Governing equations for a dynamic finite element code

Typically, any dynamic finite element code needs to consider 3 physical laws. These laws are given in terms of spatial coordinates and are thus initially considered Eulerian, given in local form.

- Conservation of mass
- Conservation of linear and angular momenta
- Conservation of energy

$$\dot{\rho} + \rho v_{i,j} = 0 \tag{3.21}$$

$$\sigma_{ji,j} + \rho b_i = \rho \dot{v}_i \tag{3.22}$$

$$\sigma_{ij} = \sigma_{ji} \tag{3.23}$$

$$\rho E_{,t} = (\sigma_{ij} v_i)_{,j} + b_j v_j + (k_{ij}\theta_{,j})_{,i} + \rho s \tag{3.24}$$

E is definend by the equation (3.25), where $V^2 = v_i v_i$

$$E = W^{int} + \frac{V^2}{2} \tag{3.25}$$

The variables σ_{ij}, b, k_{ij}, θ, and s, are the stress tensor, body force, thermal conductivity tensor, temperature and specific source term respectively.

3.2.5 The Lagrangian formulation

In the *Lagrangian* frame the mesh moves with the deformation of the material. In the this formulation each element represents the same part of material from the beginning to the end of the analysis. The fluid domain can be described trough a model of material that skips the calculation of the deviatoric stress. Consequently, the quadrature points are also locked within the material, making storage of variables very convenient for history dependent materials. The treatment of boundary conditions is also very straightforward as they are always incident with the material domain. In addition, the stiffness and mass matrices determined by the Lagrangian formulation are always symmetric by the law of conservation of angular momentum, which can easily be utilized to reduce computational time. However, in systems with large element deformation, the Jacobian determinant of the deformation gradient tensor, equation (3.26), may attain negative values, resulting in negative mass and energy densities. It is also the issue of the stable time-step decreasing as a function of the smallest dimension of the deformed element. Since there is no convection of any properties in the Lagrangian formulation, the conservation of mass is given by stating that the mass of the elements are equal for subsequent time-steps. This implies that the density can be easily solved for, equation (3.28).

$$\rho\left(\mathbf{X},t\right), J\left(\mathbf{X},t\right) = \rho_0\left(\mathbf{X}\right) \tag{3.26}$$

$$J\left(\mathbf{X},t\right) = Det\left(F\right) \tag{3.27}$$

$$F = \begin{vmatrix} \dfrac{\partial x_1}{\partial \mathbf{X}_1} & \dfrac{\partial x_1}{\partial \mathbf{X}_2} \\ \dfrac{\partial x_2}{\partial \mathbf{X}_1} & \dfrac{\partial x_2}{\partial \mathbf{X}_2} \end{vmatrix}$$

which also simplifies the conservation of momentum and energy equations to:

$$\frac{\partial \sigma_{ij}}{\partial X_j} + pb_i = p\dot{v}_i \tag{3.28}$$

$$\rho \dot{E}^{int} = D_{ij}\sigma_{ij} - \frac{\partial k_{ij}\theta_{ij}}{X_i} \tag{3.29}$$

When compared to the Eulerian and ALE formulation, the algebra needed to solve a Lagrangian system is far less complex, as the constitutive equations are solved using material points.

The figure 3.11 shows the resolutive process of a simple problem with fluid using the *Lagrangian* formulation. It supposes that the force is applied only in the central node. The result of the applied force is the displacement of the central node in a *time step* calculation. If the force does not stop or changes, the node moves to a new position in the next *timestep* and the *mesh* deforms always more following the material flow.

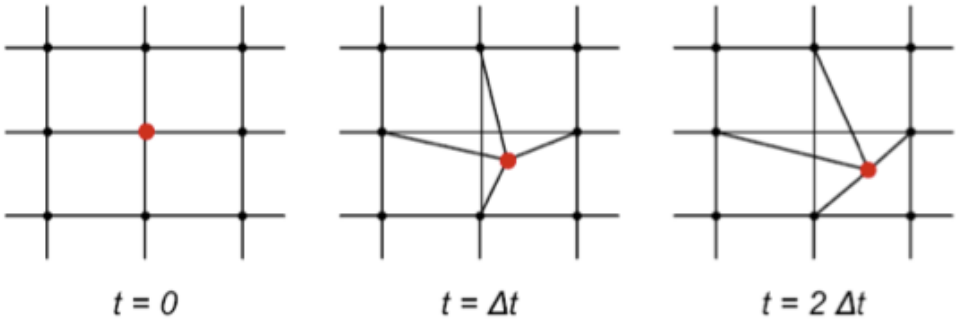

Figure 3.11: Solution of a problem according to Lagrangian formulation

3.2.6 The Eulerian formulation

The Eulerian finite element formulation assumes that the mesh is incident with spatial reference points that do not change as the material deforms. The material properties are thus updated by using a combination of convection and source terms within the elements. It is no issue with decreasing stable time-step or negative mass, as elements do not deform. However there are errors associated with the difference algorithms used to solve the convective terms that lead to smearing of discontinuities and attenuation, which effectively separates variables travelling at different frequencies. The fact that the nodes are also fixed while the material moves and deforms is problematic, as the solution variables need to be mapped into the material domain to get history variables locked to material points. Last but not least, moving boundaries also pose problems, as rigid Eulerian nodes can not conform to the moving bundaries. This makes the Eulerian formulation most appropriate in fluid mechanics where history variables usually are not needed for moving points.

The governing equations for the *Eulerian* formulation in terms of spatial points is equal to what is given in paragraph 3.2.4. However, in solid mechanics one is usually interested in obtaining derivatives locked to material points. The differential equation for a volume moving with the material flow becomes:

$$\frac{Df}{Dt} = f_{,[x]} + f_{,i}v_i \tag{3.30}$$

Where v_i is the material velocity. The governing differential equations from section 3.2.4 will take the form:

$$\rho_{,t[x]} + p_{,i}v_i + pv_{i,i} = 0 \tag{3.31}$$

$$\rho\left[v_{i,t_{[\chi]}} + v_{i,j}v_j\right] = \sigma_{ji,j} + pb_i \tag{3.32}$$

$$\rho\left(E_{,t_{[x]}} + E_{,i}v_i\right) = \left(\sigma_{ij}v_i\right)_{,j} + b_jv_j + \left(k_{ij}\theta_{,j}\right)_{,i} + ps \tag{3.33}$$

Applying the Eulerian formulation for fluids mechanics, the flux of fluid flows trough the fixed nodes of the *mesh* in the observing space. Although the *Eulerian mesh* apparently does not move and deform during the analysis, it actually change its position and shape only during the single *timestep*. The reason why stares in using the *Lagrangian* formulation in the single *timestep*. Considering the example of the previous section 3.11. Because of the load on the central node, the observed node change his position during the calculation in a *timestep* (the *mesh* deforms). Then this *timestep* the analysis stops and this two approximations are applied:

- *Mesh smoothing*: all the nodes of the *Eulerianmesh*, that have moved due to the load, are token back to the original position;

- *Advection*: the internal variables (stress, flux fields, velocity fields) for all nodes that have moved are recalculated (interpolated) so that they have the same spatial distribution before the *mesh smoothing*. So the *mesh smoothing* does not influence the internal variables distribution.

This procedure is repeated at each *timestep* of the analysis and gives an undeformed *mesh*.

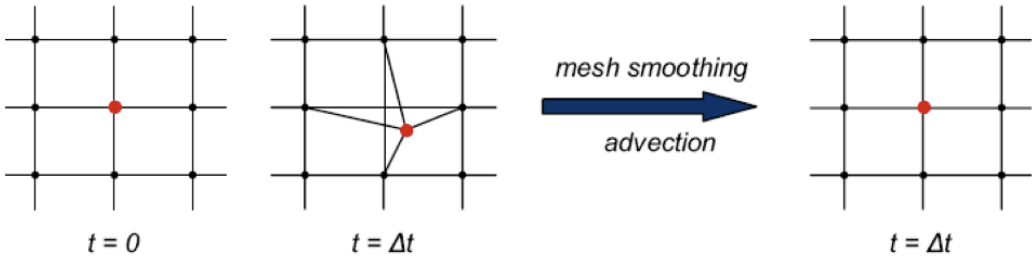

Figure 3.12: Solution of a problem according to Eulerian formulation

3.2.7 The Arbitrary Lagrangian Eulerian ALE formulation

The basic difference between Lagrangian, Eulerian and ALE element formulations, is how the mesh is constructed. In the Lagrangian formulation the mesh follows material points, while in the Eulerian formulation the mesh is locked to spatial reference points. The ALE formulation (Alia and Souli, 2005) takes the best from both methods, as it relieves the distortion in Lagrangian elements, and handles the moving boundaries unlike Eulerian methods. In this formulation the *mesh* moves and deforms partially because it follows the material (*Lagrangian* formulation), while at the same time the material can flow trough the it (*Eulerian* formulation). The ALE formulation is particularry useful when dealing with different materials, in particular when the coupling between a structure studied by Lagrangian frame and a fluid, typically studied by Eulerian frame, have to be solved. This problem arises when the moving mesh of the solid detach from the fixed Eulerian mesh of the fluid, due to the interaction.

The *ALE* settlement procedure is similar to the *Eulerians*. The only difference stares in the *mesh smoothing*. In the *Eulerian* formulation the nodes are put back to their original position, instead in the *ALE* formulation

the position of the moved nodes is calculated in accordance of the average distance of the contiguous nodes.

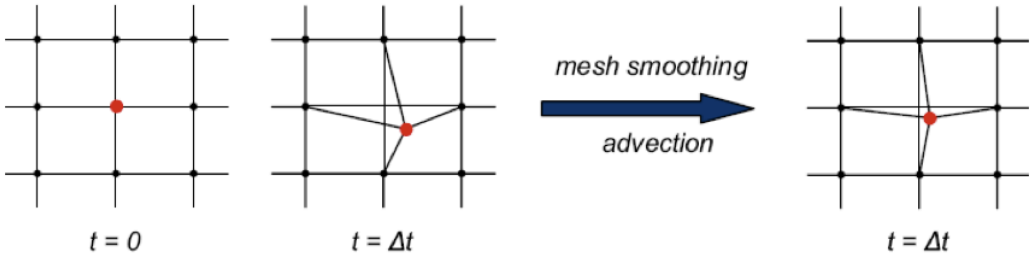

Figure 3.13: Solution of a problem according to ALE formulation

The *Eulerian* formulation presents numerical problems, such dissipation and dispersion, due to the energy flow of the mass trough the elements. Moreover, for the *Eulerian* mesh, a lot of elements could need the entire space where the material can be during the simulation process. The advantage of the *ALE* formulation is in fact the dejection of the dissipation and the dispersion, thanks to the possibility of reducing the domain trough operation of translation, rotation and deformation of the *mesh* in a controlled way. In fact it is clear that, minimizing the *mesh* dimension, the mass flows trough the elements reduces, giving minimal dispersion and dissipation, as well as the computational time. So, in theory, the *Eulerian* formulation can be seen like a particular case of the *ALE* formulation, by the fact that for each is done the *remesh* (or *mesh smoothing*) and the *advection*, with the differences written before.

Now we describe the *ALE* formulation trough the *Navier Stokes* equations (Alia and Souli, 2005). Since the Eulerian formulation is a particular case of the ALE finite element formulation, a general ALE point of view is described for compressible *Navier Stokes* equations. The ALE approach is based on the arbitrary movement of a reference domain, which will cor-

respond to the finite element mesh. This domain is introduced as a third domain additionally to the common material and spatial domains. These domains correspond to the Lagrangian and Eulerian domains, respectively. In ALE formulation, the air-blast problem is formulated in the coordinate of the reference domain. The arbitrary movement of this reference frame, accompanied by a mesh-moving algorithm, enables us to rather conveniently deal with moving boundaries, free surfaces and large deformations.

Let's consider a reference system coordinates and time dependent function f. Its total time derivative with respect to a reference coordinate can be described as:

$$\frac{df\left(\overrightarrow{X},t\right)}{dt}=\frac{\partial f\left(\overrightarrow{x},t\right)}{\partial t}+\left(\overrightarrow{v}-\overrightarrow{w}\right)\cdot\overrightarrow{grad}f\left(\overrightarrow{x},t\right) \tag{3.34}$$

where $\overrightarrow{X}$ is the Lagrangian coordinate, $\overrightarrow{x}$ is the ALE coordinate, $\overrightarrow{v}$ is the particle velocity and $\overrightarrow{w}$ is the velocity of the reference coordinate, which will represent the grid velocity for the numerical simulation, and the system of reference will be later the ALE grid. Let $\Omega^f \in R^3$ represent the domain occupied by the fluid particles, and let $\partial\Omega^f$ denote its boundary. The equations of mass, momentum and energy conservation for a Newtonian fluid in ALE formulation in the reference domain, are given by:

$$\frac{\partial\rho}{\partial t}+\rho\cdot div\left(\overrightarrow{v}\right)+\left(\overrightarrow{v}-\overrightarrow{w}\right)\cdot grad\left(\rho\right)=0 \tag{3.35}$$

$$\rho\frac{\partial\overrightarrow{v}}{\partial t}+\rho\left(\overrightarrow{v}-\overrightarrow{w}\right)\cdot\overrightarrow{\overrightarrow{grad}}\left(\overrightarrow{v}\right)=\overrightarrow{div}\left(\overrightarrow{\overrightarrow{\sigma}}\right)+\overrightarrow{f} \tag{3.36}$$

$$\rho\frac{\partial e}{\partial t}+\rho\left(\overrightarrow{v}-\overrightarrow{w}\right)\cdot\overrightarrow{grad}\left(e\right)=\overrightarrow{\overrightarrow{\sigma}}:\overrightarrow{\overrightarrow{grad}}\left(\overrightarrow{v}\right) \tag{3.37}$$

where ρ is the density and σ is the total *Cauchy* stress given by:

$$\left(\overline{\overline{\sigma}}\right) = -p\overline{\overline{Id}} + \mu\left(\overline{\overline{grad}}\left(\overrightarrow{v}\right) + \overline{\overline{grad}}\left(\overrightarrow{v}\right)^{T}\right) \tag{3.38}$$

where p is the pressure and μ is the dynamic viscosity. For compressible flow, (3.35) are completed by an equation of state that relies pressure to density and internal energy. In the energy equation (3.35), e is the internal energy by unit volume, the temperature is computed using an average heat capacity C_v:

$$\rho e = C_v \cdot T \tag{3.39}$$

If, in the previous equation $\overrightarrow{w} = 0$ is set, we shift from the *ALE* formulation to the *Eulerian* formulation, because it is imposed a null velocity to the reference coordinates. This assumption deletes the *smoothing* and the *mesh* nodes result as fixed.

Chapter 4

Examples of Numerical Simulation of explosions and interaction with Lagrangian Structures using LS-Dyna

4.1 Introduction

In this section we want to show how we can apply an explosive load in the software $LS-Dyna$. First of all we make a brief introduction to the software with the focus on the philosophy of the program and the organization of the input data. For the simulations we used two methods. First of all a pure *Lagrangian* method is implemented, where no explosive part is constructed, but it's used a particular *Load Function* native in $LS-Dyna$. This method is called $CONWEP$ (Pehrson and Bannister, 1997) and uses the theoretical *Brode* function (Harold and Brode, 1955) to apply the load on the structure. With this method we try to simulate the effects of an explosion of $0.1Kg$ of

TNT and a steel cantilever beam positioned in front of the explosive. We want to show how the stress in x direction propagates along the beam.

The other method is the multi material ALE that we have described theoretically in the previous chapter. With this method we can see the formation and the propagation in air of the blast wave. With the first simulation we only show the propagation of a cubic blast wave in a open domain with no interaction. In the second simulation we also show the interaction with the cantilever beam used in the *Lagrangian* exercise, so we can compare the propagation of the x- stress along the beam axis with the two different methods. With the $MMALE$ (multi material ALE) method, we have to construct both the model of the explosive and the one of the air as the continuum where the air blast can propagate. For the problem with no interaction, we first construct the cubic mesh of the free field of the air. Then we choose a cubic region and we assign the properties of the explosive. Thus we have at least two ***Parts**.

Finally when we model the interaction of the blast wave with a Lagrangian structure, we have to set a FSI (Fluid Structure Interaction) problem. In addition to the parts of the air and the explosive, we also have to model the parts of one or more Lagrangian structures, were the interaction takes part.These parts have to intersect the nodes of the ALE parts of air, otherwise we would have no interaction. In Fluid Structure Interaction problems we have to define the $Master$ and the $Slave$ parts of the problem. In general the $Master$ is an ALE, or Eulerian parts, which is the the part that imposes forces or pressure in the interaction, instead the $Slaves$ parts are Lagrangian, and are the part that are invested by the interaction.

4.2 Introduction to the software $LS-DYNA$

$LS-DYNA$ is a general purpose finite element code whose goal is to analyze the large deformation statics and dynamics response of structures subjected to various loads, including coupling with fluids. It works trough an explicit dynamics solver and needs a pre and post-processing software. In particular the pre-processing is the phase where the geometry, the material, the mesh and the load are defined, while with the term post-processing we denote the phase where we elaborate the results of the simulation . In our case we use the native software $LS-PREPOST$ by *Livermore Software Technology Corporation* also note as $LSTC$. The pre-processing phase ends with the creation of a *Keyword* file, which is processed by $LS-DYNA$

4.2.1 Input file preparation: the Keyword

A data block , that is the file generated by $LS-PREPOST$, begins with a keyword followed by the data pertaining to that section. When we read the keyword file and we find a word (i.e. ***MAT**), we know that the following data represent the description of a particular section (in case of *MAT, we refer to the material). The next keyword encountered during the reading of the block data defines the end of the block and the beginning of a new block. A keyword have to be left justified with the " $*$ " contained in column one. A dollar sign in column one precedes a comment and causes the input line to be ignored. Data blocks are not a requirement for $LS-DYNA$ but they can be used to group nodes and elements for our convenience. In order to solve any kind of problem, the first step is to create geometry and a mesh and define the node. As an example, we consider a mesh consisting of only one brick element and 8 node points. Also, we use default values

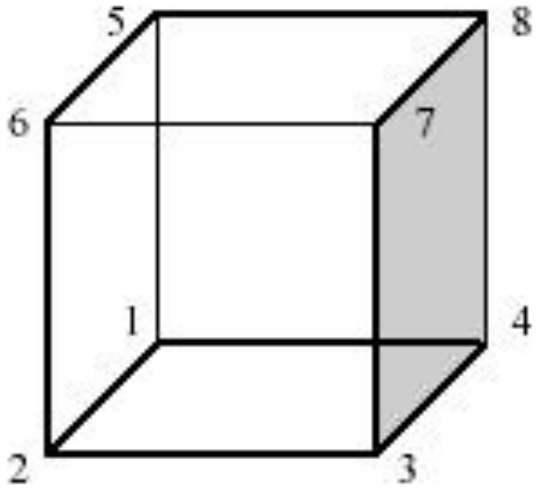

Figure 4.1: Eight node solid element

for many of the parameters in the input file . The first line of the input file have to begin with ***KEYWORD**. This identifies the file as containing the keyword format. The first input block is used to define solution control and output parameters. The ***CONTROL TERMINATION** keyword have to be used to specify the problem termination time. Additionally, one of the many output options should be used to control the printing interval of results (e.g., ***DATABASE BINARY D3PLOT**). To obtain a time history output we have to set also ***DATABASE BYNARY THDT** and set the end time that we want. The second input block is used to define the model geometry, mesh, and material parameters. The following description and map may help to understand the data structure in this block. The keyword *PART represents a series of elements and nodes with the same characteristics, such as the material, the equation of state (in the case of fluids) and the element formulation (Lagrangian, Eulerian or ALE). We consider 1 part, the cubic block, and use the *PART keyword to begin the definition of the

finite element model. The keyword *PART contains data that point to other attributes of this part, e.g., material properties. Keywords for these other attributes, in turn, point elsewhere to additional attribute definitions. The organization of the keyword input looks like this:

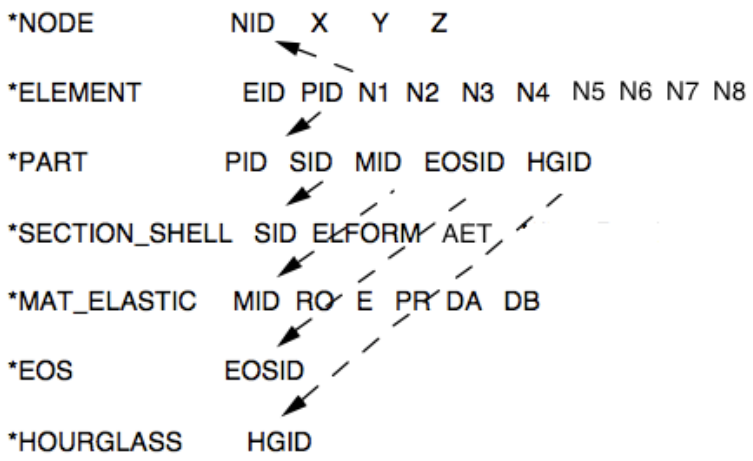

Figure 4.2: Keyword philosophy

The figure shows the general philosophy of the input organization and how various entities are related to each other. In this figure the data included for the keyword, ***ELEMENT**, is the element identifier, EID, the part identifier, PID, and the nodal point identifier, the NID, defining the element connectivity: N1 N2 N3 N4 N5 N6 N7 and N8. The nodal coordinates are defined in the ***NODE** section where each NID should be defined just once. A part identifier ***PART** keyword has unique part identifier, PID, a section identifier, SID, where the section element formulation is specified and so on. The material constants are defined in the ***MAT** section where constitutive data are defined for all elements type including solids, shells, beam and other else. Equation of state, which is used only with certain ***MAT** mate-

rials for solid elements, is defined in the ***EOS** section. Since many elements in $LS-DYNA$ use uniformly reduced numerical integration, zero energy deformation modes may be developed. These modes are controlled numerically by either an artificial stiffness or viscosity which resists the formation of these undesirable modes. The hourglass control can optionally be specified by using the input in the ***HOURGLASS** section.

4.3 Simulation of the interaction of a cantilever beam with an explosion using the CONWEP pure Lagrangian method

One of the very useful features in $LS-DYNA$ is the ability to simulate the detonation of an explosive and the loading caused by it.

In this problem we want to simulate the interaction of a cantilever beam, with an spherical explosion. In order to do that, we use the $CONWEP$ function to directly apply the pressure load due to the explosion on the surface of impact. The beam has a length of $2m$ and a square cross section of $10cm$ for each side. The charge is positioned at a distance of $6m$ from the surface of impact. The weight of the charge is $0.1\ Kg$ and the explosive used is TNT. After the simulation we want to see the wave propagation along the length of the beam, in the x-direction. To validate the experiment we also perform a convergence analysis with different mesh density, because we want to see how the density mesh influence the accuracy of the results. For better see the wave propagation along the beam axis, we analyze the problem by setting the $Poisson\ ratio\ \nu = 0$.

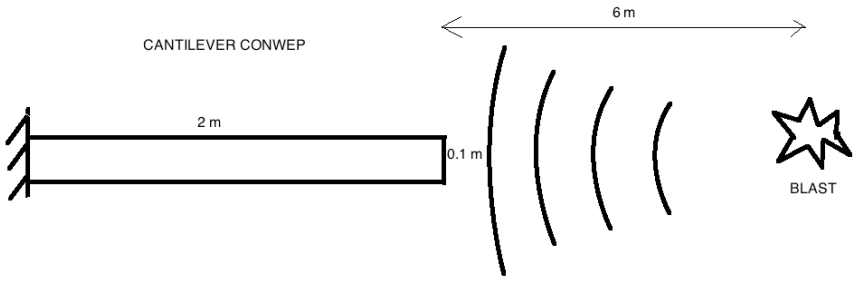

Figure 4.3: Description of the CONWEP cantilever problem

4.3.1 The CONWEP function

$LS-DYNA$, trough the CONWEP function, allows users to simulate blasts using the $Kingery$ and $Bulmash$ function (Kingery and Bulmash, 1984) that provides pressure loads due to explosives in conventional weapons. $CONWEP$ is a well known "tool" in structural analysis when looking at blast loading. To avoid computational cost and complexity by doing CFD-analysis, one can simplify by using ConWep.

The $CONWEP$ algorithm takes in account the angle of incidence by combining the reflected pressure (normal-incidence) value and the incident pressure (side-on incidence) value. Accordingly, The $LS-DYNA$ blast-loading model is modified so that it can calculate the angle of incidence and then take the sum.

$$Pressure\ Load = P_r \cos^2\theta + P_s(1 + \cos^2\theta - 2\cos\theta) \tag{4.1}$$

where P_r is the reflected pressure and P_s is the incident pressure.

When $cos\theta$ is negative (i.e., the surface is not facing the point of explosion), then $iressureLoad$ equal the $incidentPressure$, but the arrival time and the incident pressure are not adjusted in any way to account for shadowing by the intervening structure.

CONWEP is implemented in LS-DYNA as $*$**LOADBLAST**. With the *Keyword* **Load Blast** we define an airblast function for the application of pressure loads due to explosives in conventional weapons. The implementation is based on a report by $Randers - Pehrson$ and *Bannister* (Pehrson and Bannister, 1997) where it is mentioned that this model is adequate for use in engineering studies of vehicle responses due to the blast from land mines.

With this method we do not explicitly simulate the progress of the shock wave in air, but we just apply a specific pressure on a surface of the Lagrangian solid. This method is computationally less expensive than the ALE method at the cost of accuracy: $CONWEP$ is unable to account for confinement (focusing of the blast due to geometry) or shadowing (when an object is blocking a surface from direct loading).

The input data required by the $CONWEP$ model are:

- weight: equivalent mass of TNT
- x_0 y_0 z_0: coordinates of the point of explosion, in problem length units
- t_0: delay time between when the $DYNA$ problem starts and the istant of the explosion, in problem time unit. It can be negative.
- nunit: units switch: we use in this problem Kg ,m ,Pa, μs
- isurf: type of blast:
  - 1 : surface blast
  - 2 : air blast

In addition, the $LS-DYNA$ model requires a list of the surface segments that will experience the blast loading. This is done in the same manner as

with the *Brode* model, except that the load curve number is -2 instead of -1.

4.3.2 Numerical Model

The model is constituted by a single part that represents the cantilever beam. The beam have have a length of $2m$ in x direction, and a square cross section of 0.01 m^2. So the dimension in y and z direction is $0.1m$.

Material Properties

Once modelled the geometry we set the material properties. First of all we have to go to the ***MAT** tab in the third page of the program choose one of the proposed materials and edit it. We choose the material ***MAT ELASTIC** with the following properties:

- Density: 7810 Kg/m^3
- Young Modulus (E) : 2 x 10^{11} Pa
- Possion Ratio (ν) : 0.3

We have to set a number ID and a name for the material. After doing this, we have to tell the program which element formulation has to be used for the ***PART** of the beam. We choose in the ***SECTION SOLID** the element formulation "1" that corresponds to the *Lagrangian* formulation. Now to assign the material properties and the element definitions to the model we go to the ***PART** tab and we set SECID an MID as 1, because 1 is the ID of the element formulation and the material properties.

Loads and Boundary conditions

In our case the beam is clamped in one of the extremity. Thus we have to set the clamps in all the nodes at $x = 0$. To do this we first have to set the list of the nodes in the tab ***SetD** selecting the nodes directly from the model (***SET NODE**). Then in the tab ***SPC** we choose the degrees of freedom that we want to block.

We are now ready to set the blast load on the opposite surface of the beam. First of all we set the surface where the pressure is applied in the ***SetD** tab. This time we select ***SET SEGMENT** and from the model we peak all the element of the surface. Then we define the load in the ***LOAD BLAST** tab. As described earlier we have to set all the parametres as follows:

- WGT= $= 0.1\ Kg$ (weight of the charge)
- x_0=0 y_0=0 z_0=0 (position of the charge)
- TBO=0.0001s (time-zero of the explosion)
- IUNIT=2 (Kg ,m, s, Pa)
- ISURF=2 (airblast)

Blast requires us to define at least two load curves even though they may remain unreferenced. We go in the ***DEFINE** tab to edit the curves. We insert the default abscissa, $A1$ and ordinate $B1$ values which correspond to time and load respectively and the next set of values as 1 and 1. Now to apply the load we select again the ***LOAD** tab and select **SEGMENT SET** from the list. For blast we are required to enter the *Load Curve ID LCID* as -2.

4.3.3 Analysis and Results

As written before, we perform this analysis considering three different mesh densities and with two different configuration of material properties.

We require the program to give us a photography of the model every 0.001 seconds, with an end termination of 0.3 seconds. So we can clearly see the propagation of the x stresses along the beam. We also ask the program to give us the time history of some elements to see exactly some characteristic values of the problem, such as the time arrival t_a of the wave and the intensity of the $x - stresses$.

First mesh configuration

in the first mesh configuration the domain has been discretized by:

- 60 elements in x direction
- 3 elements in y direction
- 3 elements in z direction

So the single element is hexaedral with eight node per element and is exactly cubic. Then we have 540 elements and 976 nodes (figure 4.4) .

Results

The program gives us a photography of the model every 0.001 seconds, with an end termination of 0.3 seconds. Thus we can see clearly the propagation of the x stresses along the beam.

As we can see, the contours of the wave are not well defined, due to the coarse mesh.

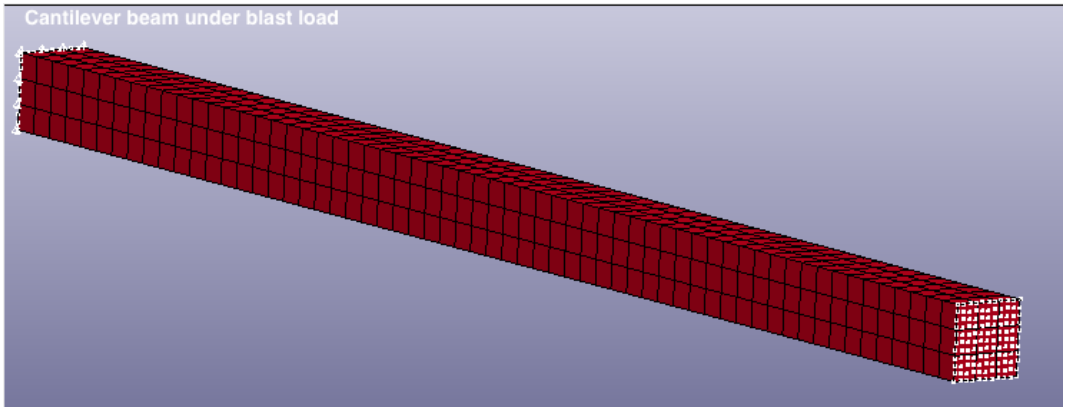

Figure 4.4: first mesh configuration

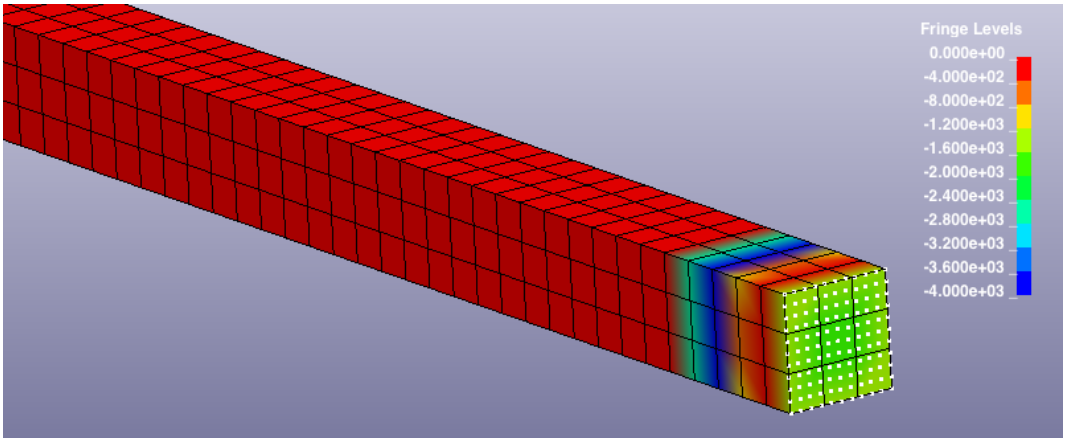

Figure 4.5: propagation of x-stress 1

Second mesh configuration

in the second mesh configuration the domain has been discretized by:

- 200 elements in x direction
- 10 elements in y direction
- 10 elements in z direction

So the single element is hexaedral with eight node per element and is exactly cubic. Overall we have 2000 elements and 88641 nodes.

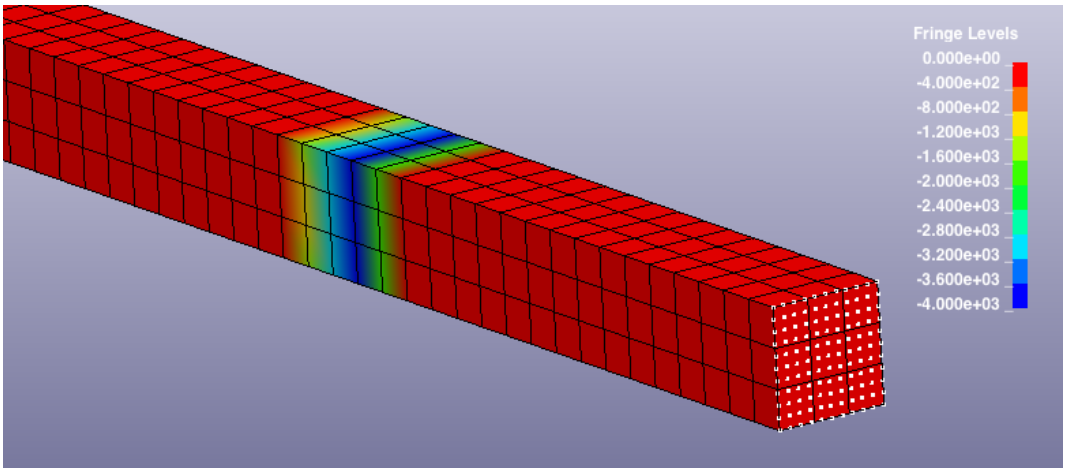

Figure 4.6: propagation of x-stress 2

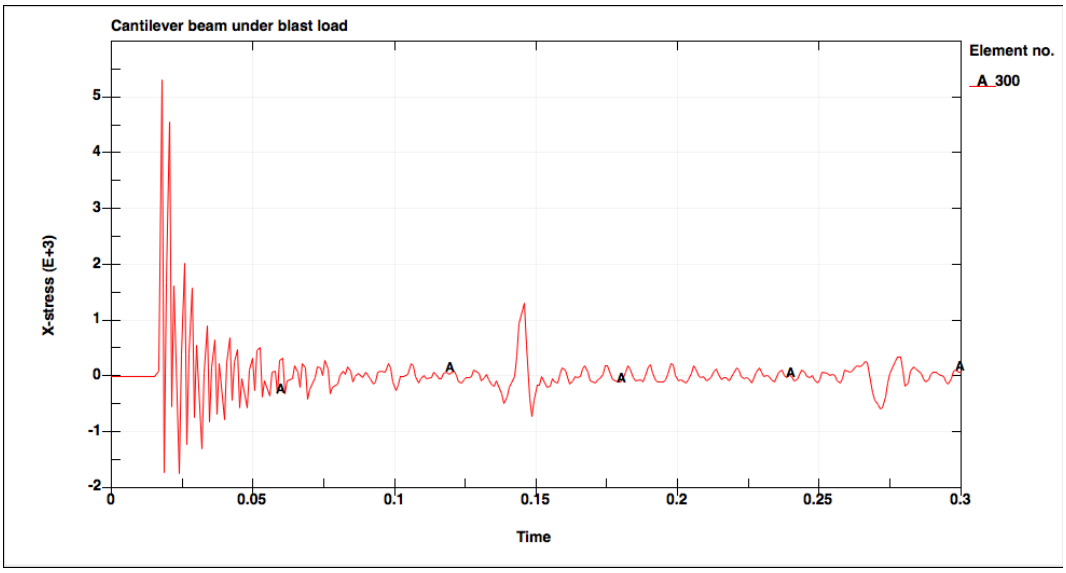

Figure 4.7: history of the x-stress in the central element of the impact surface

Results

The program gives us a photography of the model every 0.001 seconds, with an end termination of 0.3 seconds. So we can see clearly the propagation of the x stresses along the beam.

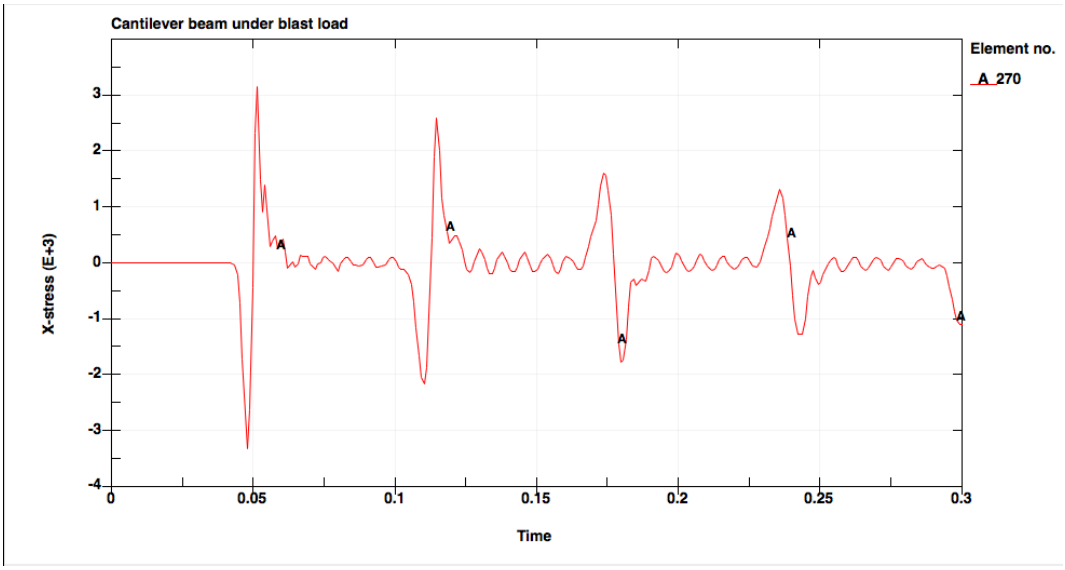

Figure 4.8: history of the x-stress in the central element of the beam

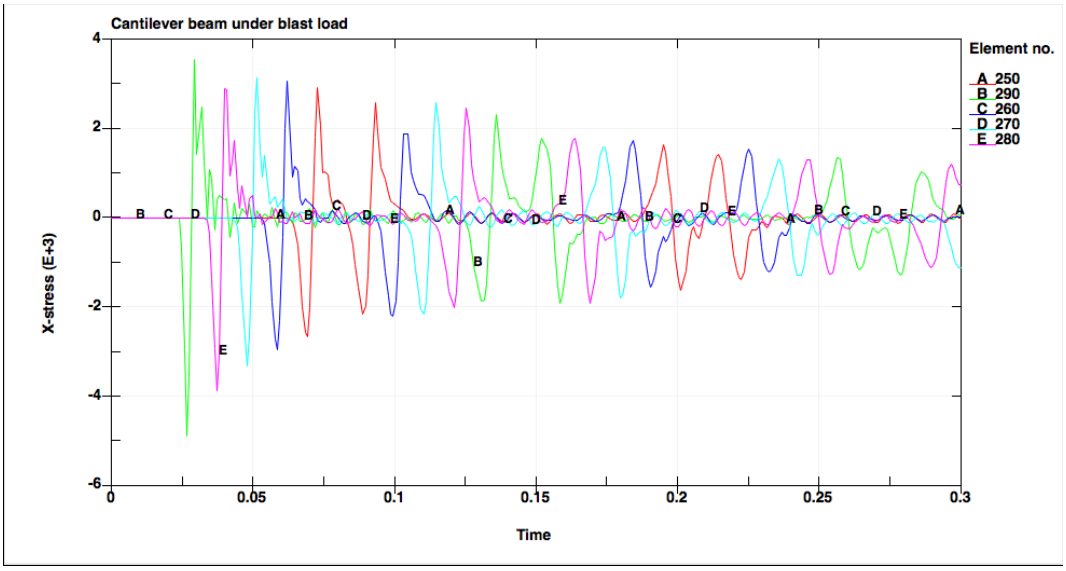

Figure 4.9: history of the x-stress in the central elements along the beam

As we can see, the contours of the wave are better defined with respect to the first mesh configuration. Also the intensity of the stresses are different.

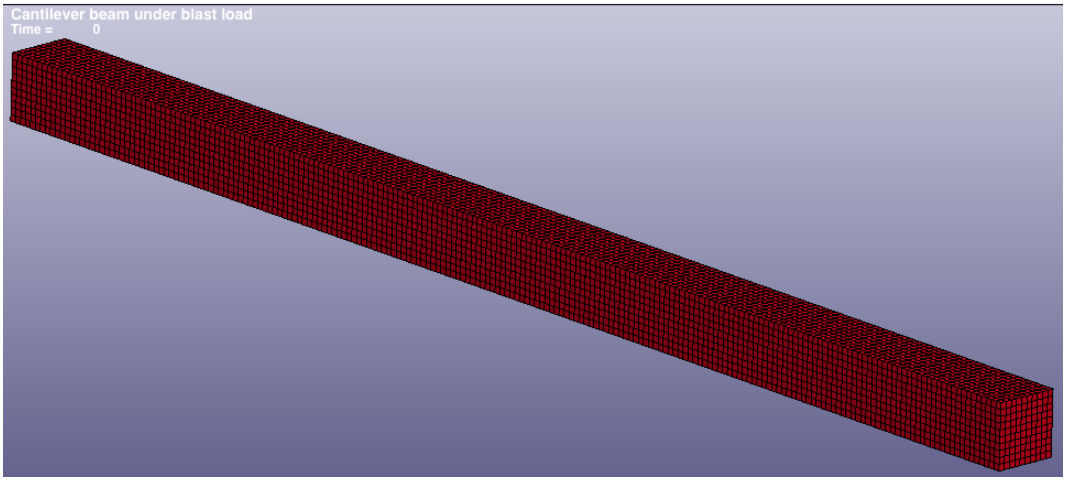

Figure 4.10: second mesh configuration

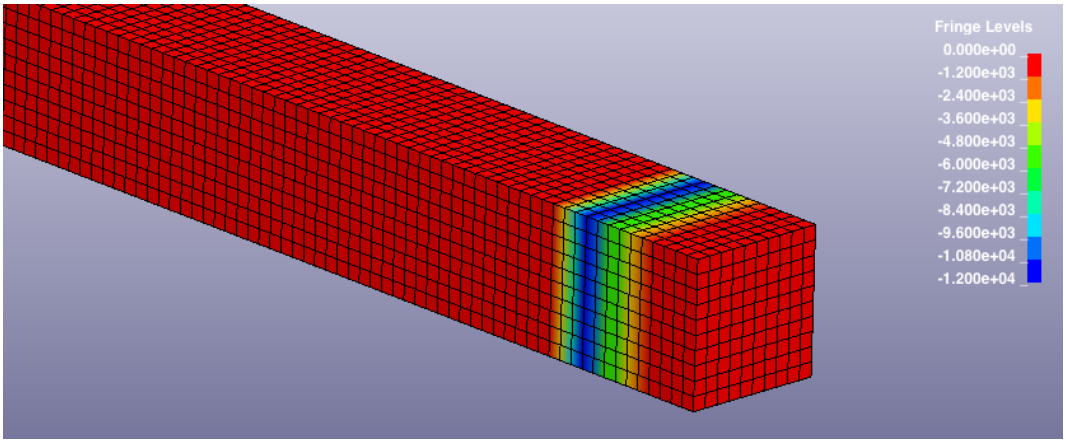

Figure 4.11: propagation of x-stress 1

Third mesh configuration

in the third mesh configuration the domain has been discretized by:

- 600 elements in x direction
- 30 elements in y direction
- 30 elements in z direction

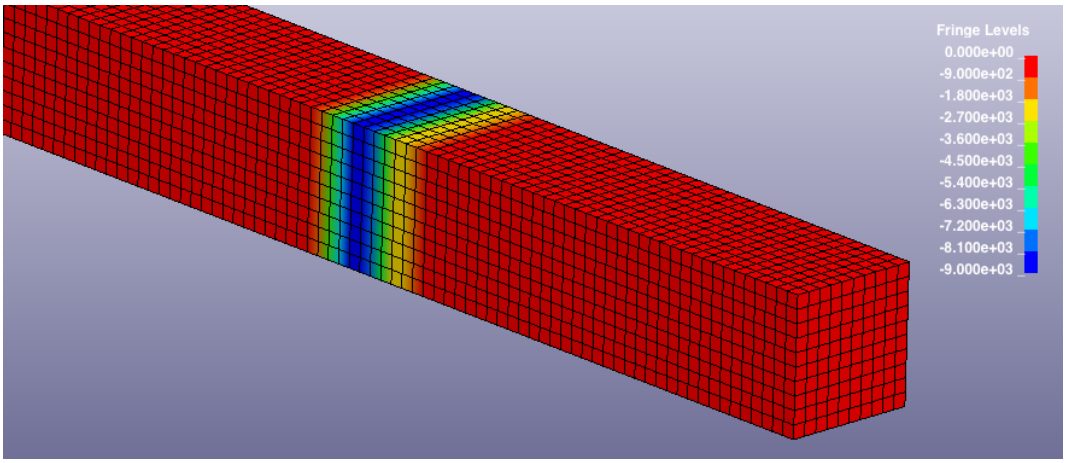

Figure 4.12: propagation of x-stress 2

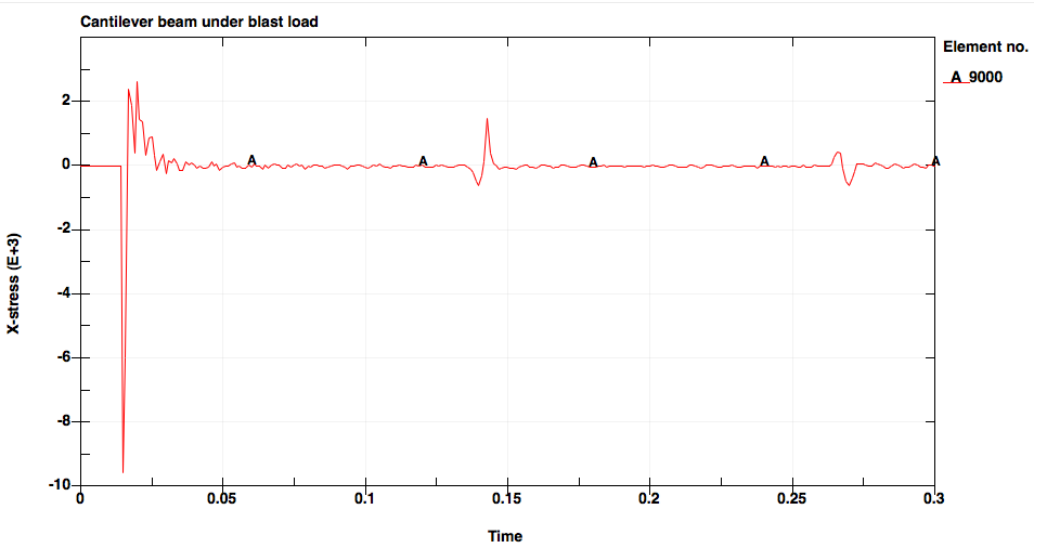

Figure 4.13: history of the x-stress in the central element of the impact surface

So the single element is hexaedral with eight node per element and is exactly cubic. Overall we have 540000 elements and 577561 nodes.

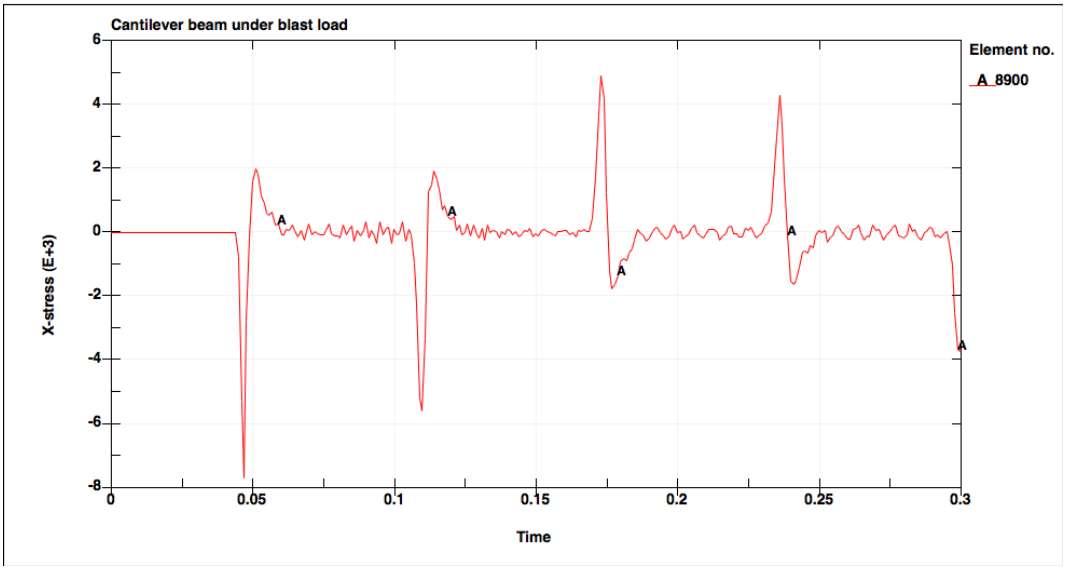

Figure 4.14: history of the x-stress in the central element of the beam

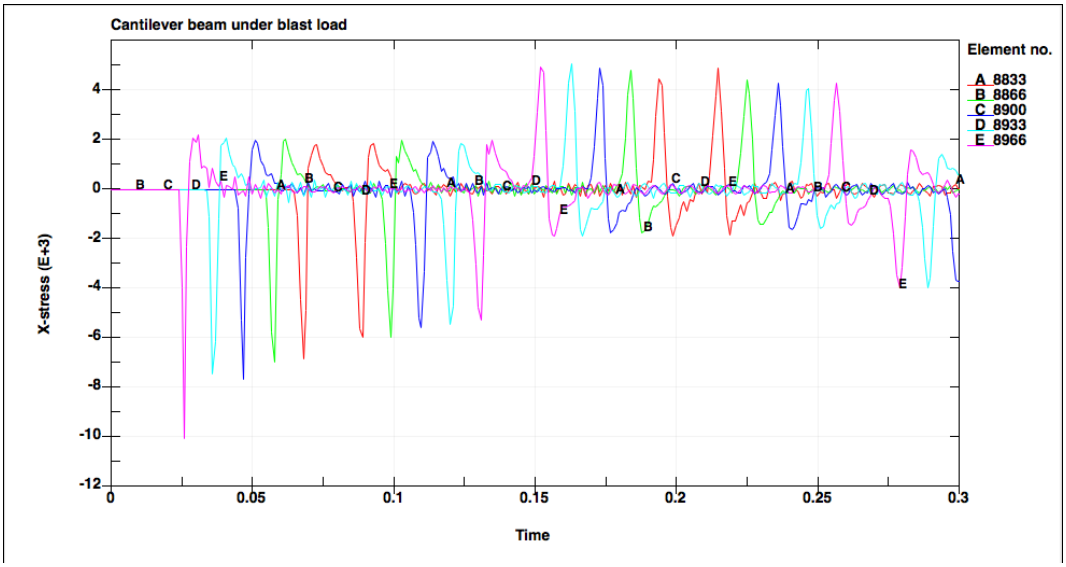

Figure 4.15: history of the x-stress in the central elements along the beam

Results

The program gives us a photography of the model every 0.001 seconds, with an end termination of 0.3 seconds. So we can see clearly the propagation of

the x stresses along the beam.

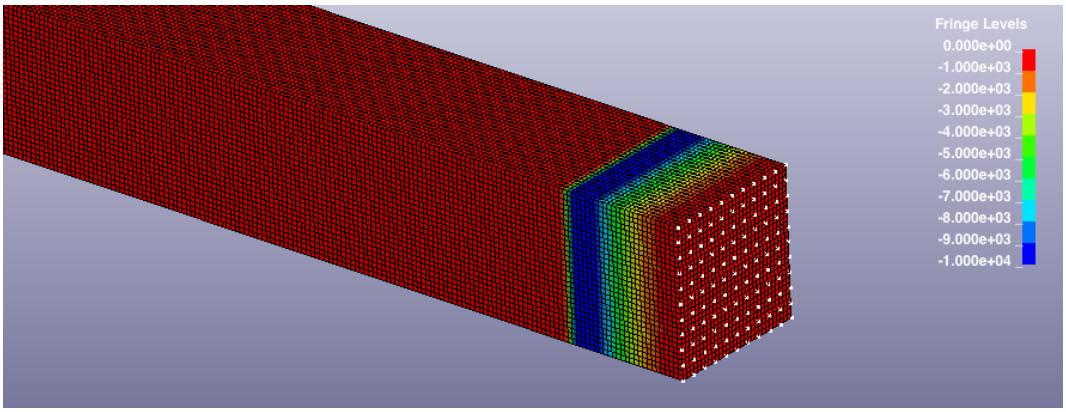

Figure 4.16: propagation of x-stress 1

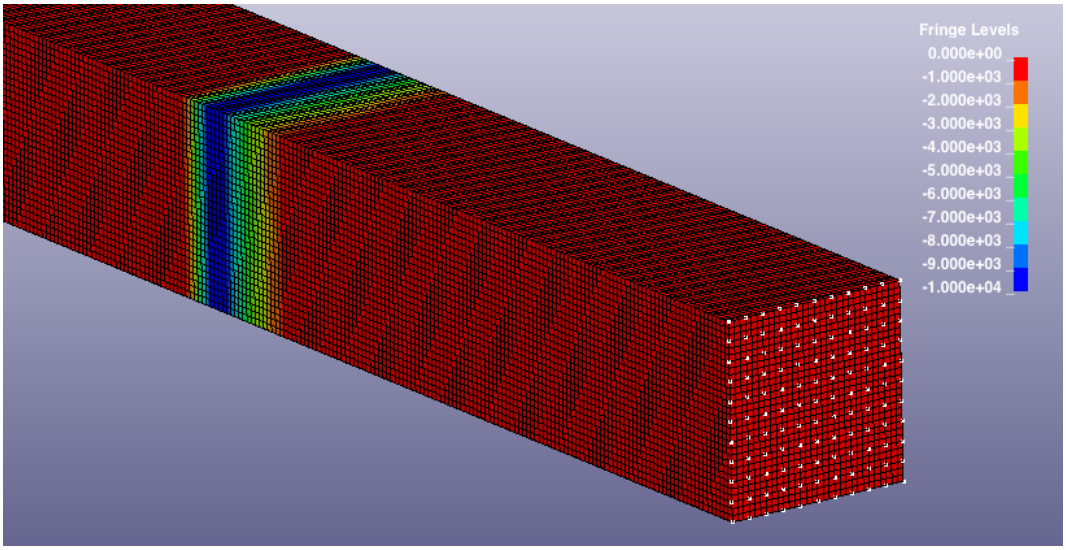

Figure 4.17: propagation of x-stress 2

As we can see, the contours of the wave are very well defined, due to a very fine mesh. Instead the results are not very different between the second and the third mesh.

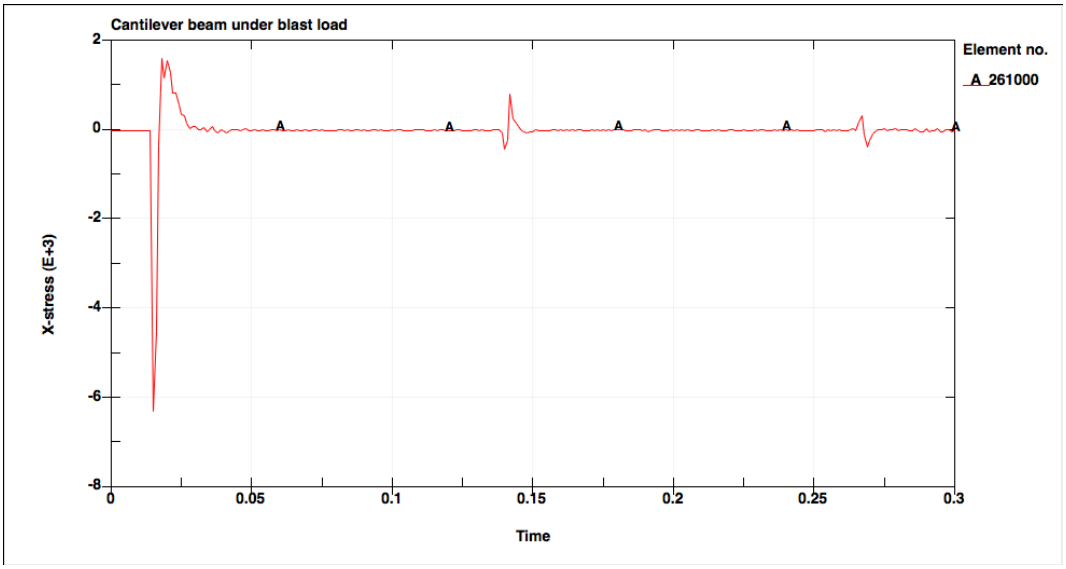

Figure 4.18: history of the x-stress in the central element of the impact surface

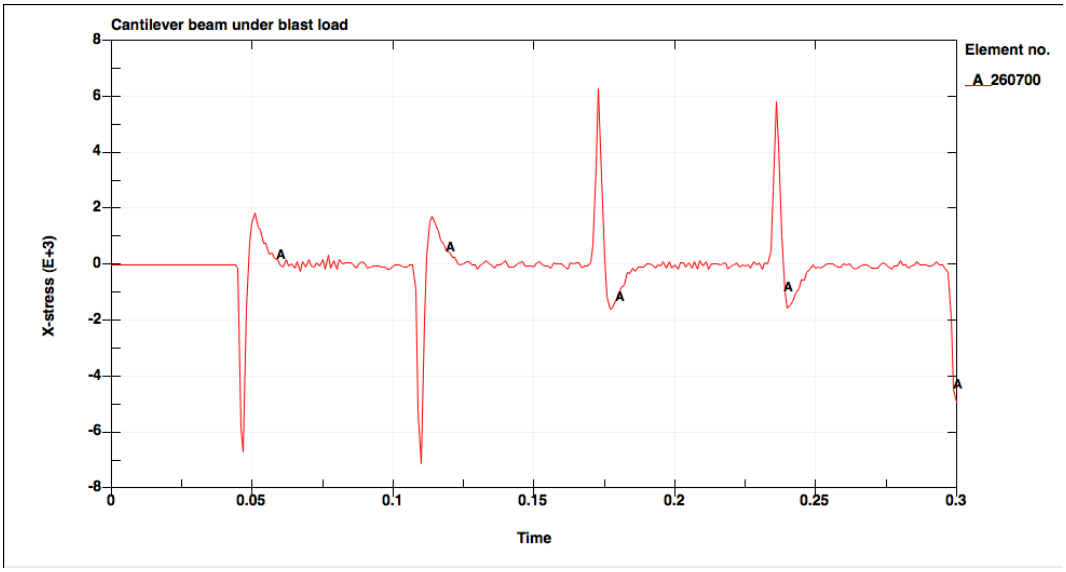

Figure 4.19: history of the x-stress in the central element of the beam

Discussion

From the results we can clearly see that the density of the mesh is very important for the accuracy of the results. It is evident that in the first mesh

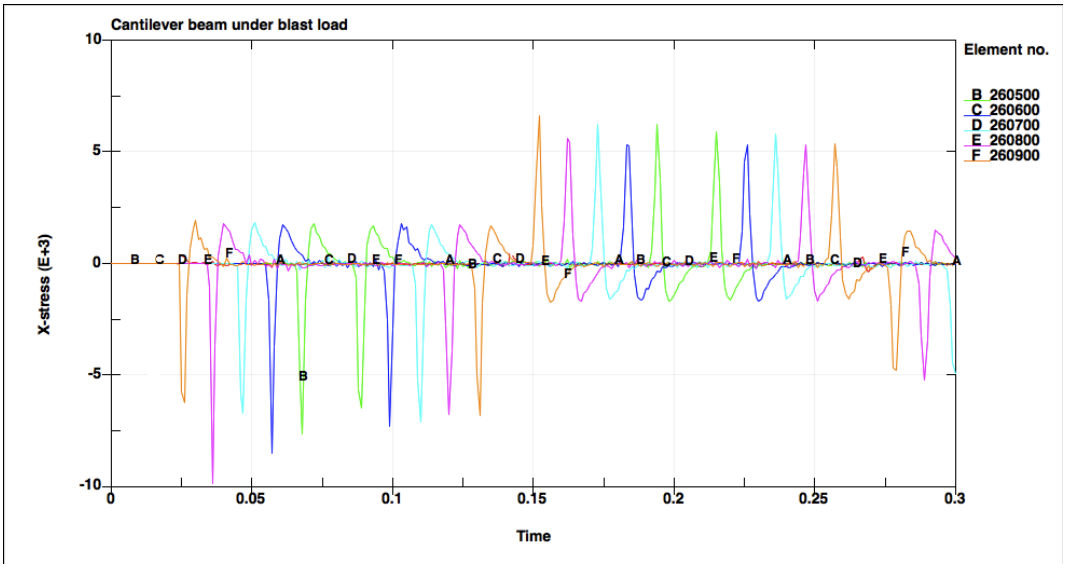

Figure 4.20: history of the x-stress in the central elements along the beam

time = 0.11 sec	**x-stress**
first mesh	-2.16 KPa
second mesh	-5.59 Kpa
third mesh	-7.11 KPa

Table 4.1: peak of negative stress in the three meshes

configuration the results are very influenced by the very coarse mesh.

In this tables we show the values of the x-stress in the three different mesh configuration at the same time. In the first one we want to evidence a peak of the negative value and in the second one a peak of the positive value.

The wave intensity along the beam decreases evidently, something that should not happen. In fact in the second and third mesh configuration this phenomenon does not occurs. We can also say that the results with the second and the third mesh are quite similar, so is not necessary to increase the density of the mesh more than the second one. The comparison of the

time = 0.17 sec	**x-stress**
first mesh	1.61 KPa
second mesh	4.92 KPa
third mesh	6.28 KPa

Table 4.2: peak of positive stress in the three meshes

x-stress history of the three mesh are shown in the figure 4.21.

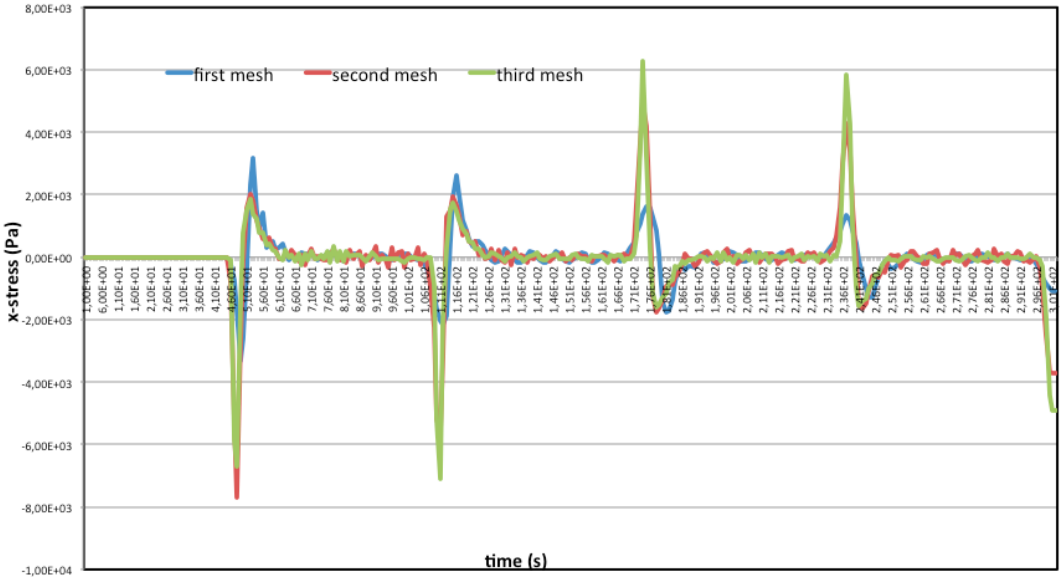

Figure 4.21: comparison of the x-stress history with the different mesh densities

4.4 Multi Material ALE Simulation of an explosion of cubical charge of 1.67Kg TNT in a cubic box full of air

In this simulation we want to represent the propagation of the shock-wave due to the explosion of 1.67 Kg of TNT in a free cubic field. The cubic shape explosive is placed in one of the corner of the cubic free field. The length is 10 cm long to represent a charge of 1.67 Kg of TNT. The field of the air is represented with a box of 100 cm per side. With this simulation we want to see how a shock wave propagate in a free field. To avoid the reflection of the wave in the face were the explosive is modelled, we have to add a specific non-reflecting boundary condition. Both the air and the explosive are modelled with the ALE formulation. After the simulation we compare the results of the simulation with the analytical solution available in the literature. The quantity that we want to focus are the progress of the peak of overpressure in function of the scaled distance and the velocity of the shock front. In this and in all the other problems developed with the ALE formulation we choose a set of consistent units that are: g,cm,μs and $Mbar$.

4.4.1 Materials and Equation of State

Material Model for Air

Air is modelled with 8 node finite elements using the hydrodynamic material model $*MAT\ NULL$. For solids elements equation of state can be called trough this material model to avoid deviatoric stress calculation. The parameter that we have to set for this material model is only the density: ρ = 0.001255 g/cm^3. The model requires also an equation of state, pressure

cut-off and viscosity coefficient to be defined. The viscosity and pressure cut-off are set to zero, because pressure cannot be negative and the viscosity forces are negligible.

EOS polynomial equation of state

The ideal gas law (gamma law) is used as the equation of state for air. This polytropic equation of state is given by considering the general linear polynomial equation of state (Alia and Souli, 2005)

$$p = C_0 + C_1\mu + C_2\mu^2 + C_3\mu^3 + E\left(C_4 + C_5\mu + C_6\mu^2\right) \tag{4.2}$$

For ideal gas, this equation can be reduced using appropriate coefficents:

- C_0=C_1=C_2=C_3=C_6= 0
- $C_4 = C_5$=γ -1

by setting μ as:

$$\mu = \frac{\rho}{\rho_0} - 1 \tag{4.3}$$

we obtain:

$$p = (\gamma - 1)\frac{\rho}{\rho_0}E \tag{4.4}$$

where ρ_0 and ρ are the initial and current density of air, E is the specific internal energy (with the units of pressure) and γ is the polytropic ratio of specific heats. For the diatomic molecules, including air, this adiabatic expansion coefficient is $\gamma = 1.4$. Here the numerical values used for air are:

- $\gamma = 1.4$
- $E_0 = 2.5e^{-6}\ Mbar$

- $\rho_0 = 1.293e^{-3}\ g/cm^3$

Note that the equation (4.4) gives at time $t = 0$, an initial pressure $P_0 = 1bar$, for $\gamma = 1.4$ and $E_0 = 2.5bar$.

The polytropic form Eq (4.4) is related to the ideal gas law via:

$$pv = RT \tag{4.5}$$

where R is the gas constant and T is absolute temperature.

To be thermodynamically consistent, the air material have to be initialized with a non-zero internal energy so that its initial pressure is non-zero. The air can leak out of the mesh if appropriate boundary conditions are not imposed at the external boundary, to avoid initial air leakage, a 1 bar pressure boundary condition is assumed.

Material Model for TNT

For the material model of the explosive, in our case TNT, we have chosen the $HIGH\ EXPLOSIVE\ BURN$ material model with 8th node finite elements. The explosive material model requires density, detonation velocity V_d, the Chapman Jouguet pressure P_{cj}, and a equation of state for pressure. Throughout this section, various subscripts will be used. These are s for an isentrope, h for a Hugoniot, CJ for the CJ state, and 0 for the initial state. Chapman Jouguet pressure generally refers to the detonation pressure, which is somewhat lower than the initial shock front pressure . The assumption of Chapman and Jouguet (Coleburn, 1964) (equation (4.2)) states (figure 4.22) that for a plane detonation wave to be propagated steadily, the Rayleigh line, which is derived from the mass and momentum conservation, have to be tangent at the CJ point to the Hugoniot curve of the gaseous products that is derived from the energy conservation.

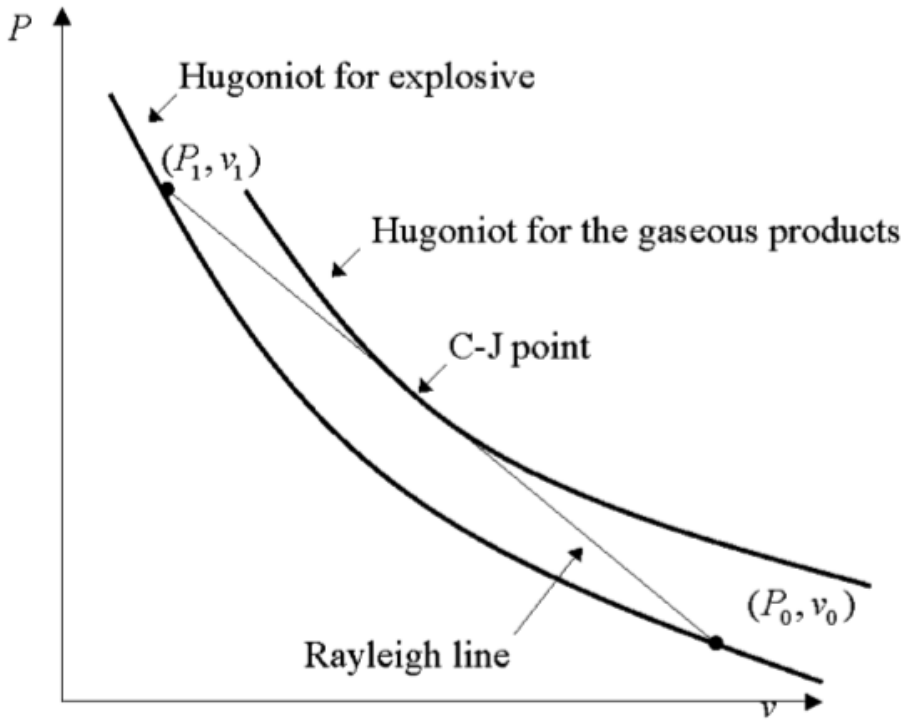

Figure 4.22: Hugoniot curve and Rayleigh line

In a steady state process, these are assumed to be produced with an infinite reaction rate in order to attain the chemical equilibrium. As shown in figure 4.22, the shock front, which advances through the explosive with a detonation velocity Vd compresses the explosive particles from a status point (P_0, v_0) to another one (P_1, v_1), defined by the intersection of the Rayleigh line and the Hugoniot curve for the explosive. After the completion of the detonation process, the interaction process takes place. A produced gas with high pressure and temperature expands outward by generating a pressure wave. Due to the high pressure, the gaseous products can be assumed to be inviscid, and thus viscous forces are ignored. In air explosion, the pressure wave moves with the gas air interface. The fluid layer at the pressure wave is a mixture of gas and air, which makes it more complex from a simulation

point of view.

EOS John Wilkins Lee equation of state

An essential part of the numerical models, used to simulate high explosives and their detonating products, is the equation of state (EOS) relating energy, pressure and density. Both theoretical and empirical approaches have been employed to describe explosive equations of state (Thiel et al., 1983). Various types of EOS describe the state of detonation products. Jones Wilkins Lee (JWL) EOS is widely used because of its simplicity and due to the fact that most high explosives are well modelled by this equation of state. The definition of the JWL equation of state starts from its isentropic form, namely:

$$p_s = A^{(-R_1 V)} + B^{(-R_2 V)} + CV^{\omega+1} \tag{4.6}$$

where p is the pressure and the subscript s denotes reference to isentropic compression or expansion. A, B, $R1$, $R2$ and ω are user defined constants which the performance values are:

- A=5.409405 $Mbar$
- B=0.093726 $Mbar$
- R_1=4.5
- R_2=1.1
- ω = 0.35
- E=0.08 $Mbar$
- V_0=0.8

The imput parameters for this equation are given by Dobratz (Dobratz, 1981) for a large variety of high explosive materials.

For reacted products, R_1 is chosen to be about four times R_2, so that the first term dominates at high pressures, the second term is significant at intermediate pressures, and the third term prevails at low pressures.

After several calculation reported in (Alia and Souli, 2005) the JWL equation of state becomes:

$$P_{JWL}(V,E) = A\left(1-\frac{\omega}{R_1V}\right)e^{-R_1V} + B\left(1-\frac{\omega}{R_2V}\right)e^{-R_2V} + \frac{\omega E}{V} \quad (4.7)$$

The first term of JWL equation, known as high pressure term, dominates first for V close to one (figure 4.23).

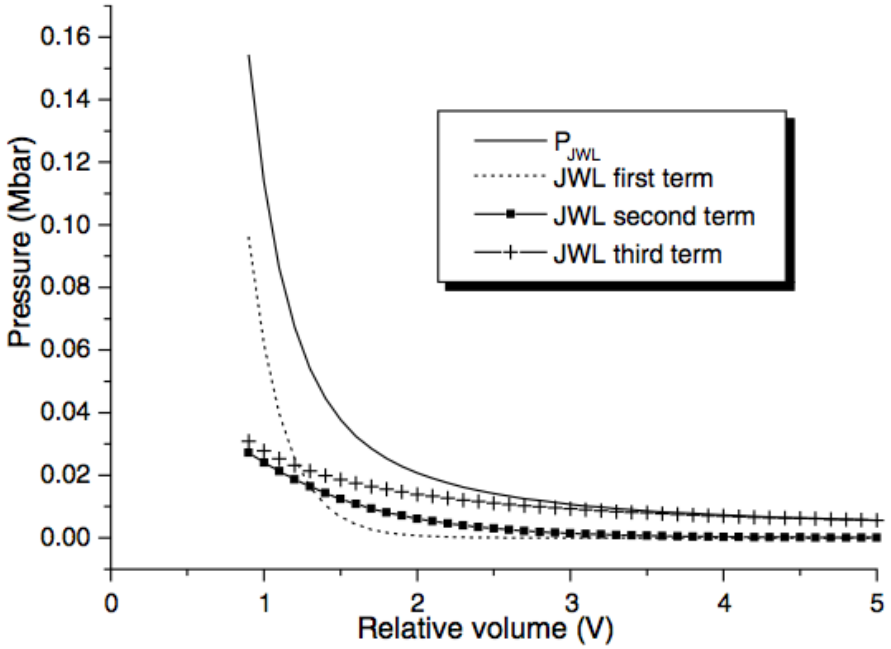

Figure 4.23: Variation of JWL pressure with respect to the relative volume

The second term is influential in the JWL pressure for V close to two.

Observe that in the expanded state ($V \to \infty$), the JWL equation of state reduces only to the third term:

$$p = \frac{\omega}{V} E \tag{4.8}$$

The last term is the polytropic equation of state for air. With $\omega = \gamma - 1$, the JWL pressure matches asymptotically the ideal gas pressure for large volumes.

4.4.2 Geometry Mesh and Boundary Conditions

We have built a three dimensional model to develop the simulation. The cubic field has a side of $100cm$ and the length of side of the cubic part of the explosive is $10cm$. Using the density of the explosive we can easily compute the mass of the explosive, that is $1.67Kg$. First of all only the mesh of the air was constructed. Then with the command ***MoveCpy** we are able to move (or copy) some elements from the part of air and assign to it the properties of the explosive part. The cubical charge is surrounded by the air mesh such that there is one-to-one node match at the boundary between the explosive model and the air models.

We create a mesh with fixed element size. The mesh has $2cm$ element size. Thus the model consists of 125000 elements. So to reduce the size of the models we have put the charge in one of the corner and in order not to have the reflection of the wave along the faces of the cubic field, we impose specific boundary conditions with the keyword ***Boundary non reflecting** in all the faces of the cube. To do this we first s have to create a ***Segment Set** and then assign to this selection of elements the non reflection conditions.

One other thing to do is to define the type of element that we want to use. So in the ***Section** keyword we have to define both the parts of air and

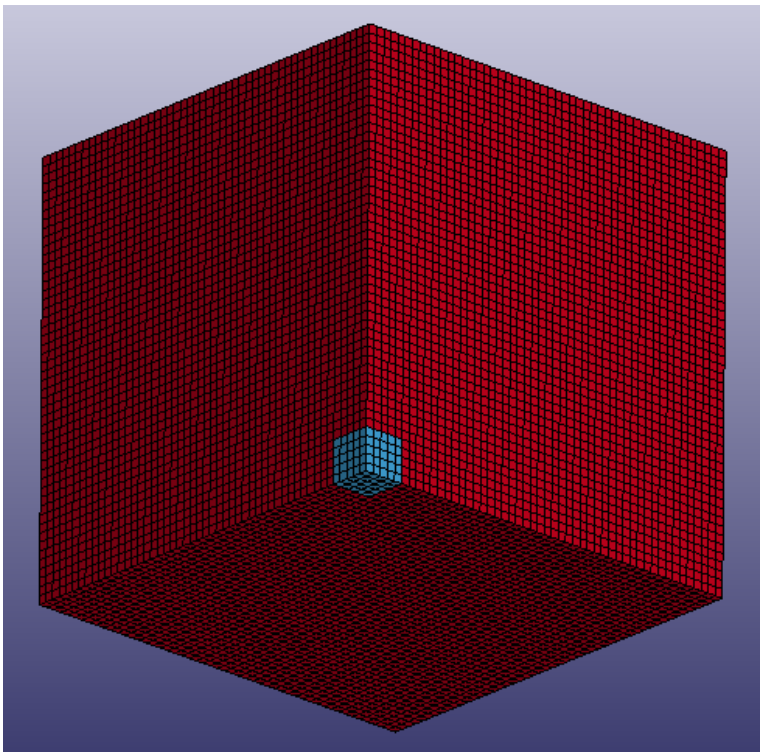

Figure 4.24: Mesh of the first model with element size=2cm

explosive as solids element with element formulation 11 that corresponds to the Multi Material Ale formulation, that we have in detail described in the previous section. When there are more than one ALE part we have to define each part in the section called ***Ale Multi Material Group Part**. Moreover when high explosive are present in the model we have to define the point source of the detonation with the keyword ***Initial Detonation**. In the ***Part** card we summarize all the information about the air and the explosive, setting the materials, the EOS, the element formulation and optionally the hourglass control. If the hourglass control is not defined a default value is computed by the software.

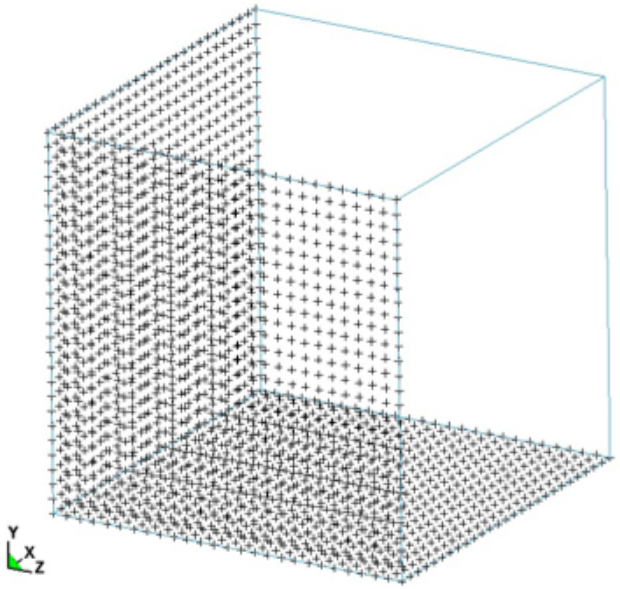

Figure 4.25: Imposition of the non reflecting conditions

4.4.3 Output Controls and Database Definition

In the explicit time integration, the time step length is determined by the smallest element size in the model. Therefore, the mesh density should be as uniform as possible. Unnecessarily small elements should be avoided, because they make the time step size small, thus increasing the computational time. Extremely large elements should be avoided as they decrease accuracy. Mixing of small and large elements in the same model should be also avoided as much as possible because such models tend to reduce simulation accuracy. Fluids are especially difficult to model because they undergo large deformations, and element shapes and sizes can change considerably during the Lagrangian cycle of the ALE time step. The Van Leer algorithm (Leer, 1984) is applied to remap the conservative variables. An explosion is a complex phenomenon, which requires good modelling techniques.

We set the termination time such that the pressure wave reaches the opposite face of the cube, so we set $T = 500\,\mu s$ and a photography of the progress of the problem every 1 μs. So we can clearly see the wave propagation. Then we also want to see the pressure time history in various point of the field to evaluate some characteristics parameters such as the peak of the overpressure and the shock front velocity. We take the series of the gauges along the edge so that we can compare the results of the analysis with the experimental formulas of Heinrych (Henrych, 1979), to evaluate the rightness of the calculations.

4.4.4 Analysis Results

During the explosion simulation, a gas bubble forms and expands. Consequently, air adjacent elements are violently pushed in front of the bubble. A high velocity shock front starts from the explosive source to the surrounding air. A shock is a narrow discontinuity in the pressure wave, and therefore would require fine mesh resolution in order to capture a reasonably accurate shock peak pressure. We now want to see if the air mesh is fine enough to match accurately the shock pressure that originates from the explosive.

Formation and propagation of the shock-wave

First of all in this problem we want to validate the hydrodynamic multi material ALE approach to simulate the detonation of explosive material and the subsequent propagation of the pressure wave. So the first thing that we want to see is the formation and the propagation of the shock-wave. Some picture of the pressure wave propagation at different times are shown in the pictures 4.26 , 4.27 ,4.28 ,4.29 .

As shown in the pictures, in a first time, the presence of the reacted

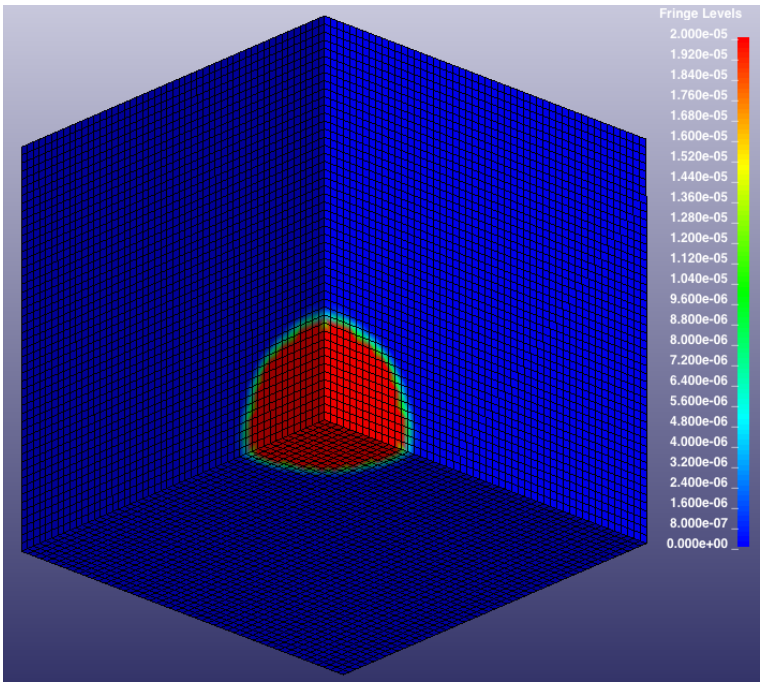

Figure 4.26: Pressure wave propagation t= 50μs

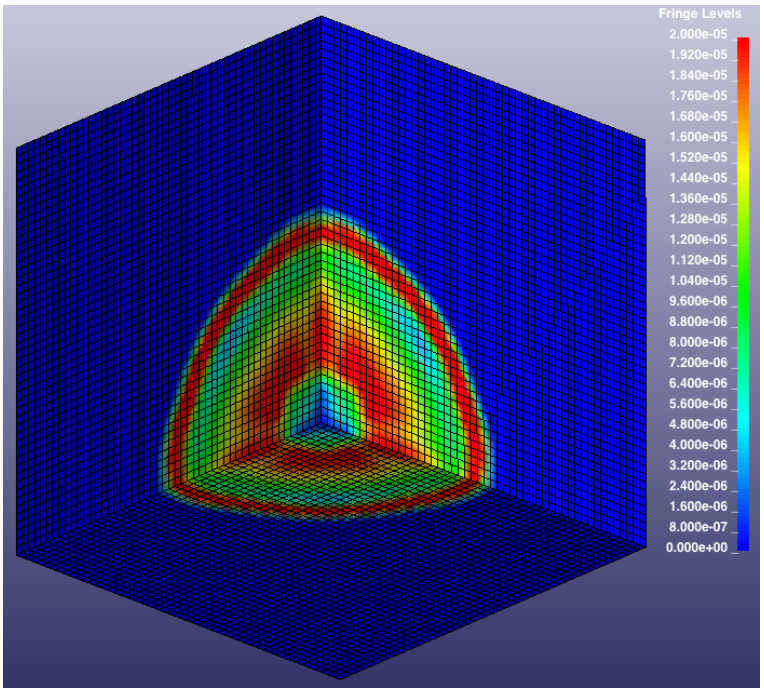

Figure 4.27: Pressure wave propagation t= 130μs

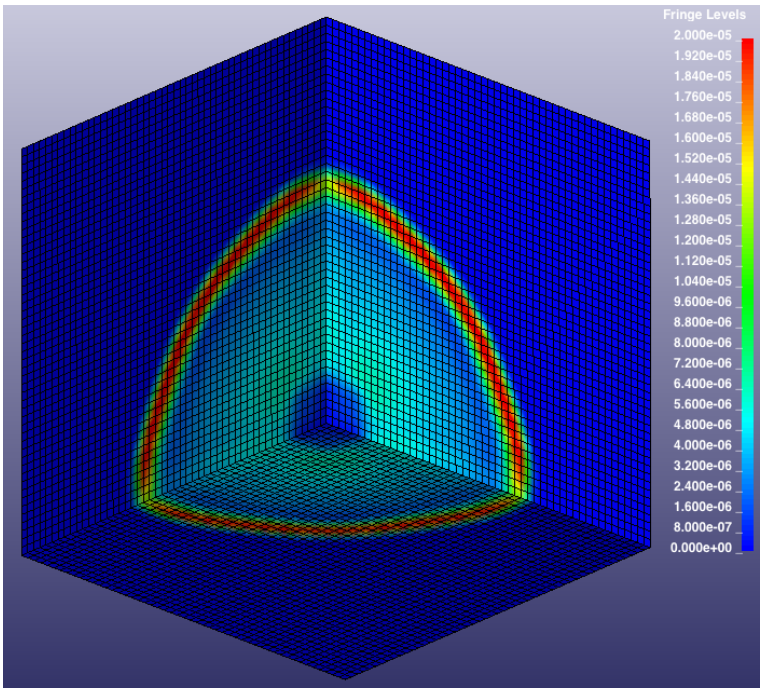

Figure 4.28: Pressure wave propagation t= 260μs

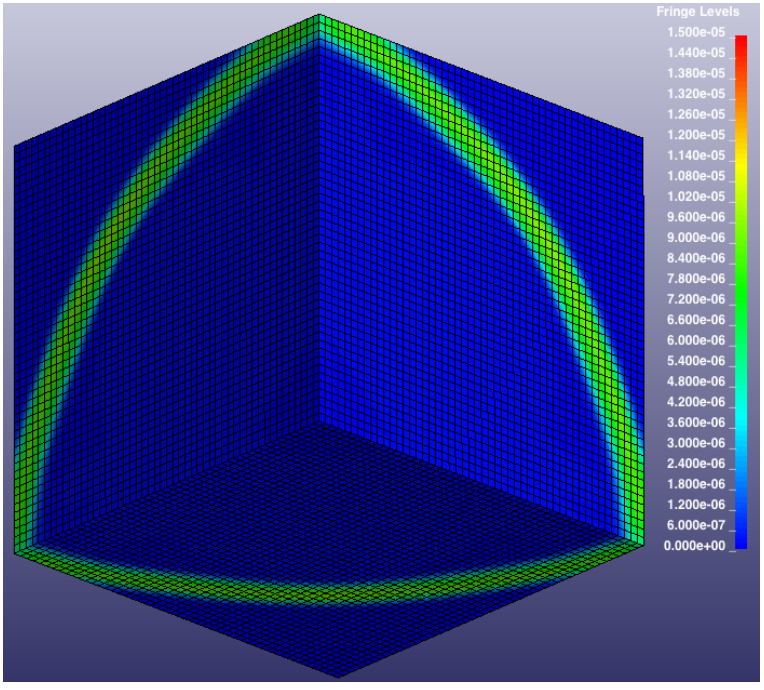

Figure 4.29: Pressure wave propagation t= 500μs

explosive is very important, so that there is a region near the explosive at very high pressure. Going forward in time we can see that this high pressure region quickly dissolves, and the shock-wave propagates. The other thing that it is possible to see is the peak of the overpressure. The scale range is fixed and setted to 2 MPa, and we can clearly see that the pressure in the shock front decrease rapidly as a function of the distance of the detonation.

Time History data

A shock-wave has a lot of characteristic parameters such as its shape, the time arrival, the peak of overpressure and the shock front velocity. To show this phenomena we investigate a time history in different points of the cubic field. First of all we present the time history of a single point, to show the basic shape of the pressure wave, and then we compare it with the other ones to show the decreasing peak of the overpressure. The figure 4.30 shows the element history of element $n.20$ and the figure 4.31 shows it again in comparison with the other element of the same edge with steps of $10cm$. It is clearly visible the decrease of the peak of pressure.

To validate these results we compare the values of the Henrych analytic formula, that give us the values of the overpressure in function of the scaled distance defined by the (5.2). We show a graphic with in abscissa the scaled distance $\overline{R}$ and in ordinate the peak of the overpressure. The empirical formulations given by Henrych are:

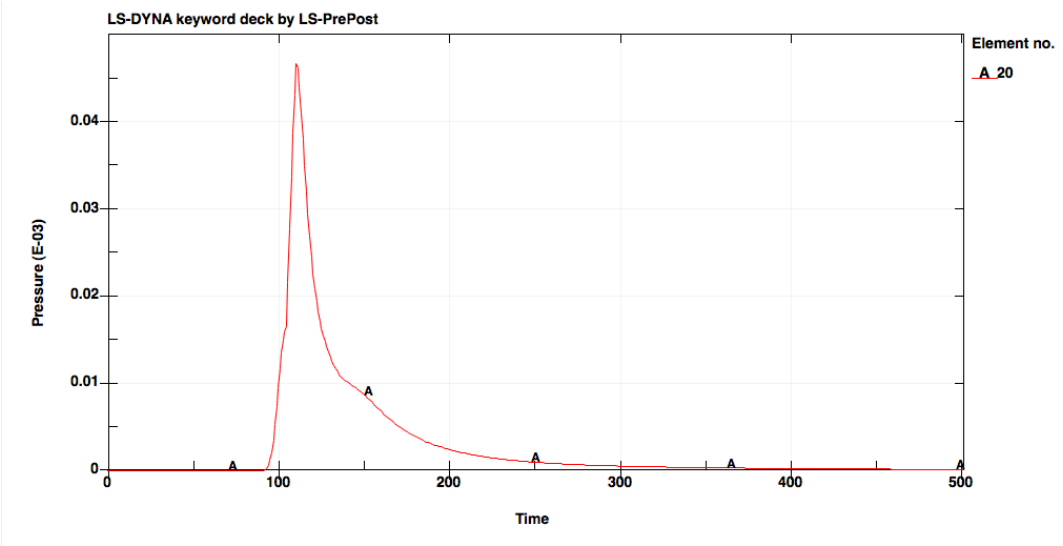

Figure 4.30: Thime History element n.20 dist: 40cm

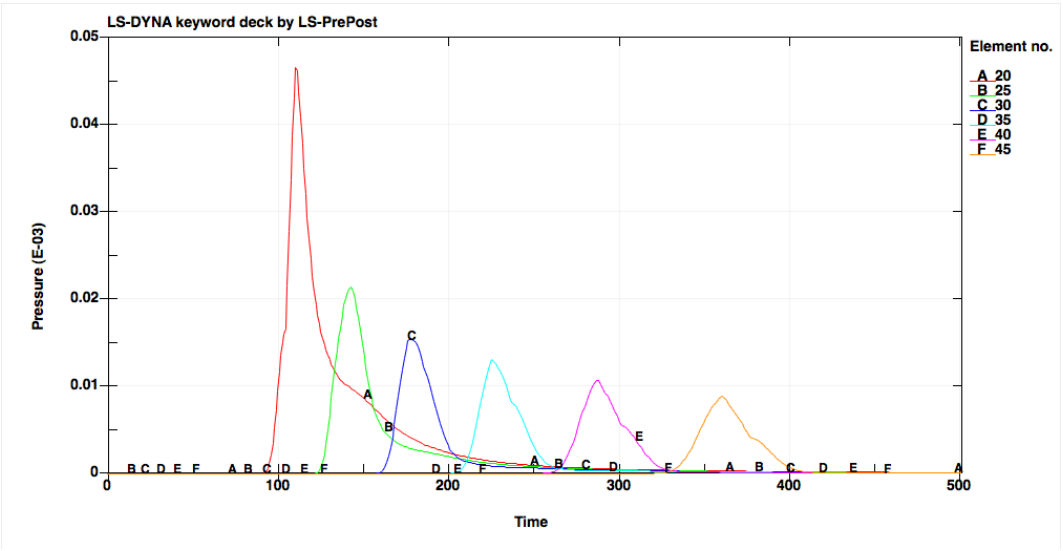

Figure 4.31: Thime History from element n.20 to element step: 10cm

$$\Delta p_\Phi = \frac{14.0717}{\overline{R}} + \frac{5.5397}{\overline{R}^2} - \frac{0.3572}{\overline{R}^3} + \frac{0.00625}{\overline{R}^4} \quad [kp/cm^2] \quad for \quad 0.05 \leq \overline{R} \geq 0.3$$

$$\Delta p_\Phi = \frac{6.1938}{\overline{R}} - \frac{0.3262}{\overline{R}^2} + \frac{2.1324}{\overline{R}^3} \quad [kp/cm^2] \quad for \quad 0.3 \leq \overline{R} \geq 1 \tag{4.9}$$

$$\Delta p_\Phi = \frac{0.622}{\overline{R}} + \frac{4.05}{\overline{R}^2} + \frac{3.288}{\overline{R}^3} \quad [kp/cm^2] \quad for \quad 1 \leq \overline{R} \geq 10$$

For 1.67 Kg of TNT and for a distance from $0.14m$ to $1m$ we obtain the graphic of figure 4.32

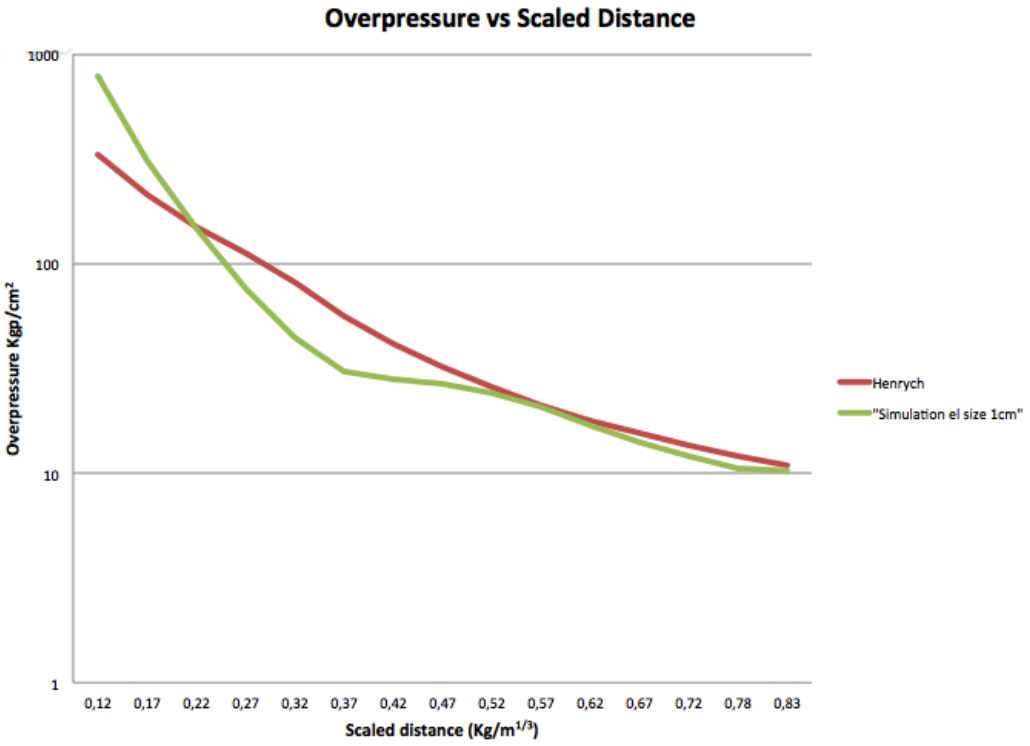

Figure 4.32: Comparison between Heynrich trend and simulation

that show the typical trend given by the Henrych's formulations and the trend of the value obtained with the simulation. The value of the overpressure

are given in the table 4.4.4

Dist R	Scaled Distance $\overline{R}$	Henrych Overpressure	Simulation Overpressure
(m)	$(m/kg^{1/3})$	(Kp/cm^2)	(Kp/cm^2)
0.14	0.118	331.93	780.54
0.20	0.169	221.59	311.39
0.26	0.219	148.33	146.54
0.32	0.270	111.29	75.98
0.38	0.320	81.06	44.19
0.44	0.371	56.13	30.62
0.50	0.421	41.35	27.94
0.56	0.472	31.93	26.63
0.62	0.523	25.60	24.29
0.68	0.573	21.14	20.77
0.74	0.624	17.88	17.02
0.80	0.674	15.42	13.96
0.86	0.725	13.52	11.96
0.92	0.775	12.09	10.53
0.98	0.826	10.80	10.25

Table 4.3: Comparison between the values of the overpressure by Henrych and by the numerical simulation

In order to validate the symmetry of the problem, we show in a unique figure 4.33 the graphs of the time history of the overpressure in three different points, that have the same distance from the detonation. We see that the graphs are perfectly overlapping.

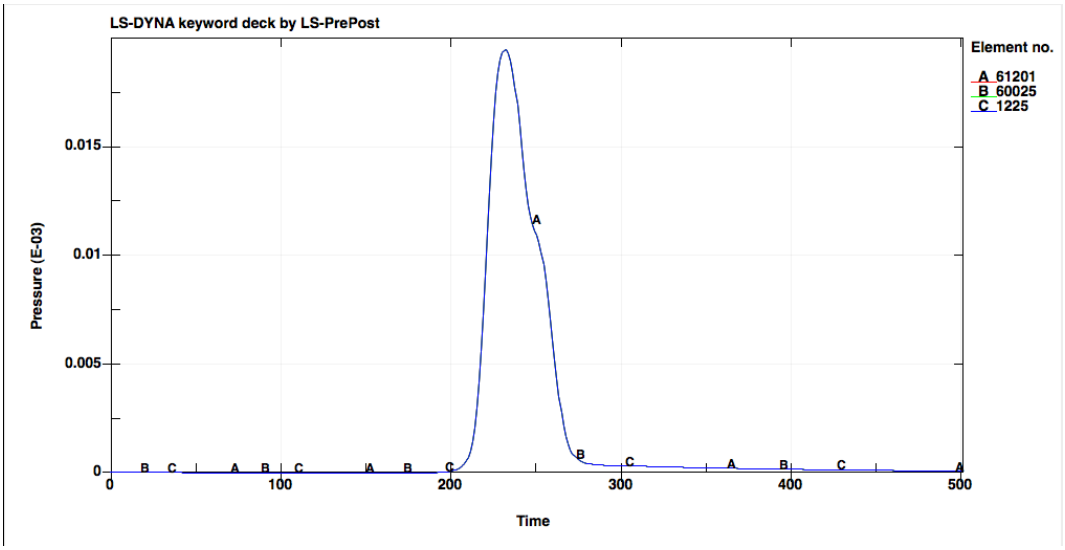

Figure 4.33: Thime History in the same elements of different faces of the cubic field

Shock Front velocity

The arrival time of the shock-wave front at different points can be used to calculate the velocity of the shock front. With the knowledge of this velocity the pressure can also be obtained trough the Rankine-Hugioniot relationship.

Kingery (Kingery and Bulmash, 1984) calculates the shock front velocity depending on pressure as :

$$u = c_0 \left(1 + \frac{\gamma + 1}{2\gamma} \frac{p_{max}}{p_0}\right)^{1/2} \tag{4.10}$$

where

- The parameter γ (ratio of specific heat of air) depend also on the over-pressure and can be taken from a table in (Kingery et al., 1964) and is defined as :

$$\gamma = \frac{c_p}{c_v} \tag{4.11}$$

with c_p being the specific heat at constant pressure and c_v the specific heat at constant volume. Both the specific heat ratio and the speed of sound depend on the temperature, the pressure, the humidity, and the CO_2 concentration. Kingery (Kingery and Bulmash, 1984) defines the variation of the specific heat ratio with a range of 1.402 to 1.176

- c_0 is the sound velocity in air (331 m/sec)
- p_{max} is the peak of the overpressure
- p_0 is the atmospheric pressure (101.3 KPa)

Using this formula and with the peaks of the overpressure computed in the simulations we calculate the different velocities of the shock front in function of the distance from the charge. We can also compare these results with the velocity calculated with a simple difference method from the data of the simulations. We take the peaks of two elements history at different distance from the charge and, assuming constant the velocity between the two peaks with the basic formula of uniform rectilinear motion (s/t) we can easily calculate the velocity of the shock front. We also have to assumes the first velocity equal to the detonation velocity $D = 6930m/s$. The results are shown in picture 4.34.

These results are validates by the graphic always by Kingery (Kingery and Bulmash, 1984) that shows the trend of the various parameters of a shock-wave. In particular the lines that describe the trend of the velocity appear at the bottom of the graphic and confirm the rightness of the simulation. As we can see, in the region near the explosive, the velocity is quite similar to the detonation velocity D that depends on the explosive material and has

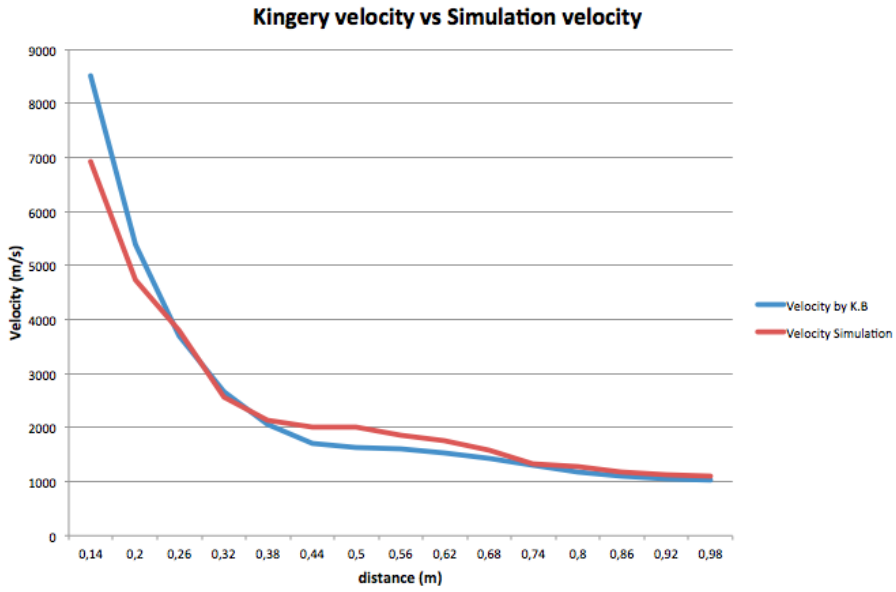

Figure 4.34: Comparison with the velocity calculated with Kingery and manually from the data

the order of magnitude of the wave propagation in solids like:

$$D = \sqrt{\frac{K}{\rho}} \tag{4.12}$$

Where K is the elasticity modulus of the explosive and ρ his density. We can also see that the velocity computed appears higher that the velocity set in the pre-processing job. This can be due to the fact that the explosive required a very fine mesh. Nevertheless the velocity in the region more distant from the detonation point, the velocity are well reproduced.

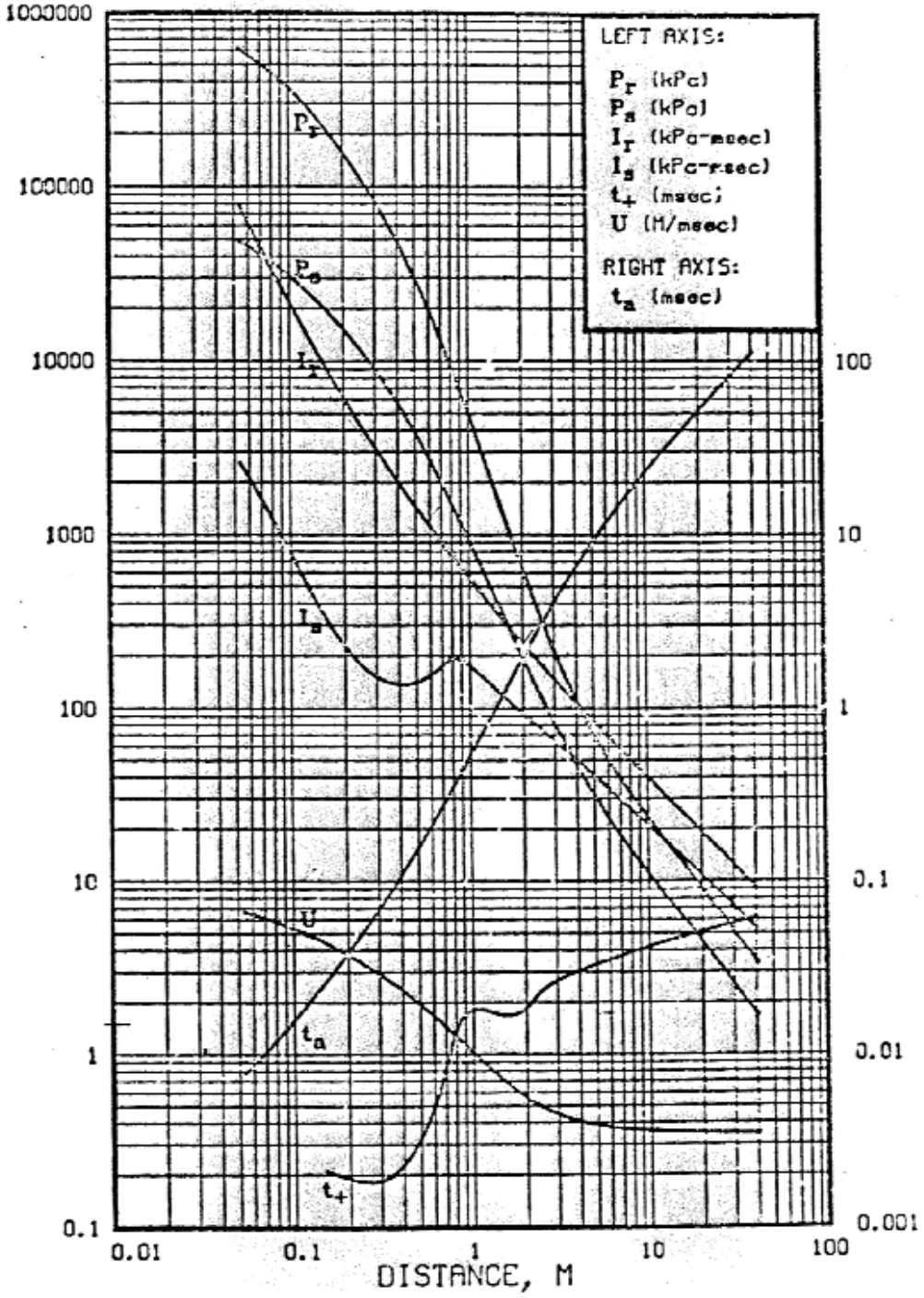

Figure 4.35: Trend of the shock-parameters by Kingery

4.5 FSI Simulation of the interaction of shock-waves with Lagrangian Structures

4.5.1 Introduction

In this kind of problems we set up the interaction of an explosion, simulated trough the Multi Material Ale formulation described before, with a Lagrangian structure. We are in the case where there is a fluid in motion (air) at high pressure that interacts with a solid initially standing. We have to set up a Fluid Structure Interaction simulation. In the case described before 4.3.1 we not model the explosive and the subsequent pressure wave propagation, but we direct apply the pressure load. Here we want to show if it is possible model the pressure load with the Fluid Structure Interaction. The ALE formulation has a more elevated computational cost with respect to the CPNWEP method, thas does not take in account some aspects such as:

- the region of enforcement of the pressure load is single. There is no interaction in other parts of the structure
- the reflecting wave is not computed

CONWEP capabilities is very indicate to have an idea of blasts problems and for specific applications, where the explosive is very near to the structure. The Fluid Structure Interaction problems, in the other hand, takes in account all these situations because the fluid is modelled and can interact with all the Lagrangian elements. In particular ALE formulation with FSI is necessary when dealing with problems in wich reflected waves are not a negligible part of the problem i.e. ground reflection and other obstacles. The Fluid Structure

Interaction problems are computationally very expensive so the model, and the mesh have to be very well designed.

To set up a Fluid Structure Interaction problem in $LS-DYNA$ we have at least one ALE part and one Lagrangian part and we can use two ways:

- Coupling of the *ALE* and *Lagrangian* formulation with the command **Costrained Lagrange in Solid*
- Merge the contact nodes (double) between the mesh of the fluid field (ALE or Eulerian) and the mesh of the structures.

With the first method we need to accurately set the option of the command to have a right interaction. In particular we have to define what is the *Part of the model that enforces the stresses to the others. This part is called *Master* and usually is the fluid ALE part. Then we have also to define one or more parts that undergo the interaction, that are usually the solid Lagrangian parts. These are called *Slaves* parts In order for a fluid-structure interaction (FSI) to occur, a Lagrangian (structure or slave) mesh have to spatially overlap with an ALE (fluid or master) mesh. Each mesh should be defined with independent node ID. $LS-DYNA$ searches for the spatial intersection of between the Lagrangian and ALE meshes. Where the meshes overlap, there is the possibility that interaction may occur. With the second method we have to know that the shared nodes works as Lagrangian 's.

In the sequent sections we construct 2 models to verify if a Fluid Structure Interaction problem is suitable to simulate explosive situations. The first simple problem considers an explosion in front of cantilever beam and the second one the explosion in front of a standalone column. In the first one

the interaction is only between the shock-wave and the beam. In the second one the interaction is other than with the column also with the ground.

4.6 Cantilever Beam under 1KG TNT detonation

In this problem we want to show the interaction of a cantilever beam under a shock-wave due to the explosion of $1Kg$ of TNT. The beam have the same geometry of the one used for the conwep simulation (4.3). To have visible interaction between the blast wave and the beam we have to set the charge near the beam at the distance of $1m$. Also the charge is set as $1Kg$ due to the mesh design, in particular to the fact that we need a minimum of element for the explosive to have a good simulation. In this problem we want to show the pressure wave that impact and enforce the stress to the cantilever beam. We should see the wave that deforms and the reflecting wave. We can also see the x-stress propagation.

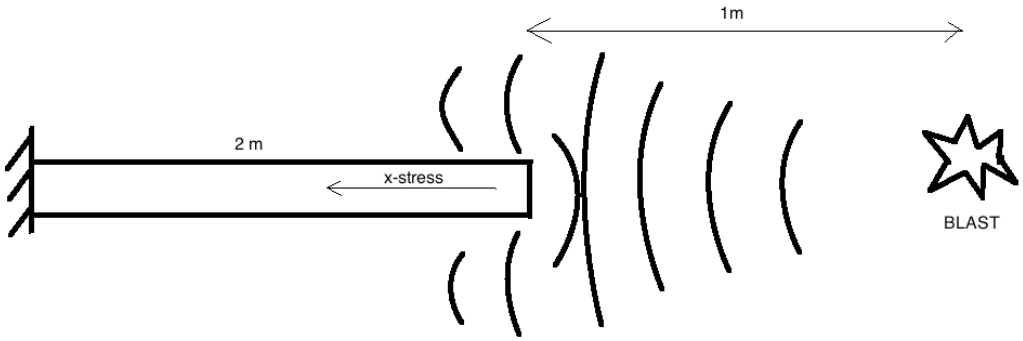

Figure 4.36: Description of the physic problem

4.6.1 Numerical model

We build a model with an uniform mesh of hexahedral elements with 8 nodes per element. We set and discretized the domain of the air, of the beam and the explosive as follows:

- Air (ALE Part 1)
  - $300cm$ in x direction with 150 elements
  - $30cm$ in y direction with 15 elements
  - $50cm$ in z direction with 30 elements
- Explosive (ALE Part 2)
  - $10cm$ in all the directions with 5 elements
- Beam (Lagrangian Part 3)
  - $200cm$ in x direction with 100 elements
  - $10cm$ in y direction with 10 elements
  - $10cm$ in z direction with 10 elements

As we have written before in order to obtain an interaction, the slave part, in our case the beam, have to intersect the part of the master, the air (figure 4.38) . Thus first we model the air and then moving or deleting some part of its we construct the mesh of the other parts. We remember that the nodes of the air and the explosive have to be coincident, but the mesh of the column and the ground have to intersect the mesh of the air, in order to have a correct interaction . After this we can assign all the needed parameters to each part present in the model. In figure 4.37 we show the entire mesh of

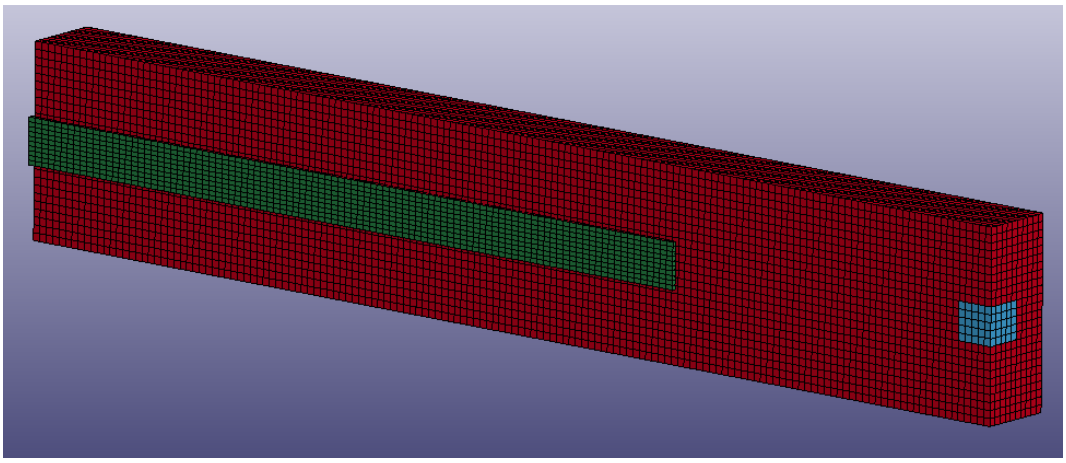

Figure 4.37: Mesh of the fsi-cantilever model

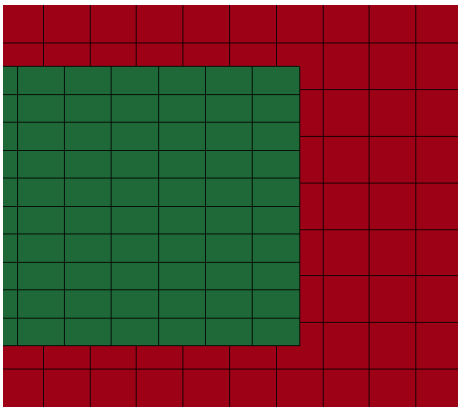

Figure 4.38: Intersection between air and beam

the model and a focus to show the intersections between the mesh of the air and the mesh of the beam .

The element formulation used for the air and the explosive is the multi material ALE elements. Having more than one ALE part, we have to summarize them in the card *ALE MULTI MATERIAL GROUP. In the *CONTROL ALE section, we have to define the parameters of the mesh smoothing and the advection of the ALE mesh. We choose to turn off the smoothing of the ALE mesh, setting the option $AFACT$ equal to 0. Always in this section we

set the pressure applied to the free surfaces of the ALE mesh boundary equal to the atmospheric pressure. The field of the air needs the *BOUNDARY NON REFLECTING conditions, in order to not have the reflection of the wave at the end of the MMALE boundaries.

Materials and Equation of State

Regarding the materials for the air and the explosive, they are the same used for the previous simulation. So we used the ***MAT NULL** with the air associated with the ***EOS POLYNOMIAL** with the parameters of air, and the ***MAT HIGH EXPLOSIVE BURN** with the ***EOS JWL** with the parameters of the TNT. The beam instead refers to the Lagrangian elements formulation. Similarly to the conwep problem we choose the ***MAT ELASTIC** and we set a low Young modulus in the way to better appreciate the x-stress propagation in the beam. For the same reason the Poisson ratio is set as 0. With this choice we only have longitudinal wave propagation. The parameters of air and TNT are summarized in tables 4.4 4.5 (Aquelet and Souli, 2008).

mid	ro	pc	mu	terod	cerod	vm	pr
1	0.001225	0.00	0.00	0.00	0.00	0.00	0.00

Table 4.4: MAT NULL parameters of air

mid	ro	D	Pcj	beta	k	g	siav
1	1.67	0.747	0.25	0.00	0.00	0.00	0.00

Table 4.5: MAT HIGH EXPLOSIVE BURN parameters of air

For what concerns the parameters of air we have only to set the density

(ro). For the explosive material we have to specify also the detonation velocity D and the *Chapman Jouget* pressure. The other parameters are not strictly needed (Hallquist, 2006).

The parameters of the EOS for the air and for the TNT are summarized in tables 4.6 4.7.

eosid	c0	c1	c2	c3	c4	c5	c6	e0	v0
1	-1.0e-06	0.00	0.00	0.00	0.40	0.40	0.00	2.58e-06	1.0

Table 4.6: EOS LINEAR POLYNOMIAL parameters for air

eosid	a	b	r1	r2	omeg	e0	v0
2	5.409	0.0937	4.5000	1.1000	0.35	0.08	0.80

Table 4.7: EOS JWL parameters for TNT

The meaning of each terms of the two EOS are specified in the previous sections.

4.6.2 Results

Here we show the results of the simulation. First of all the progression of the shock-wave and the impact with the beam are shown. We observe the wave that changes shape and the reflecting wave. Then the stress in the beam begins to propagate. Then we show a time-history graphics with the incident wave progression, the reflecting wave and the x-stress propagation. Then by using the time history data we calculate the propagation velocity of the wave inside the beam, and we compare it with its analytical value.

As we can see the reflected pressure is lower than the incident pressure. This because the reflecting surface is very small and the wave switches to

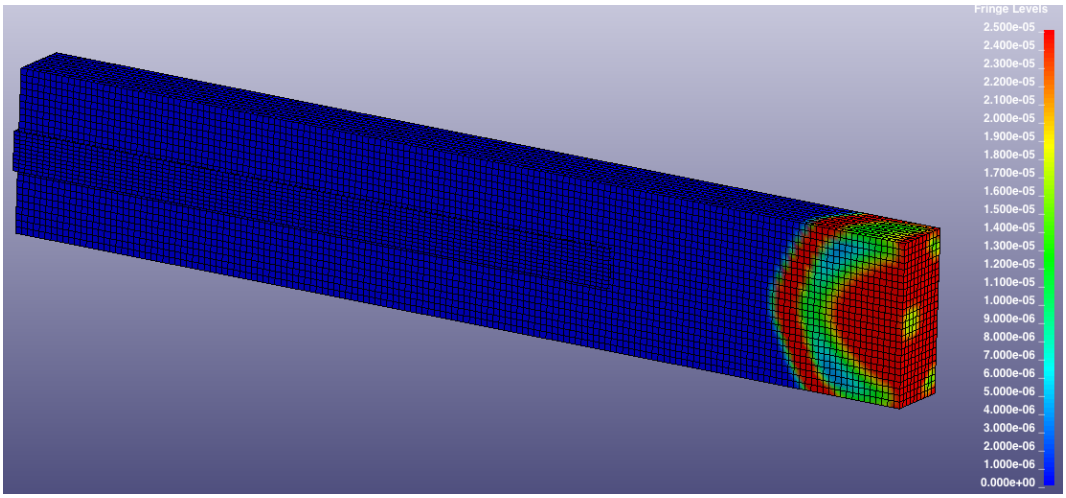

Figure 4.39: Shock-Wave propagation t=120 μs

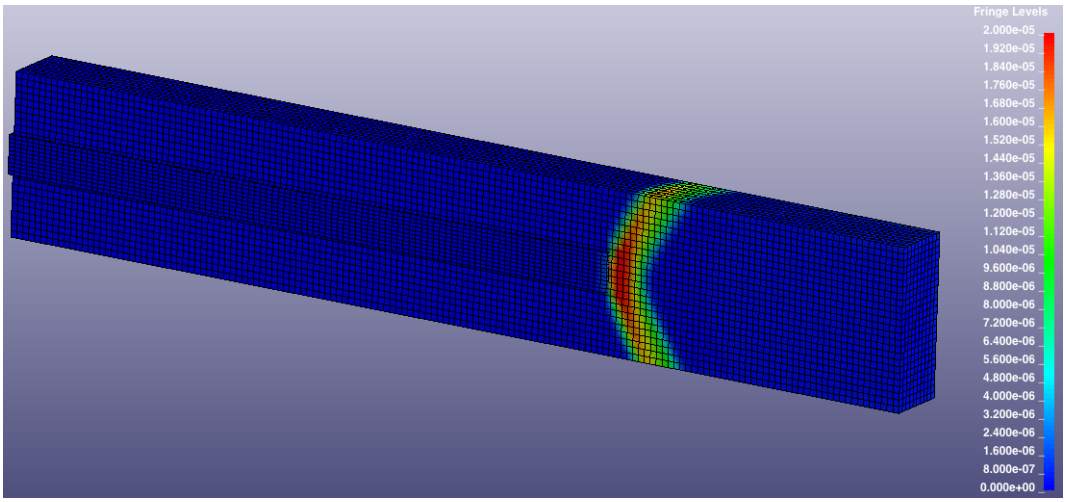

Figure 4.40: Shock-Wave propagation t=298 μs

the side of the beam. In the pictures 4.45 4.46 we focus on the x-stress propagation in the beam.

As we can see in the time history data at the beginning we have compressive x-stress , and also after the wave reaches the clamps. Then, in the second turn the x-stress are reversed and the elements are in traction. The propagation is not well defined like in the CONWEP simulation with the

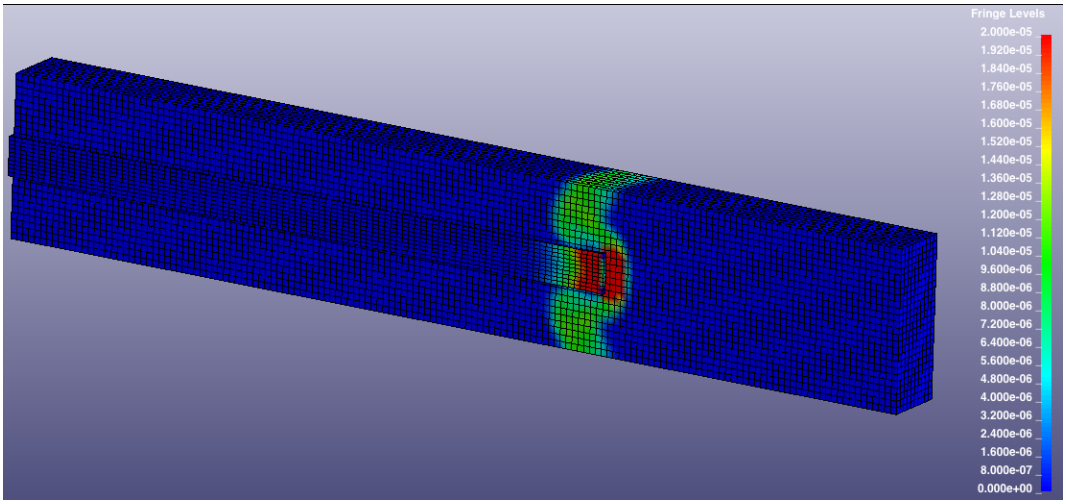

Figure 4.41: Shock-Wave propagation t=354 μs

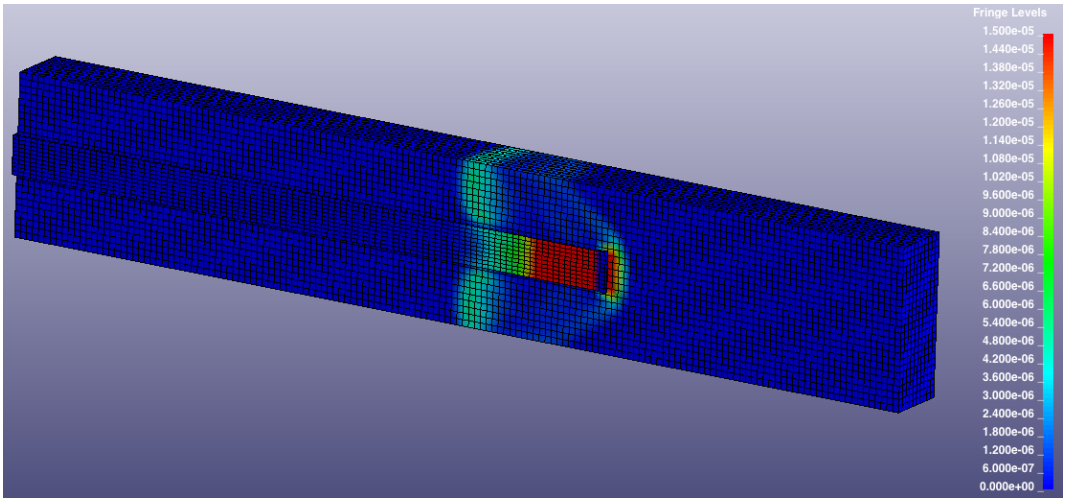

Figure 4.42: Shock-Wave propagation t=469 μs

fine mesh, because the shape of the pressure function is altered, due to the presence of the air, that in this simulation is modelled.

We compute also the history of another element far from the previous one by $40cm$. So we can calculate the velocity of the wave propagation in the beam, assuming it constant in that time interval.

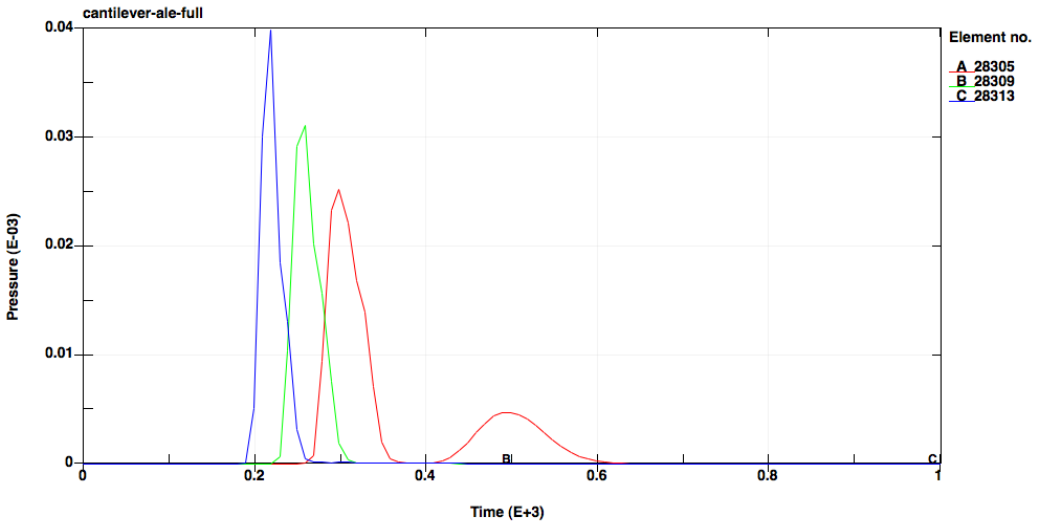

Figure 4.43: Incident arrival pressure

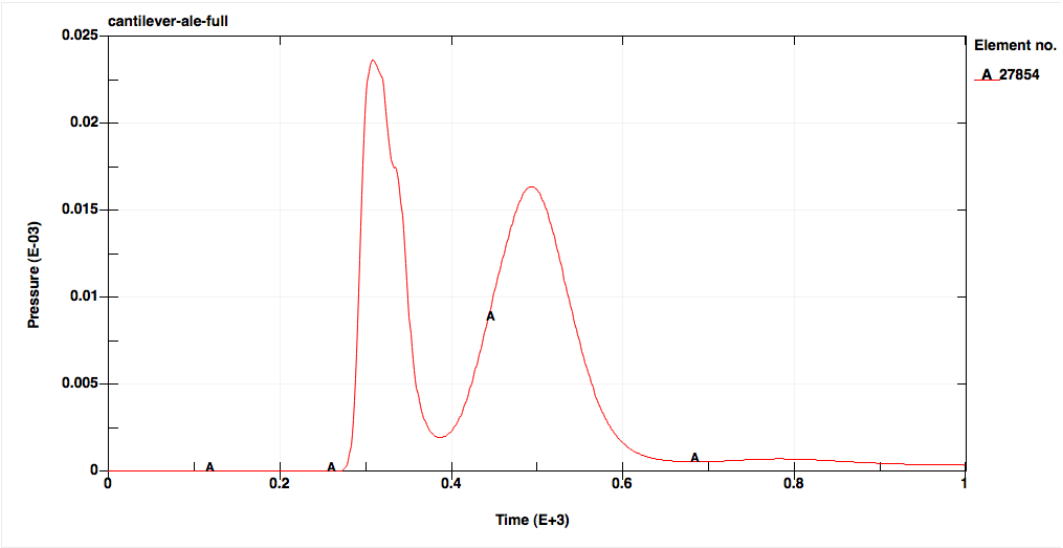

Figure 4.44: Incident pressure and reflected pressure

With the data downloaded by the history files we take the time of the two negative peak of pressure of the two different elements. The data are summarized in the table 4.8 .

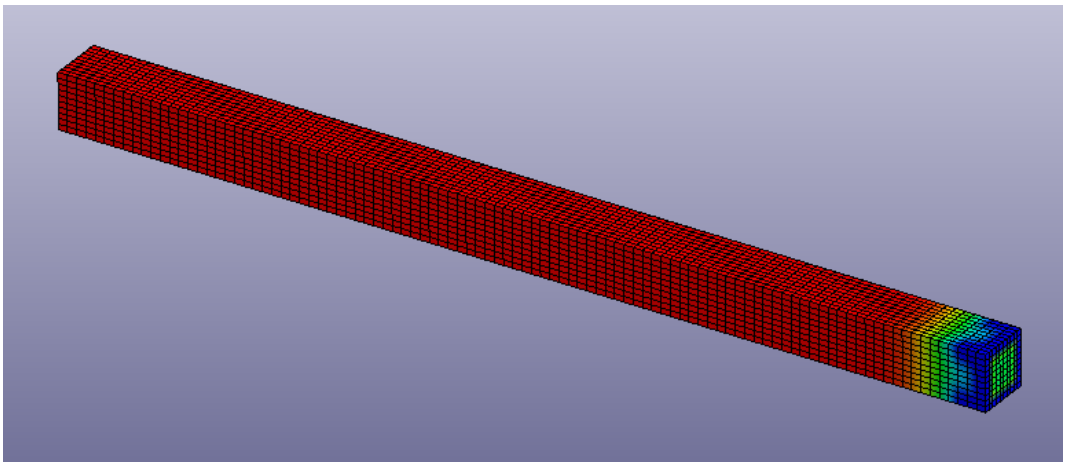

Figure 4.45: X-stress propagation 1

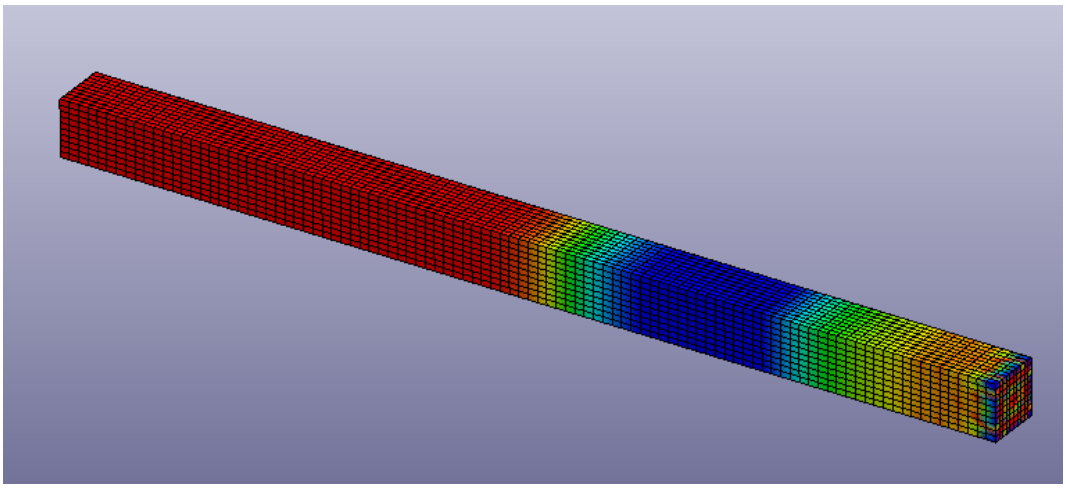

Figure 4.46: X-stress propagation 2

time (μs)	**x-stress (Mbar)**
958.9	$-2.63e^{-4}$
1039.36	$-2.45e^{-4}$

Table 4.8: Time and intensity of the peak of stresses in the two elements

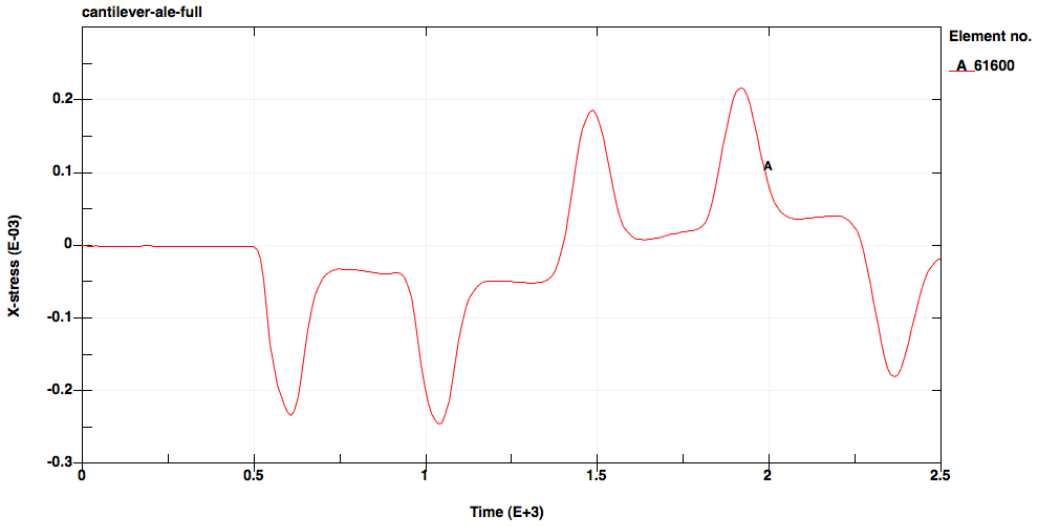

Figure 4.47: History of the x-stress propagation in the central element of the beam

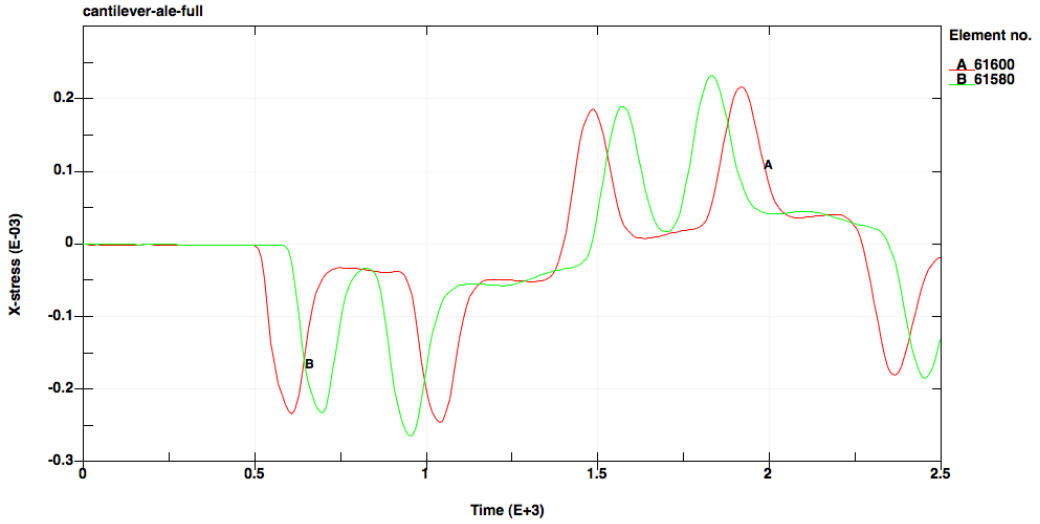

Figure 4.48: History of the x-stress propagation in the two different element of the beam

With the formula of the wave propagation in solids:

$$D = \sqrt{\frac{K}{\rho}} \tag{4.13}$$

Where K is the Elasticity modulus of the beam and ρ his density, the

computed value of the wave propagation velocity is $4582m/s$. The two values are in good accordance, so we can say that the result are in good agreement with what we expect.

The computed velocity and the analytical one are summarised in the table 4.9 :

Computed velocity	**Analytic velocity**
$4972m/s$	$4583m/s$

Table 4.9: Computed and Analytic velocity

4.7 Standalone column under 1Kg TNT detonation

In this model we simulate the interaction of the pressure wave generated by $1Kg$ of TNT positioned in front of a standalone column at the distance of $0.7m$. The height of the column is $1.5m$ with a square cross section which sides are $0.12m$. The height of the charge is set as $0.75m$ exactly at the middle height of the beam. In this model the interaction is not only with the column, but we consider also the reflection of the ground. We will focus on the incident pressure wave and the reflected wave. We expect also that the pressure wave switches to the side of the column and reaches the region beside the beam. We expect also that the pressure contour runs along the eight of the beam and continue his trend when reaches the top of the beam. The other things that we want to investigate are the contours of the effective $Von - Mises$ stresses and the displacement along the height of the beam. The figurative description of the model is represented in the picture 4.49.

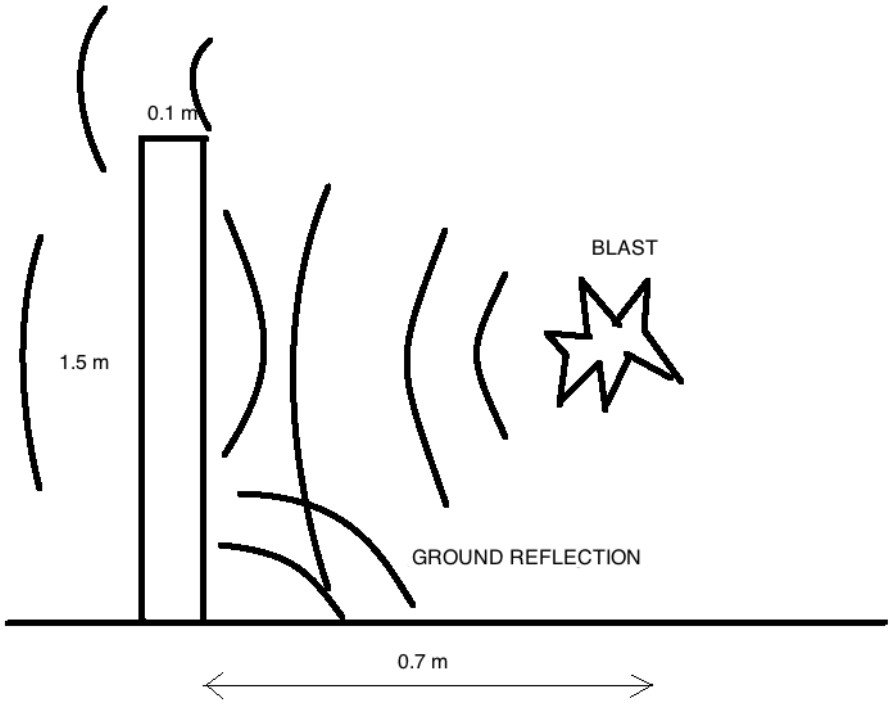

Figure 4.49: Figurative description of the model

4.7.1 Numerical Model

Also in this problem we choose to adopt a uniform mesh of solid elements with hexaedral shape with eight nodes per element. In this model we have 4 parts: two *ALE* parts that are the air and the explosive and two Lagrangian parts that are the column and the ground. The dimension and the discretization of the model are summarized as follows:

- Air (ALE Part 1)
  - $100cm$ in x direction with 50 elements
  - $30cm$ in y direction with 15 elements
  - $200cm$ in z direction with 100 elements

- Explosive (ALE Part 2)
  - $10cm$ in all the directions with 5 elements
- Beam (Lagrangian Part 3)
  - $12cm$ in x direction with 6 elements
  - $12cm$ in y direction with 6 elements
  - $150cm$ in z direction with 75 elements
- Ground (Lagrangian Part 4)
  - $102cm$ in x direction with 51 elements
  - $32cm$ in y direction with 16 elements
  - $2cm$ in z direction with 1 element

For the construction of the mesh we follow the same steps used for the previous model. First of all we model the air and then, moving or deleting some parts of its we construct the mesh of the other parts. We remember that the nodes of the air and the explosive have to be coincident, but the mesh of the column and the ground have to intersect the mesh of the air, in order to have a correct interaction.

We assign the properties of non-reflection to all the faces of the mesh of the air and we impose the pressure applied to the free surfaces of the ALE mesh boundary equal to the atmospheric pressure. Having two parts that interact with the pressure wave we have also to define a ***SET PART**, where we define the two Lagrangian parts. So when it is requested to tell the program what is the *Slave* of the interaction, we set this part set. This is a mandatory step when we have more that one slaves parts as written in Hallquist (2006). All the other setting are equal to the previous simulation.

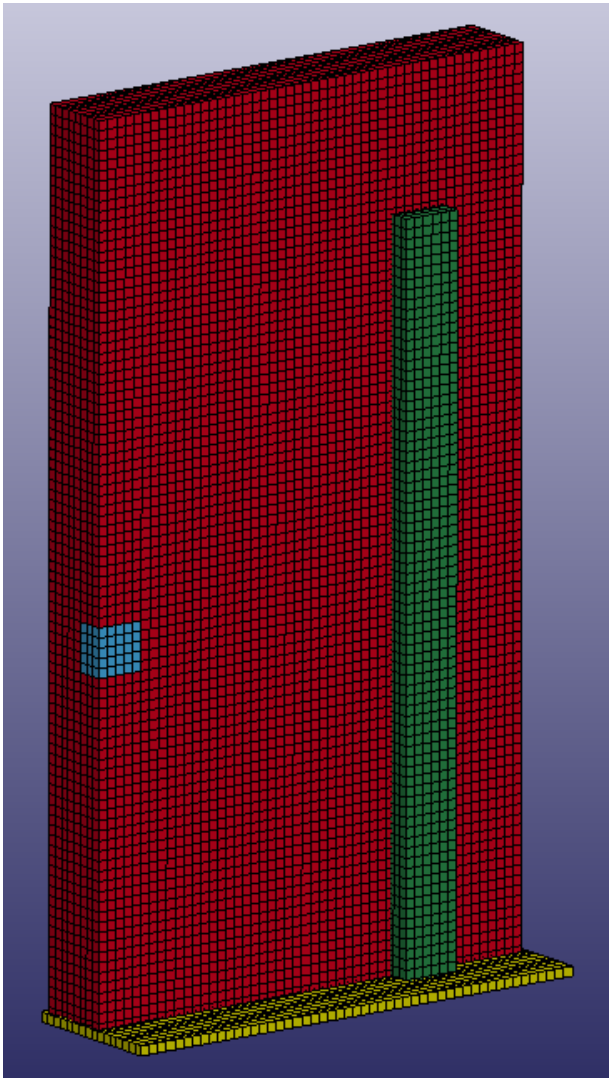

Figure 4.50: Mesh of the fsi-column model

Materials and Equation of State

For what concerns the materials of the *ALE* parts, the air and the explosive, they are the same of the previous model, and also the equation of state are the same. The Lagrangian part has new material properties and in particular we assign for the ground the properties of a rigid body. In order to do this we choose the properties of the elastic material, but we have set a very high

Young modulus. For the column we have assigned the properties of the steel. So both the parts of the column and of the ground are modelled using the elastic material properties. In this kind of material properties we have only to set the density and the Young modulus of the material. The properties of the two materials are summarized in the tables 4.10 4.11.

mid	ro	E	pr	da	db
3	7.8	2.100	0.00	0.00	0.00

Table 4.10: MAT ELASTIC parameters of the column

mid	ro	E	pr	da	db
4	5.00	2100.00	0.00	0.00	0.00

Table 4.11: MAT ELASTIC parameters of the ground

4.7.2 Results

We made this kind of simulation because we want to check if it is possible the interaction with more than one slave part, and if it works well. So the first important thing to verify, is to control if the interaction takes part both with the column and the ground. Then we see that the contour of the pressure impacts first with the beam and then reaches the ground. After this there is a concentration of pressure at the basement of the column. The pressure wave runs along the height of the beam and continues its propagation when the higher point is reached. In the picture 4.51 (a) we see the beginning of the wave propagation, in 4.51 (b) the wave impacts the column, in 4.52 (a) we can see the ground reflecting, so is verified that the interaction happens

in all the slave parts, and we can see also a contour of pressure beside the beam and in 4.52 (b) the pressure reaches the higher point of the column and continues. In the first picture the column is filled with a static colour to better identify its position.

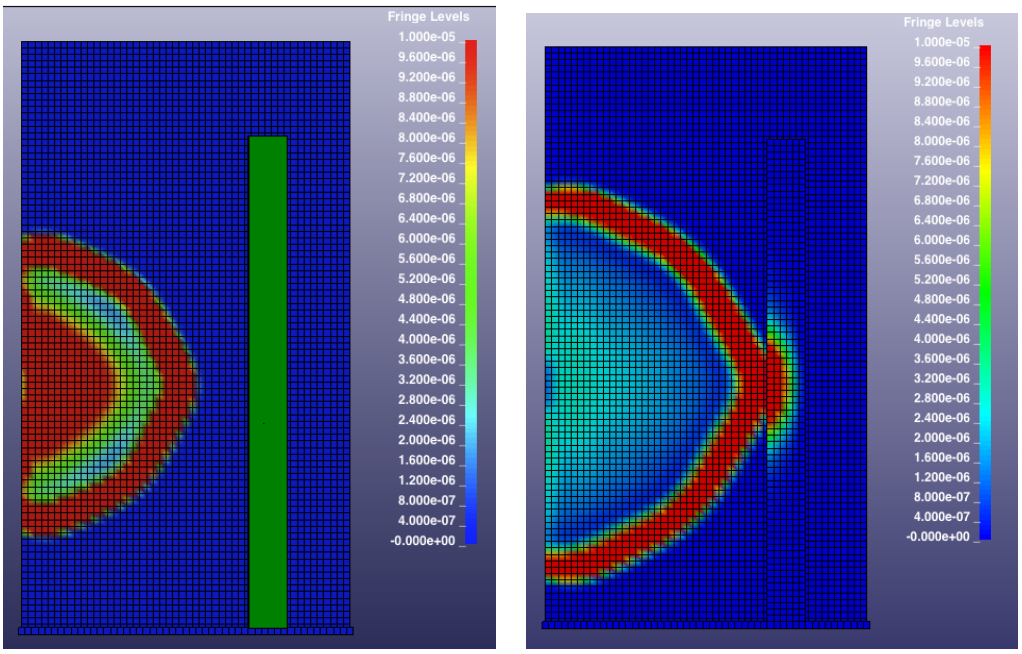

Figure 4.51: fsi-column contour of pressure t=120 μs and t=180μs

A certain quantity of pressure continue at the side of the beam and reach the region beside the column. We want to check how much is the pressure that pass at the side of the beam and compare this value with the intensity of pressure without the column. So a previous simulation without the column has been run. We compare this value of pressure with the pressure detected in the element exactly behind the column and in the element always behind the column but in the left border of the mesh. So we expect an higher pressure in this element because of the passage of the wave at the side of the column.

The comparison between the pressure with and without the column in the two sensors are summarized in table (4.12) :

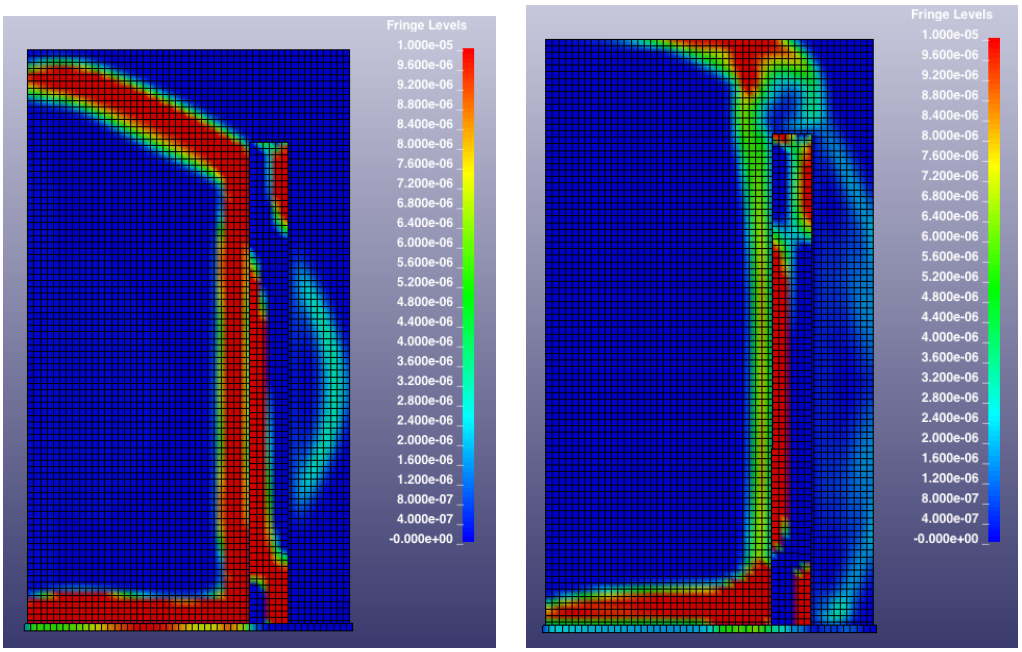

Figure 4.52: fsi-column contour of pressure t=430 μs and t=660μs

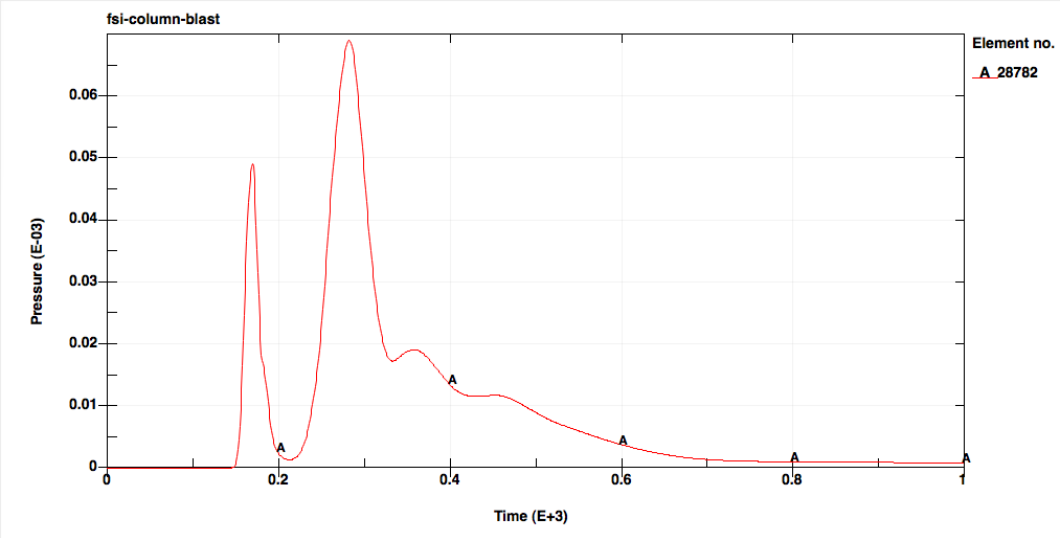

Figure 4.53: Incident and reflected pressure

Now we focus on the distribution of the stresses in the beam, so we choose to investigate the effective Von-Mises stresses, because in this case we

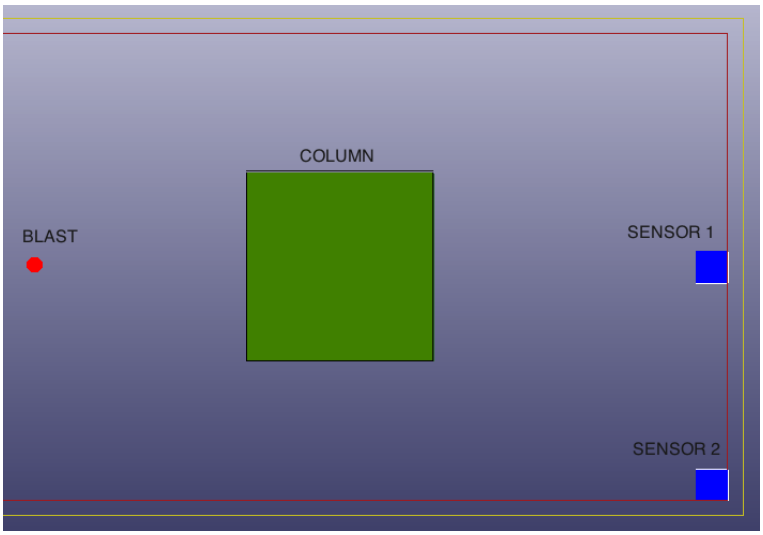

Figure 4.54: Position of the sensor

	Sensor 1	Sensor 2
Without Column	2.67 MPa	2.51 MPa
With Column	0.274 MPa	0.863 MPa

Table 4.12: Detected pressure in the two element with and without the column

have not a preferential direction of propagation. We expect that the stresses begin at the center of the beam and rapidly reaches the two extremities of the column. After this short time the column begins to move and the stresses are concentrated at the basement of the beam.

It's important to see the different maximum value and the trend of the stresses in different point of the beam. So we choose to check the history data in the elements positioned in the center of the height of the column, at the top and at the bottom of the column. First we show only the history of the central element, to evidence the fact that there is first an impulsive force and then a second smoothed load 4.57. In picture 4.58 is shown the

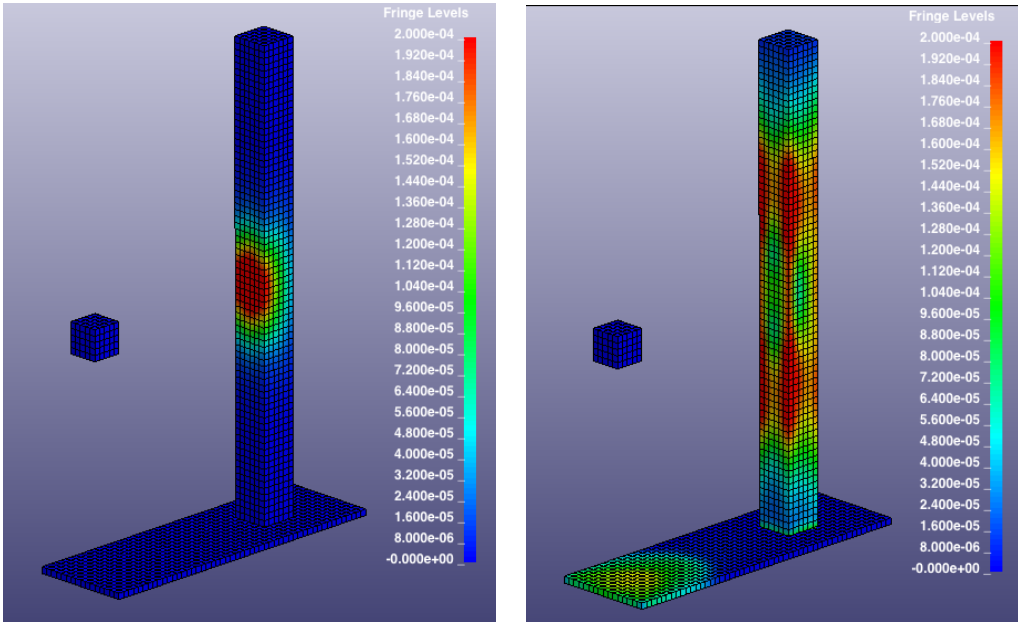

Figure 4.55: fsi-column contour of Von Mises stress t= μs and t=μs

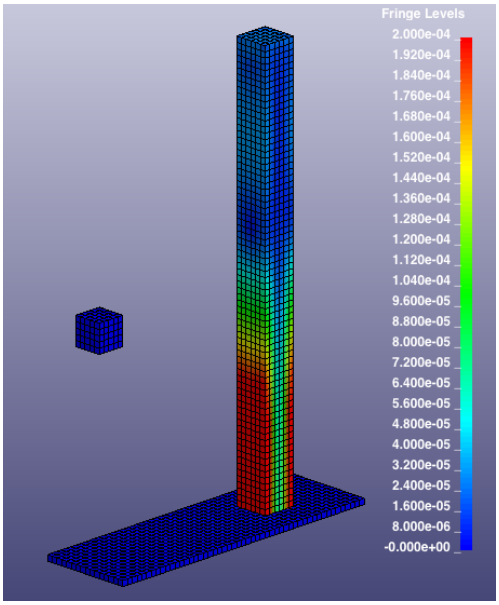

Figure 4.56: fsi-column contour of Von Mises stress t= μs

comparison of the three elements. We can easily note that in the element at the bottom of the column the stresses are significantly higher, but less

impulsive, due to the presence of the ground that make a reflected wave.

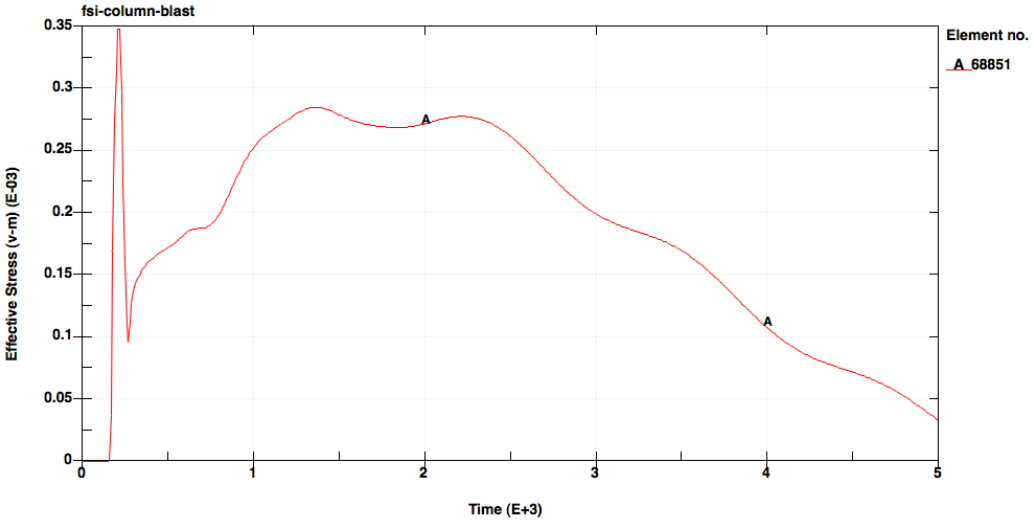

Figure 4.57: history of the von mises stress in the central element of the column

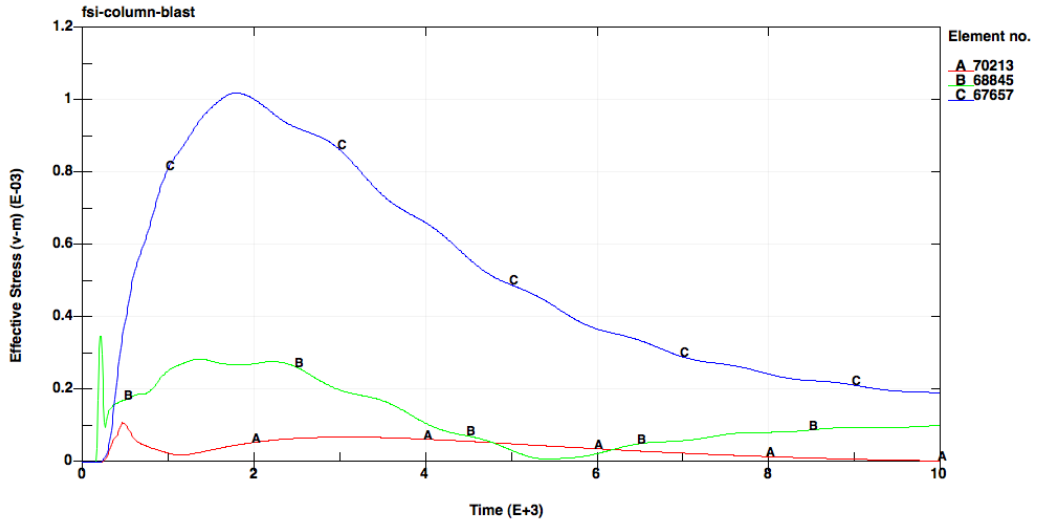

Figure 4.58: comparison of the histories of the von mises stress in the three different elements

An other thing that is significant to see is the displacement in x direction. We show the displacement of elements from top to the bottom of the column.

We expect that the maximum value of displacement are at the top of the column, and decreased up to zero going towards the bottom of the column.

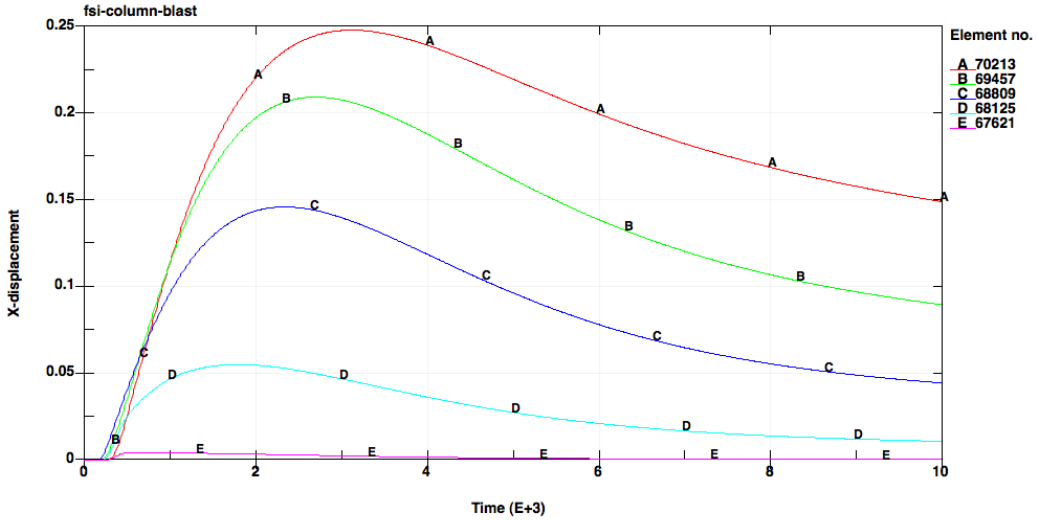

Figure 4.59: displacement in x-direction of element from top to the bottom of the column

Chapter 5

Experimental tests on the SAS GFRP porous barrier and Numerical Simulation

From the analysis of the previous chapters it is evident that in literature there are enough models to evaluate the peak of the reflected overpressure in the open space, only considering the interaction with the ground, i.e in a system where there is any protection between the source of the explosion and the target. There are also models that consider the interaction of the reflected waves with rigid barriers (Army, 1990). Using these models, we are able to evaluate the peak overpressure and compare it with the case of absence of protection. Conversely the analysis of the reduction of the peak overpressure, in case of porous or permeable protective barriers, can not be performed on the bases of existing model.

In this chapter we describe the experimental tests carried out in mine at the University of Naples Federico II. We define the blast configuration and check the experimental data. Therefore we develop a numerical model act

to simulate the experimental test. Finally we compare the numerical results with the experimental data. In particular we evaluate the reduction of the overpressure due to the presence of the barrier.

5.1 Set up of the experimental tests

5.1.1 Geometry of the porous barrier of the SAS project used for the experimental tests

The barrier used for the experimental test in mine is formed by an unique modulus of $2m$ obtained from the fencing used for the SAS project. This barrier consists in a series of tubular elements in $GFRP$ stuck in precast reinforced concrete modulus.

Figure 5.1: Presentation of the configuration of blast test performed in mine

Each concrete modulus is stuck to the ground trough reinforced concrete micro-pipes made, then all of them are assembled each other with joints. This particular assembly system allows to have a compact barrier and easy to build. On each concrete modulus an unique tubular element of

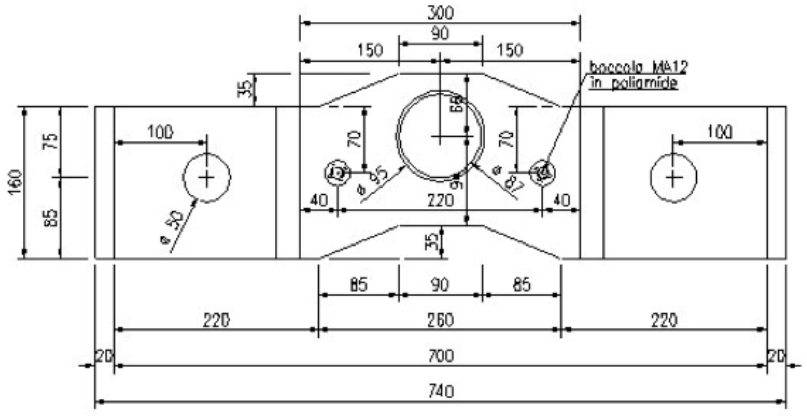

Figure 5.2: Dimensions of one concrete modulus of the SAS project

GFRP is installed . The precast modulus, composed of concrete basement and bars reinforced with glass fiber, always respecting the requirements of radio-transparency and ensuring an higher durability with respect to steel, is conceived with very small dimension in order to confer to the structure an high versatility.

A schematic representation of the dimensions of a single concrete modulus is shown in the figure 5.2; in figure 5.3 is represented the expected reinforcement scheme.

The external diameter of the vertical elements, in composite, is $85\,mm$, and the established step between two elements is $150\,mm$, while the distance between the axis of two adjacent cylindrical elements is $65\,mm$.

The mechanical properties of the concrete and the GFRP bars are summarized in the table 5.1.1 (Asprone et al., 2009)

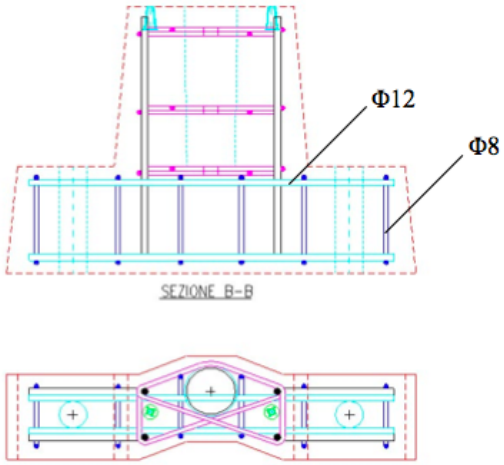

Figure 5.3: Schematic representation of the reinforcement of a concrete modulus used in the barrier of the SAS project

Property	GFRP	Concrete
Elastic Modulus (MPa)	40789	24607
Shear Modulus (MPa)	16316	9843
Tensile Strength (MPa)	648	3
Compressive Strength	648	30

Table 5.1: Mechanical properties of the material that compose the barrier

5.1.2 Blast configurations

The experimental tests have been performed in a mine in the province of Naples. The schematic representation of the test configuration is shown in figure 5.4. In the blast test a constant weight of the charge ($W = 5Kg$), and fixed values of height of the barrier ($H_b = 3m$), height of the charge from the ground ($H_c = 1.5m$), height of the pressure gauges from the ground ($H_t =$

$1.5m$) and distance of the target behind the porous barrier ($D_t = 4m$) have been considered, while the distance between the explosive and the barrier (D_e) is different in the different tests.

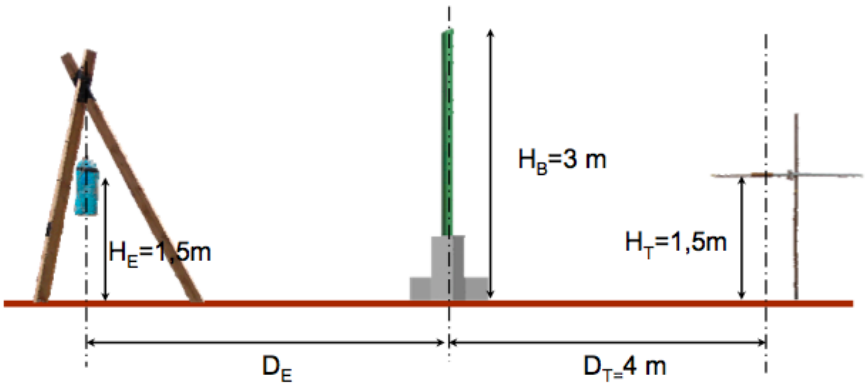

Figure 5.4: Schematic representation of the configuration using during the tests

In the first case the explosive was placed at the distance of $D_e = 5m$ from the barrier , in the second test the explosive was placed at the distance of $D_e = 3m$ from the barrier and finally in the last case the explosive was placed at the distance of

$$D_e = 0.5m$$

from the barrier. The schematic representation of the three blast configurations performed are shown in figure 5.5, 5.6 ,5.7.

As we notice from the schemes, in the first and the second blast other pressure gauges ($S2$,$S3$,$S4$) are placed immediately before the barrier, while in the third test this is not possible, because of the low distance between the position of the explosive and the barrier. For this reason the pressure gauges ($S2$,$S3$,$S4$) are placed immediately behind the barrier at a distance of $1m$. Finally it is possible to notice that in all the three cases also contact pressure gauges close to the barrier ($T1$,$T2$,$T3$) are placed, that allowed

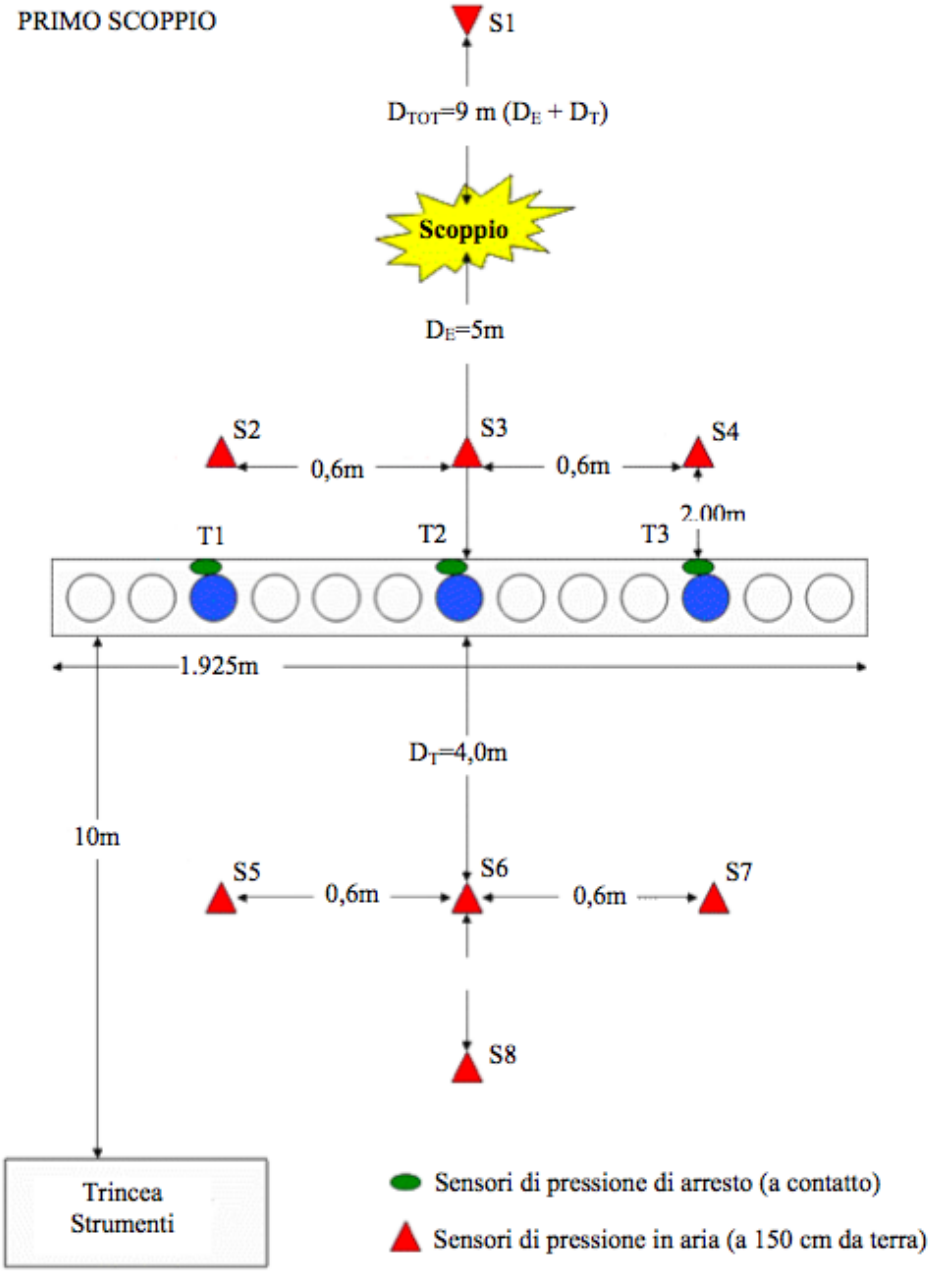

Figure 5.5: First test

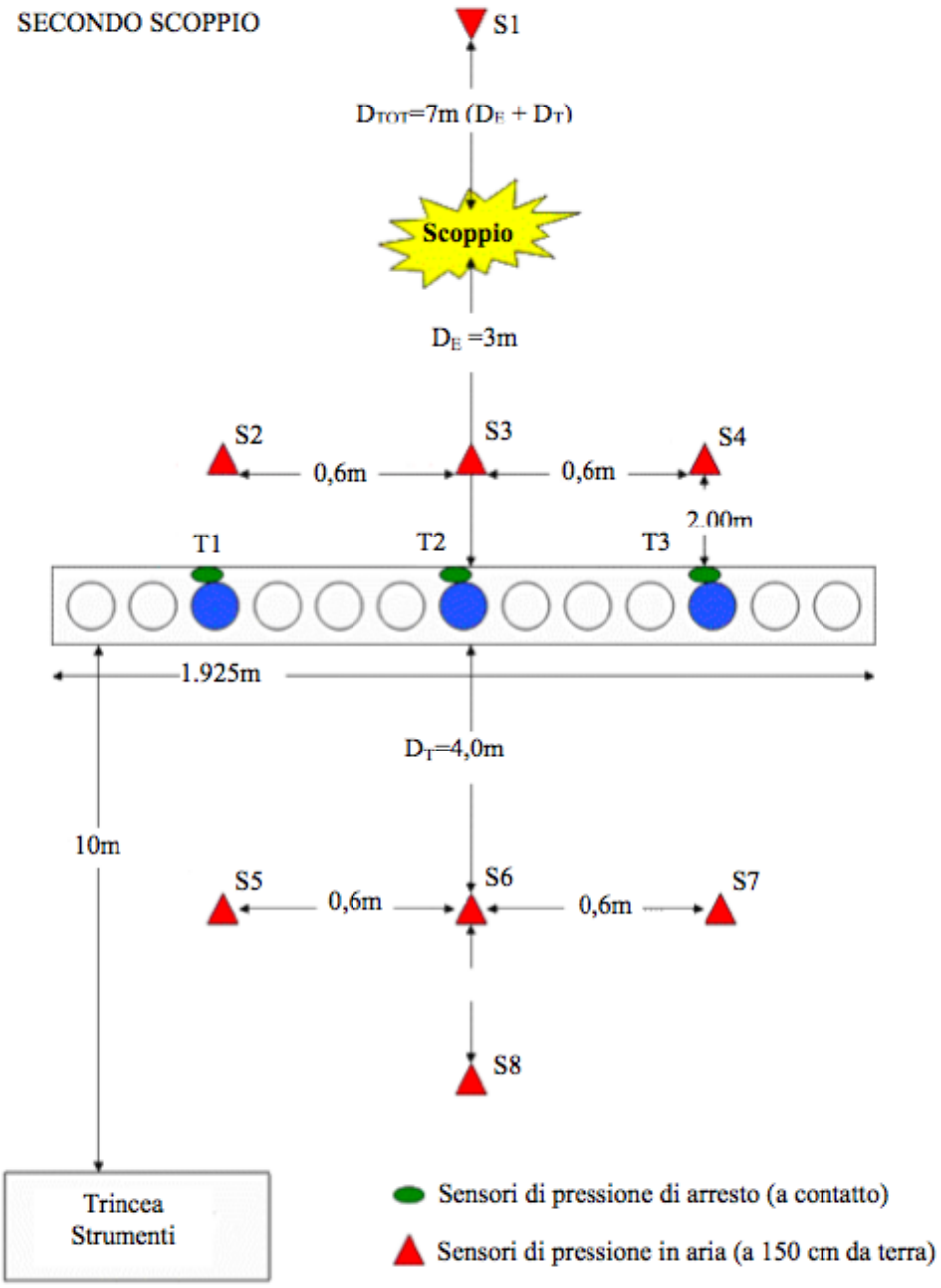

Figure 5.6: Second test

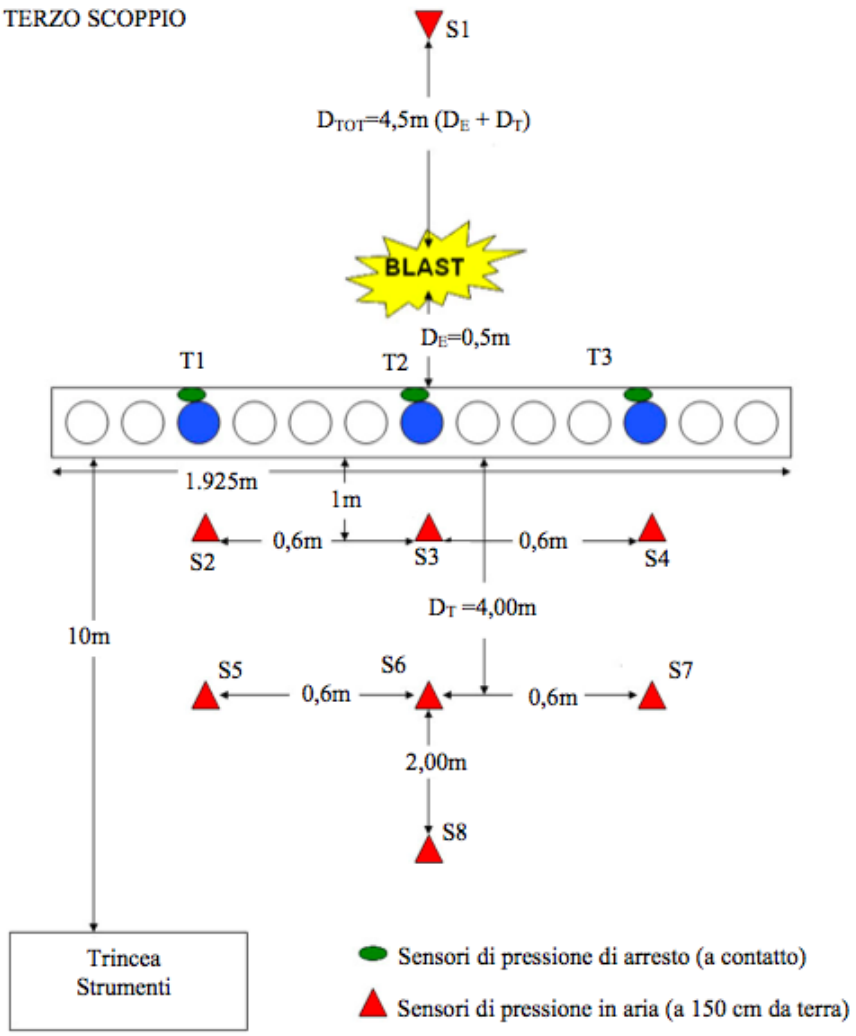

Figure 5.7: Third test

us to evaluate the peaks of reflected overpressure after the contact with the barrier.

5.2 Behaviour of a porous barrier with the interaction with a shock wave

In this section we study the effect of the porosity of a barrier with the interaction of a shock-wave. The model proposed by Hadassah and Doyle (2007) take the assumption that the barrier is perfectly rigid and standing and shows the basics physics of the development of the field flow. The model consist in a sequence of cylindrical pole. The distance W/D indicates the real measure of the porosity of the barrier, where W is the middle point of the cylinder and D the point at the upper surface of the domain. The values taken in exam are for W/D equal to 0.75 , 1 and 2 , to simulate the interaction of more or less porous barriers .

We use the *Shlieren* pictures (Hadassah and Doyle, 2007) to understand the motion of the pressure wave.

Figure 5.8 shows some instants of the diffraction of the shock-wave on a cylinder. The initial impact of the shock wave with the cylinder causes a normal reflection (figure 5.8 (b)). The point generated from the impact, continues to move on the surface of the cylinder until the angle of the wedge between the principal shock wave and the reflected shock-wave becomes too small and a triple point is created. (figure 5.8 (c,d)).

The reflected shock wave propagates on the surface of the cylinder until an impact between the two branches occurs (figure 5.9 (a,b)). After the branches of Mach impacted beyond the pole, the complexity of the flow increases rapidly, because once this initial system of reflected wave is generated, they continue to hurts each other and multiplies along the length of the domain, and thus is difficult to follow their trend and shape. In figure 5.9 (c), the shock arcs overtake the incident pressure wave, so the reflected waves

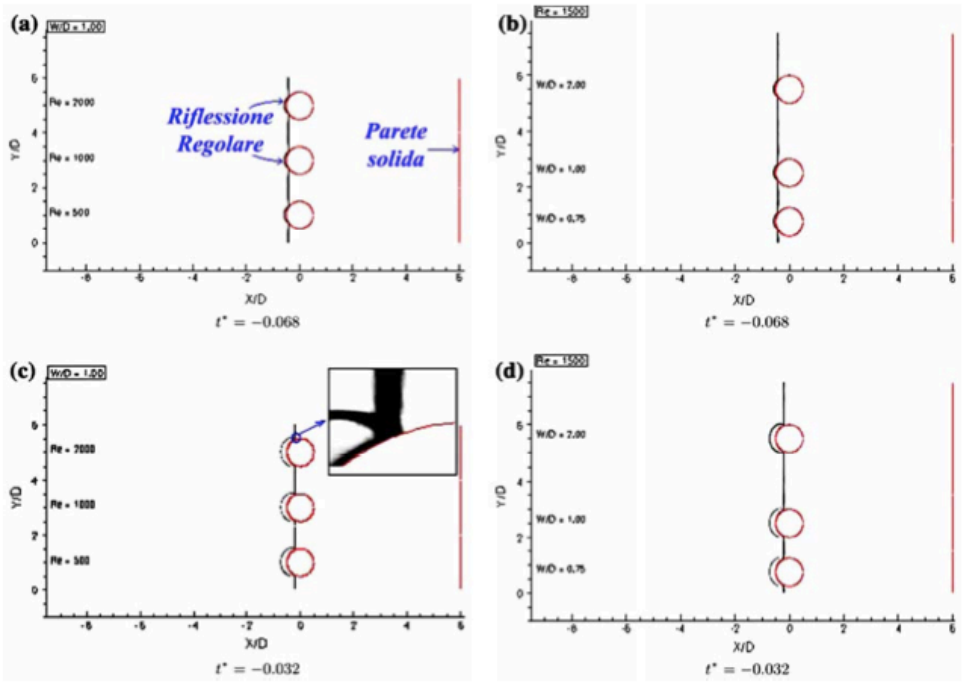

Figure 5.8: Interaction of the wave with the poles t=-0.068 t=-0.032

move quickly than the incidents. Actually none of these reflected waves overtake the frontal part of the shock-wave because once reached the incident wave, are incorporated by it (figure 5.9 (c,d)). When the reflected waves intersect each other beyond the cylinder (figure 5.9 (c)), the new shock front is accelerated. The wave front that is initially curved, after the passage between the barrier, is linearized. This phenomenon is more evident when the porosity is low, because the number of reflection per unit time increases, and thus the interaction between the curved wave and the wave front occurs later. It is possible to say that the cylindrical barrier acts like a convergent canal, accelerating the inflow of the Mach waves as it passes between the pore.

The sudden pressure increment trough this normal reflection causes the separation of the boundary layer, generating vortices beyond the cylinder (figure 5.10 (e,f)). The porosity takes an important role for the creation

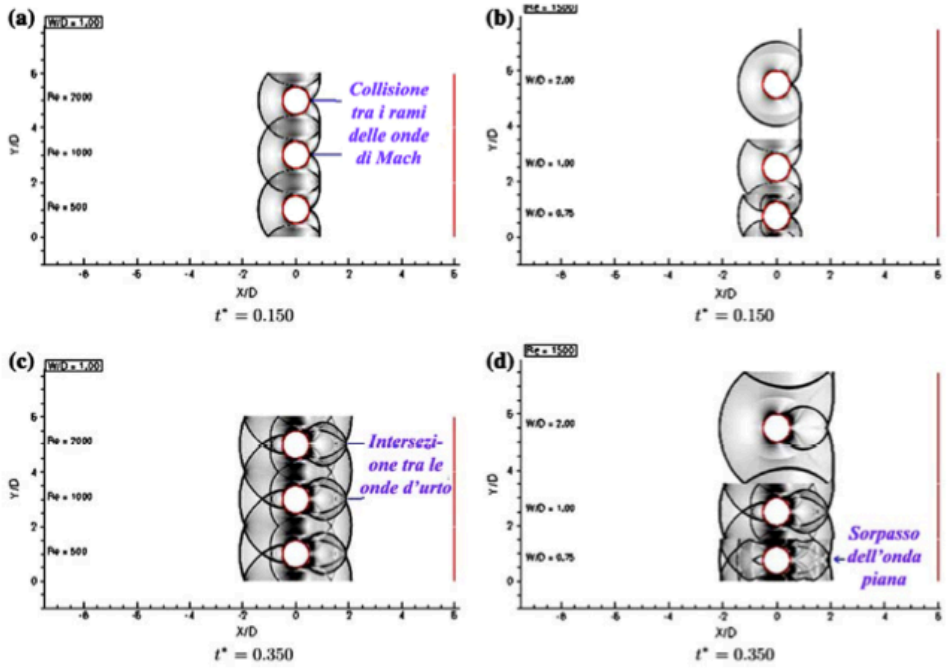

Figure 5.9: Interaction of the wave with the poles t=0.150 t=0.350

and the shape of such vortices. It is possible to notice from figure 5.10 (f) that when the ratio W/D decreases, the region of the vortices increases and the vortices are bigger and stronger, dragging much more fluid behind the barrier.

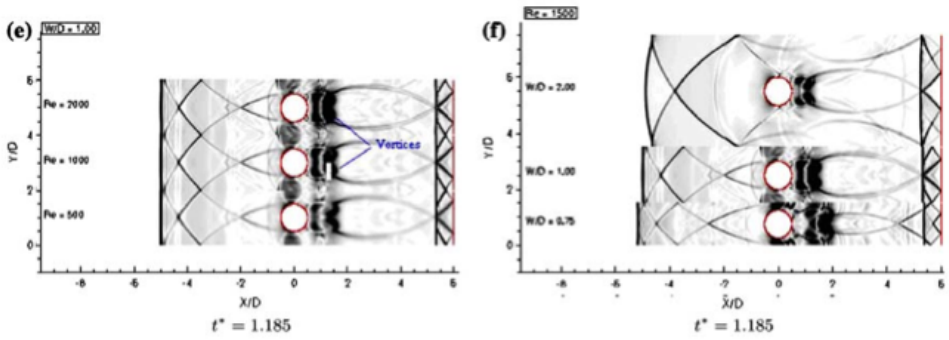

Figure 5.10: Vortices formation behind the barrier

5.3 Numerical Simulationof the SAS project barrier subjected to explosions

In this section we face the numerical simulation of the interaction of the blast wave due to the explosion of $5Kg$ of commercial explosive and the porous barrier described before. We use for the simulation the ALE method and we set up a fluid structure interaction problem, were the field of the air is the *Master* and the barrier is the *Slave* of the interaction. In this problem of interaction we have to define well the parts of the Slave. The interaction is not only with the barrier but we have to take in account also the ground reflection. Another thing to do is to distinguish between the part of the barrier that concerns the basement and the one that belongs to the pipes, because the first is treated as rigid and the second is treated as deformable. Also the ground as assumption is treated as rigid. The pressure wave impacts the barrier: a certain amount of pressure is reflected, the wave returns back in the direction of the source of the explosion, and other amount of pressure pass trough the barrier as described in section 5.2. The blast configuration does not follow the experimental test because we place the charge at the same height of the experiment, but ad a different distance. The explosive is placed at a distance of $1.5m$ from the barrier. We choose it because it is the minimum safe stand-off distance for the barrier in order to have no damages due to the explosion (Asprone et al., 2009). Thus we have the values of pressure when the barrier resist to blast.

5.3.1 Numerical Model

The model of the barrier provides a representation of the existing barrier in full scale. Also in this problem we choose to set up an uniform mesh. The

elements used are hexahedral with eight nodes per element. The elements of the air and the explosive have to share nodes, while the mesh of the barrier, both the pipes and the basement, and the mesh of the ground, intersect the mesh of the air in order to let the program find the nodes were the interaction takes part. For the construction of the mesh we follow the same steps used for the previous problems. So first of all we model the air and then moving or deleting some part of its we construct the mesh of the other parts. The domain of the air is $6.5m$ length in x-direction, $4m$ large in y-direction and $4m$ high in z-direction. We want to give some much space over and at side of the barrier, because we know that the modelled air influences the rightness of the results in comparison to the experimental data, because the amount of the compressed air that passes at the side of the barrier in the reality cannot be checked. So we give some space to let the air surround the barrier and reach its backside, in order to make as real as possible the simulation.

For what concerns the model of the poles of the barrier we do an approximation, due to the complex geometry of the real barrier. The barrier consists in cave cylinder of GFRP. In the model the cylindrical shape is replaced using a parallelepiped shape. In order not to change the mechanical behaviour of the barrier we set the same bending stiffness. Then we compute an equivalent Young modulus E_{eq} , by calculating the moment of inertia of the two shapes we can easily calculate the equivalent elastic modulus E_{eq}.

$$E_{eq} = \frac{E \cdot I}{I_{eq}} \tag{5.1}$$

where E is the elastic modulus of the GFRP bars, I the moment of inertia of the cylindrical pipe, and I_{eq} the inertia of the barrier of the model. The dimension and the shape of the real barrier and the modelled barrier are shown in figure 5.11

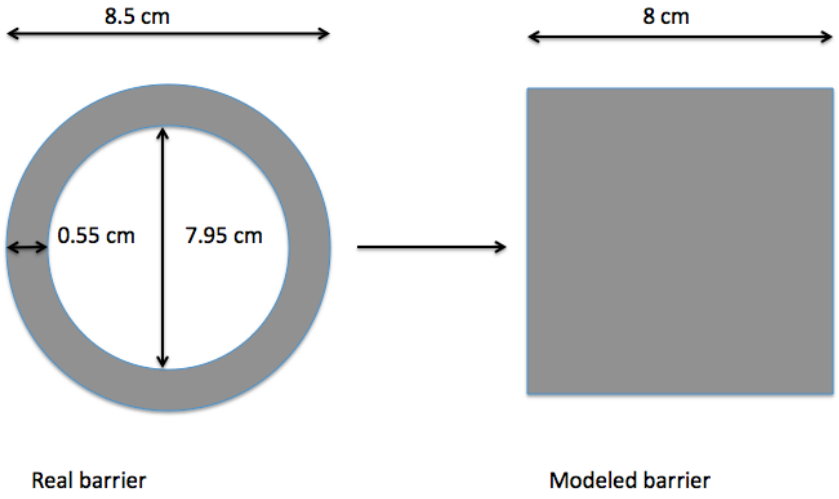

Figure 5.11: Shape of the real barrier and the modeled Barrier

The modelled poles have the following dimension:

- $8cm$ in x and y direction
- $250cm$ in z direction

As said before all the Lagrangian parts have to intersect the mesh of the air, as shown in the figure 5.12.

Thus the model consists of 5 parts; 2 ALE Parts (explosive and air) and 3 Lagrangian parts (ground, basement and bars). Some picture of the model are represented in the figures 5.13 5.14

The element formulation used for the air and the explosive is the $n.11$ that refers to multi material ALE elements. Having more than one ALE part, we have to summarize them in the card *ALE MULTI MATERIAL GROUP. In the *CONTROL ALE section, we have to define the parameters of the mesh smoothing and the advection of the ALE mesh. We choose to turn off the smoothing of the ALE mesh, setting the option $AFACT$ equal to 0. Always

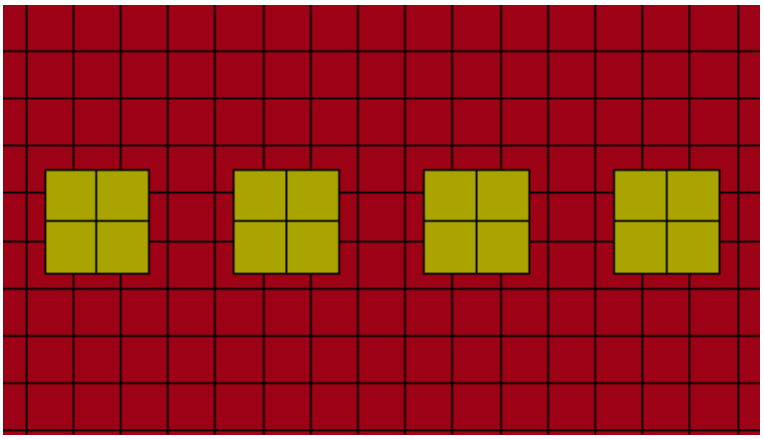

Figure 5.12: Intersections between the poles and the air

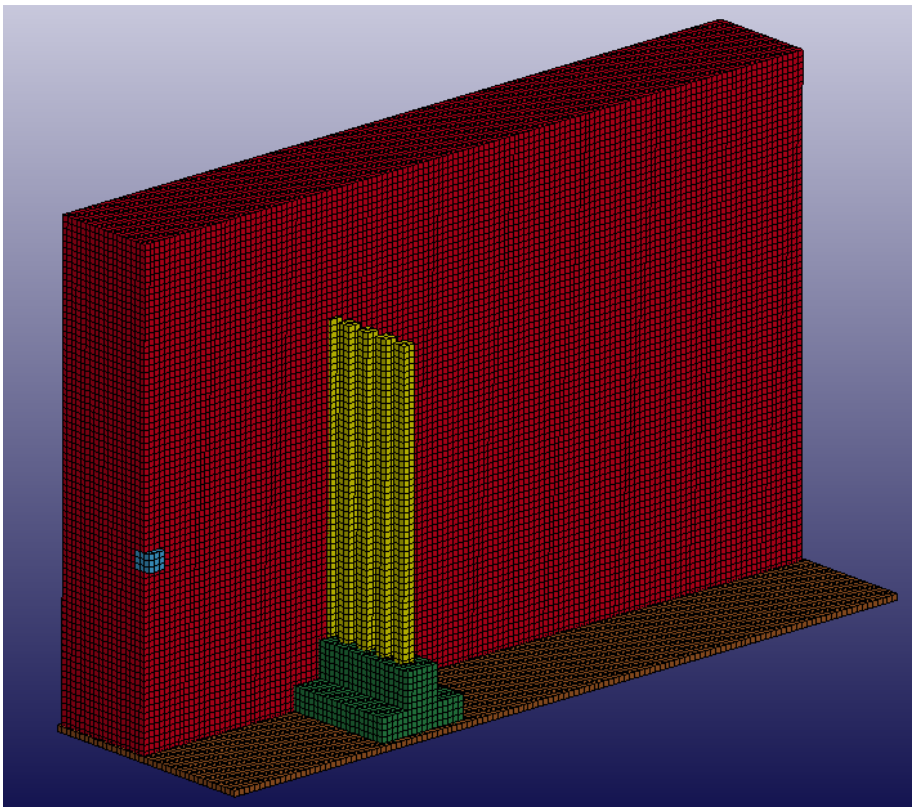

Figure 5.13: Entire model with all the 5 parts

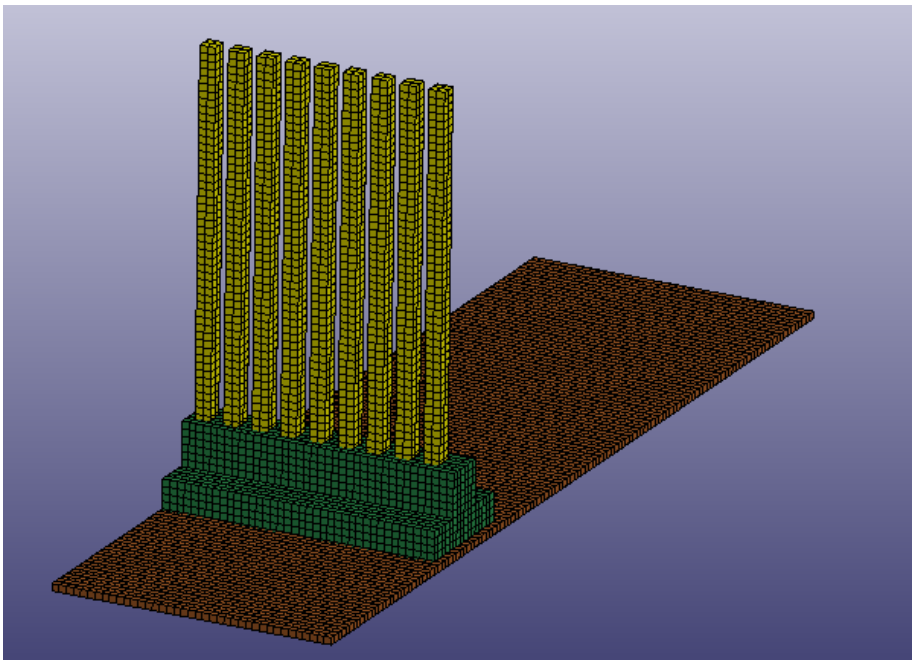

Figure 5.14: Entire model with only the lagrangian parts

in this section we set the pressure applied to the free surfaces of the ALE mesh boundary equal to the atmospheric pressure. The elements formulation used for the the barrier, both the basement and the pipes, and the elements of the ground is the $n.1$ that refers to the Lagrangian Solids. The field of the air needs the *BOUNDARY NON REFLECTING conditions, in order not to have the reflection of the wave at the boundary of the domain.

For what concerns the material of the *ALE* parts, the air and the explosive, they are the same that we used in the previous models, and also the equations of state are the same. The Lagrangian parts have new material properties and in particular we assign to the ground and the basement of the barrier the properties of a rigid body. In order to do this we have always chosen the properties of the elastic material, but we have set a very high $Young$ modulus. For the column we have assigned the properties of

the GFRP, but with the equivalent elastic modulus E_{eq} calculated in (5.1) . Both the parts of the column and the ground are modelled using the elastic material properties. In this kind of material properties we have only to set the density and the Young modulus of the material. The properties of the elastic materials are summarized in the tables 5.2 , 5.3 , 5.4 .

mid	ro	E	pr	da	db
3	2.5	100.0	0.00	0.00	0.00

Table 5.2: MAT ELASTIC parameters of the basement

mid	ro	E	pr	da	db
4	10.0	100.0	0.00	0.00	0.00

Table 5.3: MAT ELASTIC parameters of the ground

mid	ro	E	pr	da	db
5	1.8	0.02.00	0.00	0.00	0.00

Table 5.4: MAT ELASTIC parameters of the GFRP bars

All the units are consistent (g,cm,μs,$Mbar$)

5.4 Results

5.4.1 Experimental test results

In this section we show the results of the experimental data achieved in (Asprone et al., 2009), for all the three tests. We check the pressure of the

sensors $S1$ and $S6$, shown in figure 5.5 , 5.6, 5.7, that shows the pressure with and without the barrier. In the second test the pressure gauge $S1$ has not worked well, so we have calculated the free field reflected pressure with the Henrych formula with the amplification coefficent k (2.20).

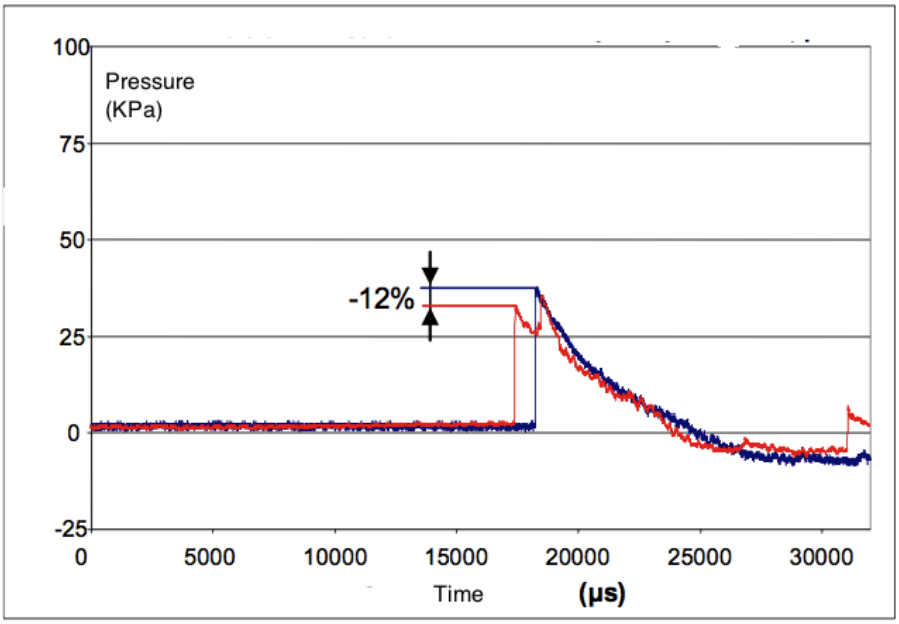

Figure 5.15: Comparison between the pressure at the gauges S1 and S6 in the first blast

Now we can compile the table 5.5 with the reduction of pressure in percentage.

S1 vs S6	5 Kg at 5m	5 Kg at 3m	5 Kg at 0.5m
Reduction in %	12 %	47 %	36 %

Table 5.5: Reduction of the overpressure with the barrier in the three blast tests

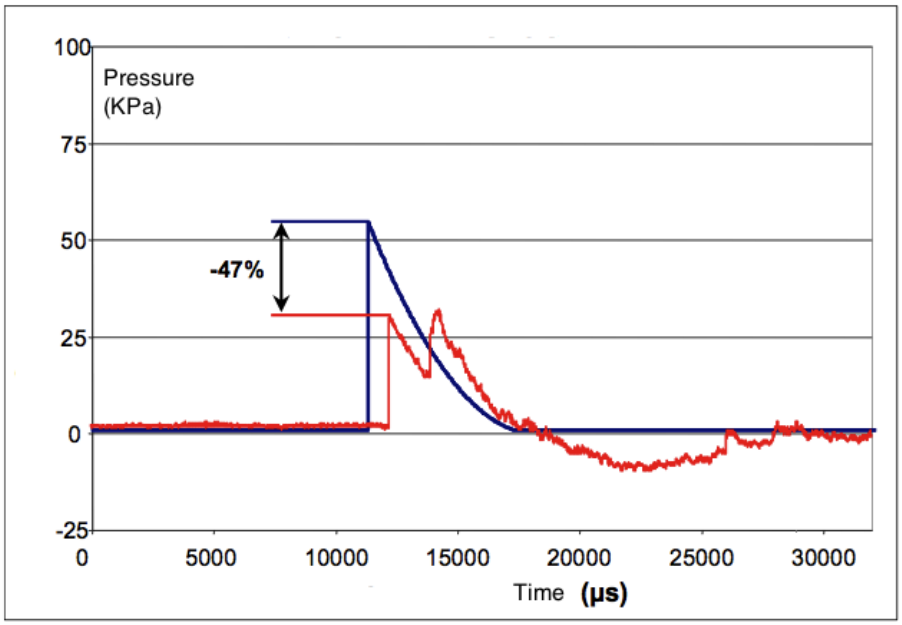

Figure 5.16: Comparison between the pressure at the gauges S1 and S6 in the second blast

5.4.2 Numerical results

Here we show the results of the numerical simulations. We first show some instants of the pressure wave propagation, and then we check the history data to evaluate the pressure behind the barrier. We model the explosive charge at the distance of $1,5m$ from the barrier, that is the minimum distance that not cause the failure of such protection system (Asprone et al., 2009). For this reason we are able to catch the maximum pressure reduction due to this kind of barrier. We take in exam the pressure exactly behind the barrier (pressure gauge $S6$ in figure (5.7)). To make the comparison with the overpressure without the barrier, once again we use the Henrych formulation (Henrych, 1979) with the amplification coefficent k (figure 2.11 (b)). We do not evaluate this overpressure from a simulation that would be too much computationally expensive. The pressure is evaluated at different distances

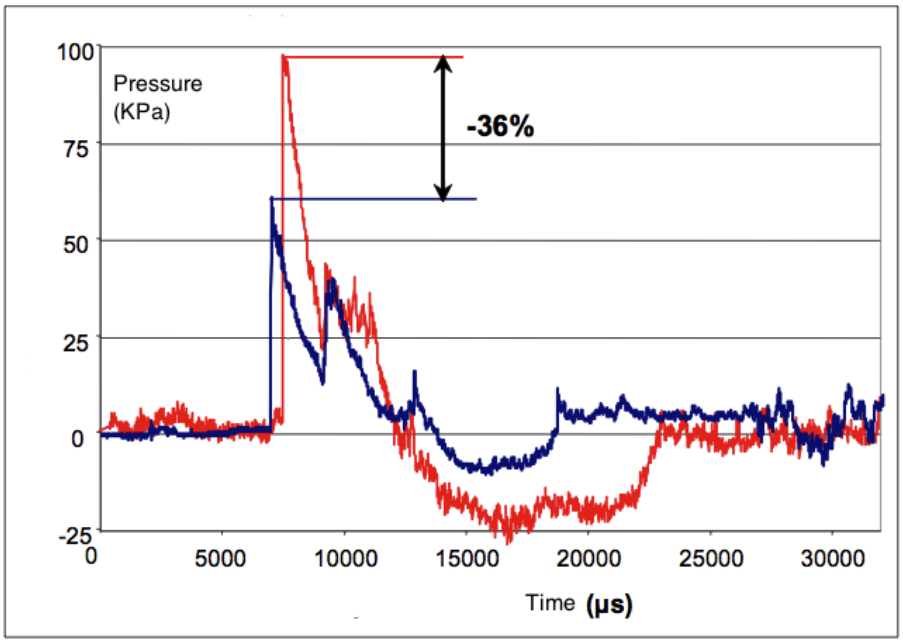

Figure 5.17: Comparison between the pressure at the gauges S1 and S6 in the third blast

behind the barrier, thus we can verify at what distance from the barrier we have the higher pressure and the higher pressure reduction, having placed the charge at $1.5m$ from the barrier.

In figure 5.19 we can see that the pressure wave, first overlaps the barrier at the top side, and we can only see a little gleam of pressure passes trough the barrier, that shows that, there is the interaction between the wave and the poles.

In a second moment we can clearly see that the shock-wave passes trough between the bars and joins the pressure that had passed at the top of the barrier. It is evident also the pressure wave reflected from the barrier (figure 5.20).

Finally we see that the two waves form an unique front, and we can also see that the reflected wave returns to the source of the explosion, and

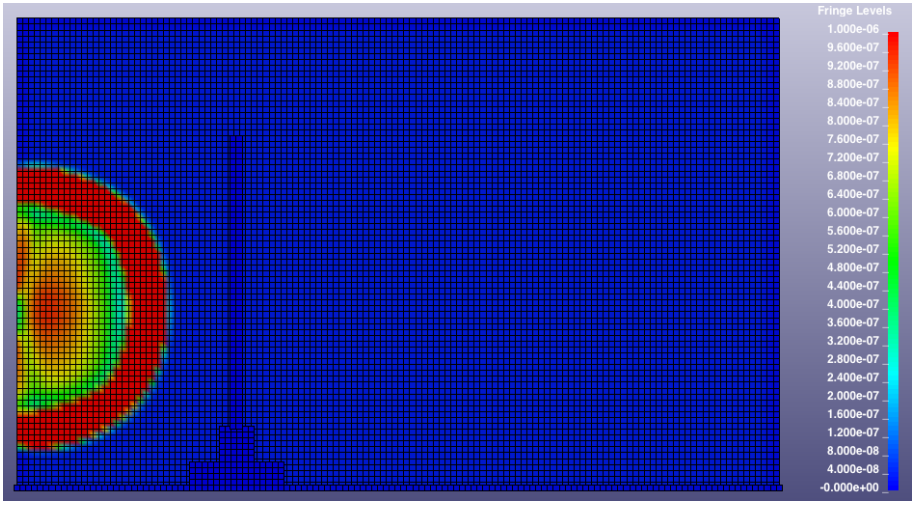

Figure 5.18: Contour of pressure at time=500 μs

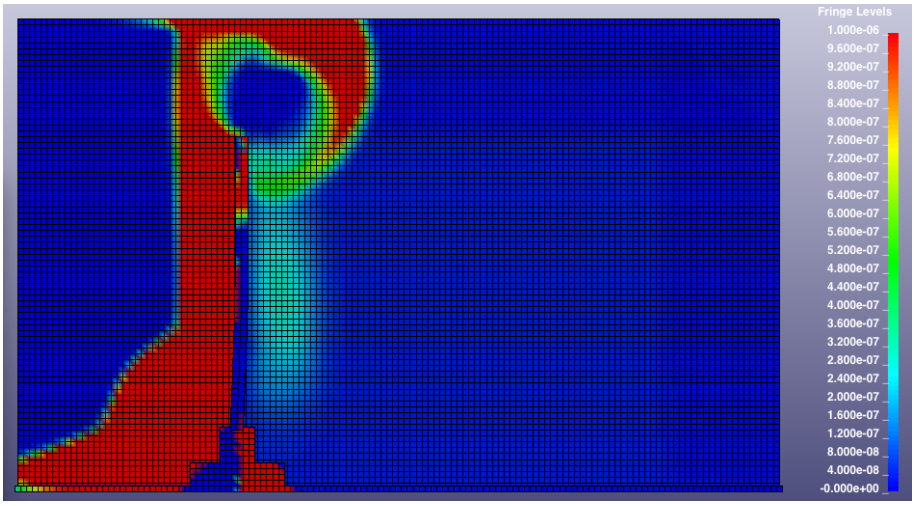

Figure 5.19: Contour of pressure at time=4000 μs

decreases more quickly than the pressure than the pressure that passes trough the barrier (figure 5.21).

To highlight also the pressure wave that passes at the side of the barrier we take two instants with a top visualization. Also in this images it is clear that first the pressure passes at the side of the barrier, and then it passes

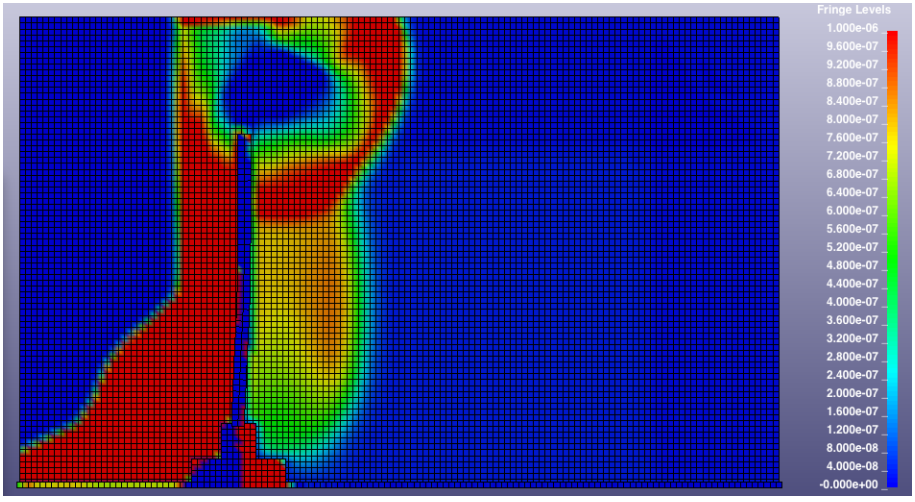

Figure 5.20: Contour of pressure at time=5200 μs

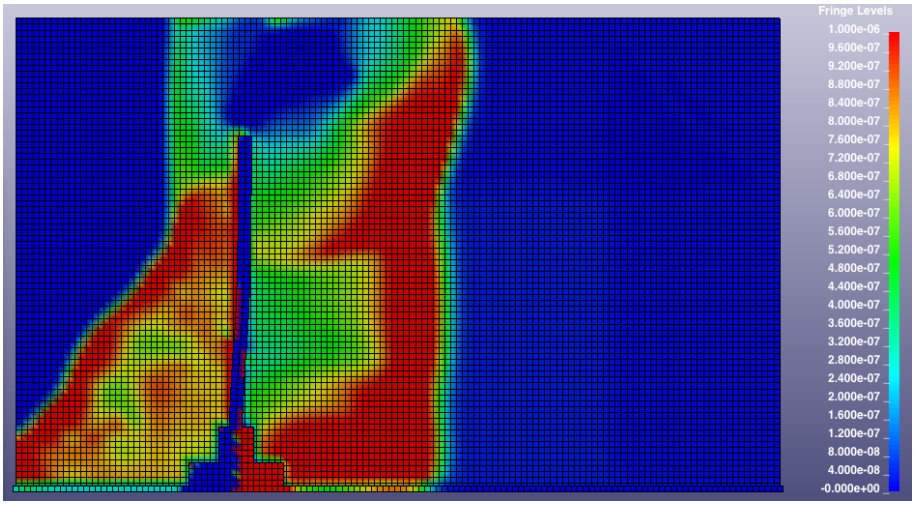

Figure 5.21: Contour of pressure at time=9100 μs

trough. (figures 5.22 5.23)

Due to the high computational time we can not perform the simulation with the charge positioned at $3m$ from the barrier, which experimental data are provided by the group of the University of Naples. Conversely the simulation about the charge at the distance of $0.5m$ is not very significant because

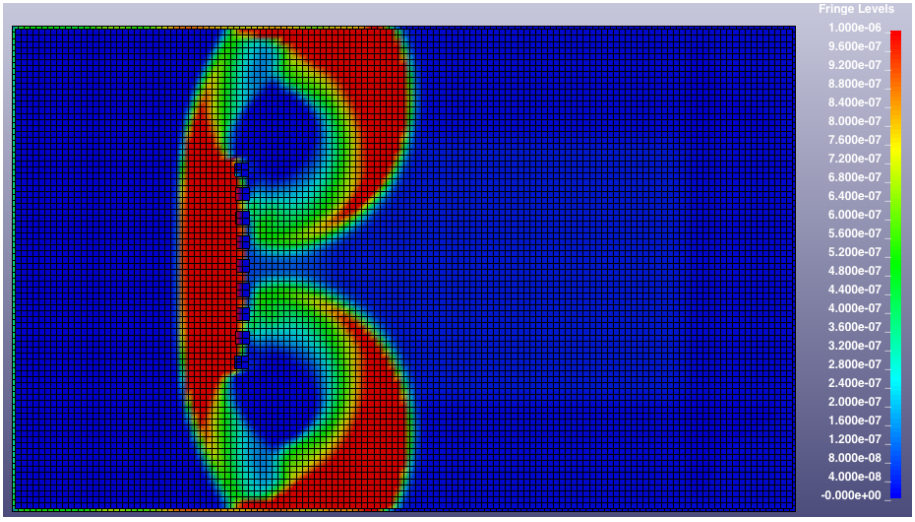

Figure 5.22: Contour of pressure at time=4000 μs

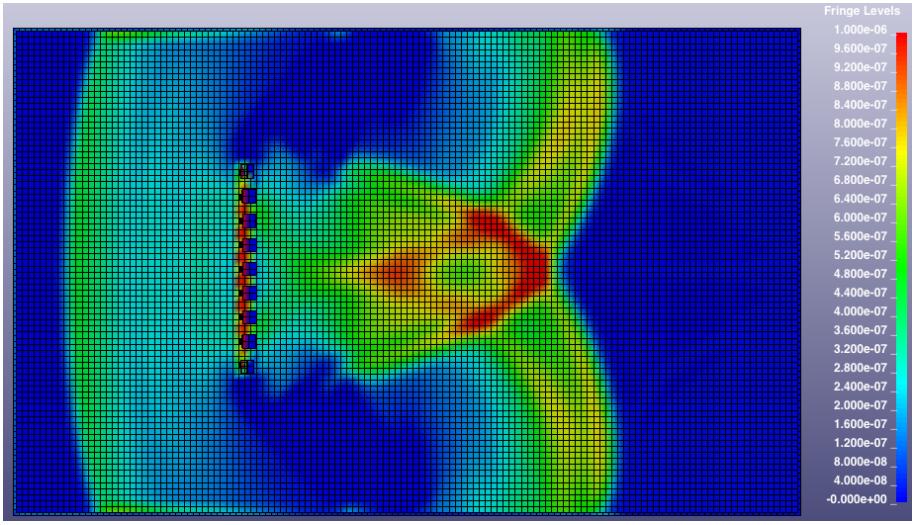

Figure 5.23: Contour of pressure at time=9100 μs

in that case the barrier does not resist to the blast, and other phenomena occurs, like failure of the barrier, which are not included in the numerical model. For all these reasons we cannot compare the data of the experiments with the data of the simulation, but we can use them to have an idea, if the simulation results are in good agreement with the tests data. In our

case the values of pressure at the highest distance behind the barrier is in an element positioned at the distance of $3m$ (total distance from the center of the explosive $D = 4.5m$) (figure 5.29) and it is about $72\,KPa$. The values of pressure in the third test at sensor $S6$, is of the same order of magnitude ($75\,KPa$). So probably the values of the simulation are a little bit higher than the results of the experimental test, but in acceptable manner and the behaviour of the blast-wave it exactly the same.

Back to the simulation results, in the table 5.6 we summarize the pressure evaluation in different elements behind the barrier, compare this results with the values without the barrier, and check the difference in percentage. Here we show the procedure used to derive the overpressure in air with a charge of $5Kg$ of TNT.

$$\overline{R} = \frac{R}{\sqrt[3]{W}} \qquad [m/Kg^{1/3}] \tag{5.2}$$

The scaled distance $\overline{R}$ is always greater than 1 so the overpressure is evaluated by:

$$\Delta p_{\Phi} = \frac{0.622}{\overline{R}} + \frac{4.05}{\overline{R}^2} + \frac{3.288}{\overline{R}^3} \quad [kp/cm^2] \quad for \quad 1 \leq \overline{R} \geq 10 \tag{5.3}$$

$$\alpha = arctg\frac{D}{H_c} \tag{5.4}$$

where α is the angle of incidence, D the distance from the center of the explosive and H_c the height of the explosive.

Then the coefficent k is evaluated with the graphic in figure (2.11 (b)).

The results of the computation of the free overpressure, the evaluated overpressure behind the barrier by the numerical simulation, and the reduc-

tion factor between the two pressures (with and without the barrier) are summarized in table 5.6.

Distance D (m)	α $(C\circ)$	k	Pressure without barrier (KPa)	Pressure with barrier (KPa)	Reduction factor $(\%)$
2.0	59,06	2	253,61	118,67	58,72
2.5	59,06	1,8	253,61	117,21	48,65
3.0	63,47	1,8	191,06	100,02	47,65
3.5	66,83	1,8	159,68	83,54	47,68
4.0	69,47	1,6	119,86	79,06	34,04
4.5	71,60	1,6	102,52	72,66	29,12

Table 5.6: Calculated Overpressure with ground reflecting without barrier

In figures 5.24, 5.25, 5.26, 5.27, 5.28, 5.29, the time history graphs of the pressure behind the barrier at the difference distance with highlighting the reduction factor in percentage.

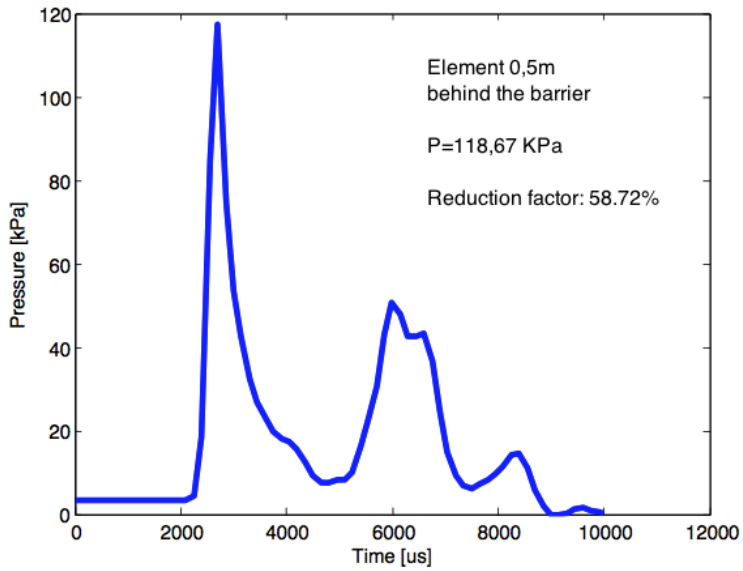

Figure 5.24: Time history of pressure behind the barrier D=2m

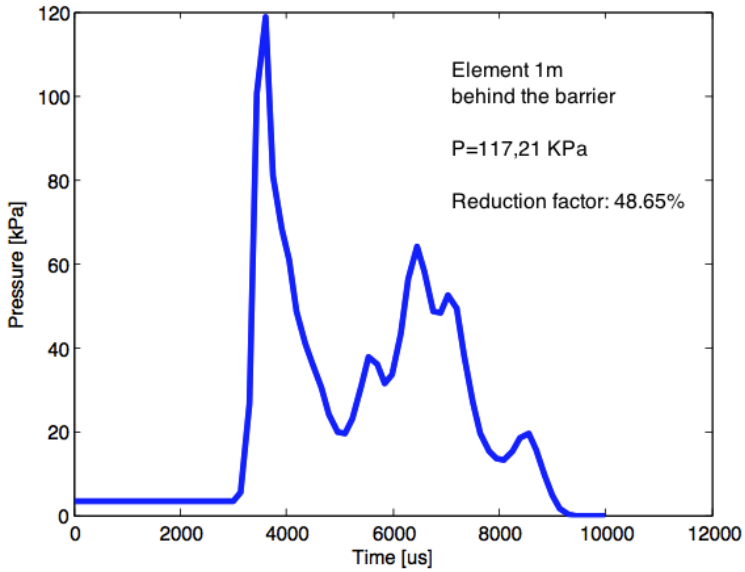

Figure 5.25: Time history of pressure behind the barrier D=2.5m

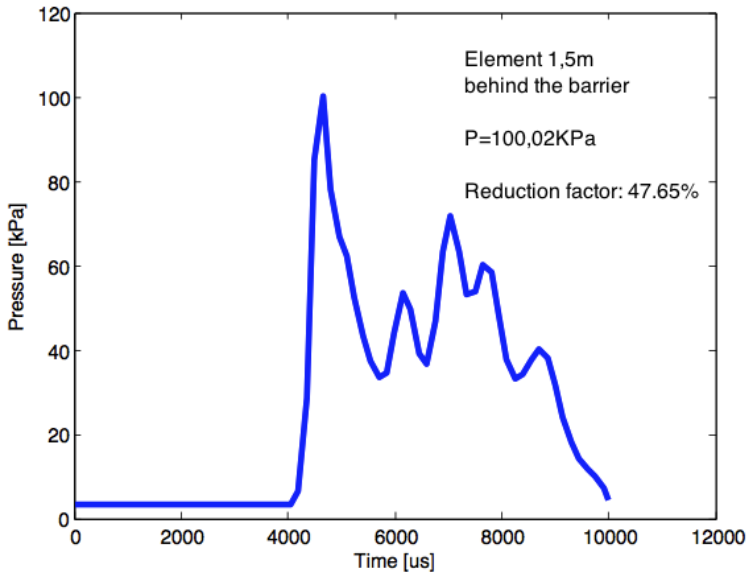

Figure 5.26: Time history of pressure behind the barrier D=3m

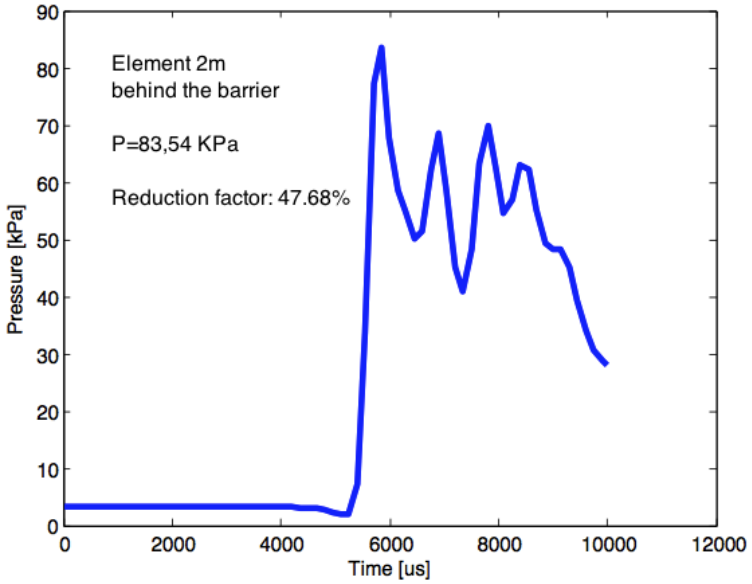

Figure 5.27: Time history of pressure behind the barrier D=3.5m

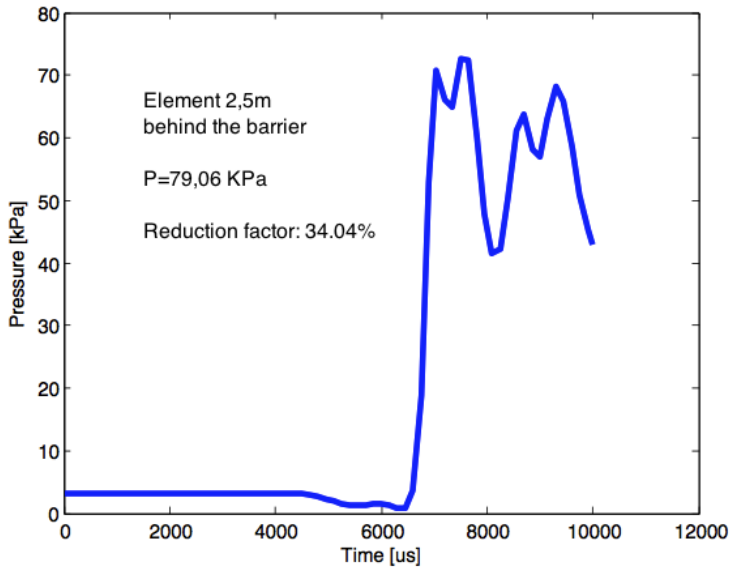

Figure 5.28: Time history of pressure behind the barrier D=4m

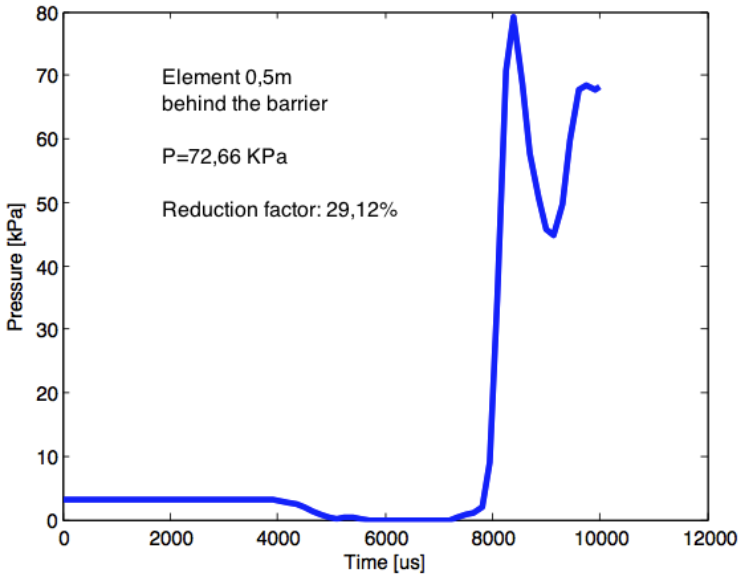

Figure 5.29: Time history of pressure behind the barrier D=4.5m

Chapter 6

Conclusions

In this work of thesis the problem of the numerical simulation of the behaviour of deformable structures subjected to explosive load has been studied. In our specific case we analyze the effectiveness of a porous barrier in the reduction of the pressure wave due to an explosion. The numerical model is accompanied by the experimental tests set up in mine at the University of Naples Federico II. The results of those tests help us to verify the rightness of our model. The numerical model treated in this work is inserted in the SAS project, that has the goal of design structures that can grant protection of strategics airport buildings subjected to terrorist action, and to preserve the incolumity of people and things at risk. Has been developed in the "Homeland Security of the research center AMRA".

Before achieving this goals we introduce the empirical and experimental models present in the literature, to step by step confront and validate the performed simulations.

With the first simulation, trough the CONWEP function, we have fronted the first approach with the simulation of explosive loads. This kind of numerical model is strictly usable in specific cases, where the wave does not

undergo reflections, thus the explosive have to be very near to the target. We can derive that the stress propagation along the longitudinal axis of the cantilever beam is influenced by the density of the mesh. From the convergence analysis that we have performed we see that the best configuration in terms of precision of results and computational time effort is the second one. In fact, the shape of the wave is well defined, it is perfectly reflected after one turn, and there is not decrement of intensity in going forward with time. Also the third finest configuration respects this standard, but the computational time and the size of the model are higher, and the difference between the results is not enough to justify the size of the model.

From the model of the free explosion in air we have simulated the development and the propagation of a shock-wave of a cubical explosion. We denoted that at the beginning the shape of the modelled explosive influences the shape of the wave, but after small instants the wave takes the classical spheric shape. From this model we have highlighted some of the major characteristics of the shock wave, like the time arrival, the peak overpressure and the propagation velocity in the fluid. From the tables and the graphics constructed we derive that the trend of the overpressure in function of the scaled distance $\overline{R}$ is in good agreement with the trend evaluated with the Henrych formulations (Henrych, 1979), and the shock front velocity always in function of the scaled distance follows well the trend proposed by Kingery and Bulmash (1984).

The two models with Fluid Structure Interaction helped us to understand the behaviour of a shock-wave that impacts a structure. From the model with the cantilever beam, the interaction is only with the beam, and we check the stress propagation along the longitudinal axis, to compare the result with the CONWEP function. The result shows that the the trend of the stresses

is the same, but their shape is not very well defined, because the shape of the shock-wave that arrives at the face of impact is altered by the propagation in air. We also compare the velocity of the stress propagation in the beam with the one calculated analytically , and we can observe that the two values are in good agreement. In the model with the standalone column the interaction occurs also with the ground, modelled as rigid. Here we have evaluated the reflected pressure, and the pressure that reaches the back side of the column to check the reduction of pressure. Also we check the trend of the Von-Mises stress and we derive that in the region at the base of the column there are the highest values of stresses. The last evaluated thing is the trend of the displacement in the elements from top to the bottom of the column. Obviously the higher values are registered at the top of the column, and decrease until zero, going to the base of the column.

The last model provide the simulation of the porous barrier subjected to the explosion at $1,5m$ from it. From this model we have a visual approach of the phenomenon of the passage of a shock-wave trough a porous barrier, described in section 5.2 (Hadassah and Doyle, 2007). We see the pressure that impacts the barrier; the wave first overlaps the structure at the top, and then after the interaction with the bars, passes trough them and continues its propagation. The wave passes also at the side of the barrier so, at a certain point, there is the conjunction of all the fronts to form a unique contour. We evaluate the pressure behind the barrier at different distance behind the barrier, precisely from $0.5m$ to $3m$ and we compute the reduction between these values and the ones calculated without the protection with the Henrych formula and the amplification factor k (2.20) . Then calculate the reduction factor in percentage; the higher reduction of pressure is at the point nearest to the barrier $(0,5m)$, where the pressure is reduced by the presence of the

barrier by 58%. In the farther point to the barrier the reduction factor drops to the 29%.

At the end of this thesis work we can see that a porous barrier, that respects the standard of radio transparency, is suitable to the protection of medium charge, at a distance greater than $1,5m$, granted a reduction of the overpressure in the regions behind it until 58%.

Bibliography

Alia, A. and M. Souli (2005). High explosive simulation using multi-material formulations. *Elsevier*.

Aquelet, N. and M. Souli (2008). 2d to 3d ale mapping. *10th International LS-Dyna User Conference*.

Army, U. S. (1990). Technical manual (tm5-1300): To resist the effect of accidental explosion. *Department of the Army, Navy and Air force, Washington DC*.

Army, U. S. (1991). U.s. army engineer waterways experiment station. tm 5-855-1. *Fundamentals of protective Design for Conventional Weapons*.

Asprone, D., A. Nanni, H. Salem, and H. T. Din (2009). Element method analysis of porous gfrp barrier subjected to blast.

Baker, W. E., P. A. Cox, P. S. Westine, J. J. Kulesz, and R. A. Strehlow (1983). Explosion hazard and evaluation. *Elsevier*.

Belytschko, T., W. K. Liu, and B. Moran (2000). Nonlinear finite elements for continua and structures. *Wiley New York*.

Bergano, C. (1973). Gli esplosivi. *Hoepli*.

Coleburn, N. L. (1964). Chapman-jouguet pressures of several pure and mixed explosives. *Defense Technical Information Center*.

Dobratz, B. M. (1981). Llnnl explosive handbook, properties of chemical explosive and explosive simulants. *Lawrence Livermore National Laboratory*.

Hadassah, N. and D. K. Doyle (2007). The effect of porosity on shock interaction with a rigid, porous barrier. *Shock Waves*, 321–337.

Hallquist, J. O. (2006). Ls-dyna theory manual. *Livermore Software Technology Corporation (LSTC)*.

Harold, L. and H. Brode (1955). Numerical solution of spherical blast waves. *Journal of applied physics 26*.

Henrych, J. (1979). *The dynamics of explosion and its use*. Elsevirer.

Hou, G., J. Wang, and A. Layton (2012). Numerica methods for fluid-structure interaction - a review. *Commun. Comput. Phys. 12*, 337–377.

Kingery, Charles, and Pannill (1964). Parametric analysis of the regular reflection of airblast. *BRL Report 1249*.

Kingery, C. and G. Bulmash (1984). Air blast parameters from tnt spherical air burst and hemispherical surface burst. *Ballistic Research Laboratories*.

Leer, B. V. (1984). Multidimensional explicit difference schemes for hyperbolic conservation laws. *Elsevier*.

Miller, K. and G. Joldes (2006). Total lagrangian explicit dynamics finite element algorithm for computing soft tissue deformation. *InterScience 122-124*.

Naumyenko, I. A. and G. I. Petrovsky (1956). The shock-wave of nuclear explosion. *BOEH, CCCP*.

Pehrson, G. R. and K. A. Bannister (1997). Airblast loading model for dyna2d and dyna3d. *Army Reserach Laboratory*.

Richter, T. (2010). Numerical methods for fluid-structure interaction problems.

Sadovsky, M. A. (1952). Mechanical effects of air shock wave from explosion according to experiments. *AH, CCCP*.

Seguiti, T. (1969). Le mine nei lavori minerari e civili. *L'industria mineraria*.

Smith, P. D. and T. A. Rose (2002). Blast loading and bbuilding robustness. *4*, 213–223.

Thiel, V. M., E. L. Lee, and S. Cochran (1983). Effects of overdriven shock states on the equation of state of 9404 explosive. *Applied Physic 6760-6763*.